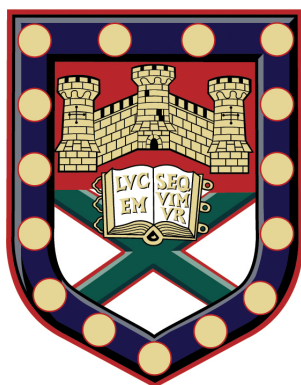# Optoelectronic devices based on van der Waals heterostructures

Submitted by Jake D. Mehew to the University of Exeter as a thesis for the degree of Doctor of Philosophy in Physics

September 2018

This thesis is available for library use on the understanding that it is copyright material and that no quotation from the thesis may be published without proper acknowledgement.

I certify that all material in this thesis which is not my own work has been identified and that no material has previously submitted and approved for the award of a degree by this or any other university.

<div style="text-align:right">

_____

Jake D. Mehew

</div>

Abstract

In this thesis we investigate the use of van der Waals heterostructures in optoelectronic devices. An improvement in the optical and electronic performance of specific devices can be made by combining two or more atomically thin materials in layered structures. We demonstrate a heterostructure photodetector formed by combining graphene with tungsten disulphide. These photodetectors were found to be highly sensitive to light due to a gain mechanism that produced over a million electrons per photon. This arises from the favourable electrical properties of graphene and the strong light-matter interaction in WS_2. An analysis of the photodetector performance shows that these devices are capable of detecting light under moonlight illuminations levels at video-frame-rate speeds with applications in night vision imaging envisaged. We also report a novel method for the direct laser writing of a high-k dielectric embedded inside a van der Waals heterostructure. Such structures were shown to be capable of both light-detection and light-emission within the same device architecture, paving the way for future multifunctional optoelectronic devices. Finally we address a more fundamental problem in the properties of aligned graphene/hBN heterostructures. Strain distributions are shown to modify the electronic properties of graphene due to a change in the interlayer interaction. We demonstrates a method to engineer these strain patterns by contact geometry design and thermal annealing strategies.

Acknowledgements

This thesis represents a culmination of many years of education and research. Along my way to writing this an extraordinary number of people have supported and encouraged me - without them I certainly would not have got this far. This page is meant as way of saying thank you.

Firstly I would like to thank my supervisors Prof. Saverio Russo and Prof. Monica Craciun for their guidance over the past few years. It is clear you are both highly passionate about your work and this manifests in your desire to be continually learning. You are also determined in helping people realise their potential without applying unnecessary pressure or stress. This has helped foster an excellent research environment in which people are not afraid to explore new ideas and challenge existing ones - sometimes even your own.

Within your research groups I have had the opportunity to work with some excellent scientists and build lasting friendships. On my first day as a PhD student Gareth and Domi were there to show me the ropes, teach me about fabrication and measurements for which I am extremely grateful. Gareth throughout my PhD always found the time to explain new concepts and discuss results. Thank as well must go to Adolfo for all his help with optoelectronic measurements, our many collaborations, and interesting discussions on food/drink, politics and Dartmoor. Nicola and Iddo are also very knowledgeable on a number of topics and we have had many engaging conversations over meals together. Elias you brought energy to the lab: drumming, singing, whistling etc and were always up for a party. You also had a talent for growing graphene and produced many CVD samples for our projects together. Saad you have a crazy energy as well, taking you on driving lessons was an experience! Thanks too to Freddie for teaching me how to stack flakes and having time for beers after work. Without this many projects would have been impossible. To the minions (Namphung and Janire) you made the cleanroom a far more enjoyable place to work. I should also acknowledge the technicians for their help and expertise over the years in particular Paul, Nick and Adam in the workshop as well as Mark whose managed to keep the cleanroom running relatively smoothly.

Away from physics I thank my wonderful group of friends both in Exeter and further afield for keeping me sane and providing much needed distraction from work. To my family: I cannot express enough thanks for everything you have done and the patience you have shown me over the years. You all have made me the person who I am today.

Finally to Lara, thank you. You have brought so much happiness into my life over the last few years. I couldn't have done this without your love and support.

Contents

List of Figures

Publications

- **J. D. Mehew**, S. Unal, E. Torres Alonso, G. F. Jones, S. Fadhil Ramadhan, M. F. Craciun, and S. Russo, Fast and Highly Sensitive Ionic-Polymer-Gated WS 2 -Graphene Photodetectors. Adv. Mater. 29, 1700222 (2017).

- **J. D. Mehew**, M. D. Barnes, M. Dubois, M. F. Craciun, and S. Russo, Role of defect states in functionalized graphene photodetectors. in Active Photonic Platforms IX (eds. Subramania, G. S. & Foteinopoulou, S.) 10345, 29 (SPIE, 2017).

- F. Reale, P. Palczynski, I. Amit, G. F. Jones, **J. D. Mehew**, A. Bacon, N. Ni, P. C. Sherrell, S. Agnoli, M. F. Craciun, S. Russo and C. Mattevi11, High-Mobility and High-Optical Quality Atomically Thin WS2. Sci. Rep. 7, (2017).

- A. De Sanctis, **J. D. Mehew**, S. Alkhalifa, C. P. Tate, A.White, A. R. Woodgate, M. F. Craciun, and S. Russo, Novel circuit design for high-impedance and non-local electrical measurements of two-dimensional materials. Rev. Sci. Instrum. 89, 024705 (2018).

- A. De Sanctis, **J. D. Mehew**, M. F. Craciun, and S. Russo, Graphene-based light sensors: fabrication, characterisation, physical properties and performance. Materials MDPI 11(9), 1762; (2018)

- A. De Sanctis, **J. D. Mehew**, S. Alkhalifa, F. Withers, M. F. Craciun, and S. Russo, Strain-Engineering of Twist-Angle in Graphene/hBN Superlattice Devices, Nano Letters 18, 7919 (2018)

- N. Peimyoo, **J. D. Mehew**, M. D. Barnes, A. De Sanctis, I. Amit, J. Escolar, K. Anastasiou, A. P. Rooney, S. J. Haigh, S. Russo, M. F. Craciun, and F. Withers, Laser written high-K dielectric for flexible van der Waals nano-electronics, Science Advances *accepted for publication* (2019)

- N. Townsend, I. Amit, **J. D. Mehew**, T. Octon, M. F. Craciun, and S. Russo, Temperature Dependence of Charge Traps in Atomically Thin Transistors, *in preparation*

- A. De Sanctis, **J. D. Mehew**, S. Alkhalifa, M. F. Craciun, and S. Russo, 1D capacitance measurements of quantum phenomena in ballistic graphene FETs, *in preparation*

Declaration

The research presented in this thesis relates to several of the manuscripts included in the preceding list of publications, for which there are multiple co-authors in each study. The content enclosed in this thesis is intended to highlight my individual contribution towards a number of these collaborative research projects and has not previously been submitted and/or approved for the award of a degree by this or any other university.

Jake D. Mehew, September 2018

Abbreviations

2D   two-dimensional

AFM   atomic force microscopy

BLG   bilayer graphene

CAFM conductive atomic force microscopy

CMOS complementary metal–oxide–semiconductor

DFT   density functional theory

DI   deionised

DOF   degree of freedom

FET   Field-effect transistors

FIR   far infrared

LED   light-emitting diode

MoS_2 molybdenum disulphide

PDMS Polydimethylsiloxane

PMMA Poly-methyl methacrylate

PPC   polypropylene carbonate

PV   photovoltaic

SLG   single-layer graphene

SPCM Scanning Photocurrent Microscopy

SPCM scanning photocurrent microscopy

TMD transition metal dichalcogenide

WS_2 tungsten disulphide

1

Introduction

1.1 Optoelectronics

Optoelectronic devices bridge the optical and electronic worlds.[1] Modern technology relies heavily on optoelectronic devices especially within the fields of telecommunications, energy generation and consumer electronics. Transcontinental fibre optic cables carry photonic signals around the world through a series of infrared lasers, optical amplifiers and detectors with this interconnectivity forming the foundation of the internet. Solar panels convert sunlight into electricity which can power our homes and businesses. In the UK alone solar photovoltaic (PV) capacity has grown from 22 MW in 2008 to over 13 000 MW in 2017.[2] At an individual level optoelectronic devices are found everywhere. Smart phones have high-definition organic light-emitting diode (LED) displays as well as high-resolution CMOS (Complementary metal–oxide–semiconductor) image sensors.

The use of optoelectronic devices is expanding at an impressive rate. Economic forecasts predict that the global optoelectronics market is set to grow $\sim 18\%$ a year between 2017 - 2023.[3] Currently materials such as silicon and germanium are at the heart of optoelectronic devices. To maintain such growth into the future and develop new markets, such as in wearable electronics,[4–6] a new generation of materials are required.

1.2 Two-dimensional materials

Graphite was first utilized by a modern civilization in the 16th century by the English Royal Navy. The discovery of a massive deposit in Cumbria, England led to the creation of the now famous Borrowdale mine. Here graphite was used to reduce the surface roughness of cannon balls by acting as a lining material in the moulds.[7] The smoother design increased the range at which they could be fired owing to a reduction in the skin friction drag and arguably this contributed to the naval dominance of the British over the next few hundred years. It therefore seems

fitting that the latest major advance in the study of graphite was also made in the United Kingdom.

The ground breaking experiments into graphene,[8] a single layer of graphite, led by Andre Geim and Kostya Novoselov ignited interest in two-dimensional (2D) materials and subsequently won them the 2010 Nobel Prize in Physics. The unprecedented attention that graphene has received is demonstrated by the huge numbers of papers being published on the subject. The success of graphene allowed researchers to re-examine the properties of other layered materials at the monolayer limit. Today the 2D material family includes insulators, such as hexagonal boron nitride (hBN), and semiconductors (e.g. molybdenum disulphide, MoS_2) to complement the semimetal graphene.

Two-dimensional materials have found applications across many fields in science including electronics,[9–11] photonics and optoelectronics,[12–15] plasmonics,[16] and spintronics.[17] Present research efforts are focussed on combinations of 2D materials known as van der Waals heterostructures.[18] These structures can combine the properties of two materials into a single device due to an interlayer interaction which is able to redistribute charges and induce structural changes. In this thesis we explore some of these material combinations as an attempt to overcome their individual limitations.

1.3   This Thesis

In Chapter 2 the theoretical concepts which underpin the experimental work will be introduced. In particular the electronic and optical properties of graphene, hBN, and transition metal dichalcogenides (TMDs) are discussed. Optoelectronic devices based on 2D materials are introduced with explanations of common figures of merit and photodetection mechanisms provided to guide the reader. Finally a literature review of graphene-based photodetectors is presented highlighting the key areas in which improvements can be made. Chapter 3 details in depth the experimental techniques that have produced the results found in subsequent chapters. The creation of heterostructures of 2D materials through the dry transfer technique is described as is the fabrication of high-quality optoelectronic devices. Raman spectroscopy is introduced through both classical and quantum theories and discussed with regards to graphene and TMDs. Techniques for the characterisation of optoelectronic devices are also discussed. The first experimental investigation can be found in Chapter 4. Here, tungsten disulphide (WS_2) is used as a light-absorbing layer in a graphene phototransistor. The strong light-matter interaction of WS_2 coupled with the electronic properties of graphene produces a highly sensitive photodetector. Unique to this system is the screening of charged impurities which increases the speed of the device over previous works. Chapter 5 demonstrates a technique for the incorpora-

tion of a high-k dielectric into heterostructures of 2D materials. The optoelectronic properties of a tunnelling transistor based on this are examined with the results demonstrating that both light-emission and light-detection are possible within a single device architecture. This is the first demonstration of the use of high-k dielectrics in van der Waals heterostructure optoelectronic devices. Finally in Chapter 6 a method for strain engineering of the twist angle between graphene and hBN is demonstrated. Complementary Raman spectroscopy and electrical transport measurements reveal that strain can be induced and relaxed in these superlattice structures. This represents an important step in the understanding the role played by contacts in twist-angle phenomena.

References

[1] John Wilson and J. F. B. Hawkes. Optoelectronics - An introduction (2nd edition). *Optoelectronics - An introduction (2nd edition), by J. Wilson and J.F.B. Hawkes. Englewood Cliffs, NJ, Prentice Hall, 1989, 483 p.*, 1989.

[2] National Statistics. Energy Trends: March 2018. Technical report, Department for Business, Energy & Industrial Strategy, London, 2018.

[3] Stratistics MRC. Optoelectronics-Global Market Outlook (2017-2023). Technical report, Orbis Research, 2018.

[4] Mahiar Hamedi, Robert Forchheimer, and Olle Inganäs. Towards woven logic from organic electronic fibres. *Nature Materials*, 6(5):357–362, may 2007.

[5] Michael R Lee, Robert D Eckert, Karen Forberich, Gilles Dennler, Christoph J Brabec, and Russell A Gaudiana. Solar power wires based on organic photovoltaic materials. *Science (New York, N.Y.)*, 324(5924):232–5, apr 2009.

[6] A I S Neves, T H Bointon, L V Melo, S Russo, I de Schrijver, M F Craciun, and H Alves. Transparent conductive graphene textile fibers. *Scientific Reports*, 5(1):9866, sep 2015.

[7] University of Waterloo. Graphite - https://uwaterloo.ca/earth-sciences-museum/resources/detailed-rocks-and-minerals-articles/graphite.

[8] Konstantin S Novoselov, A K Geim, S V Morozov, D Jiang, Y Zhang, S V Dubonos, I V Grigorieva, and A A Firsov. Electric Field Effect in Atomically Thin Carbon Films. *Science*, 306(5696):666–669, oct 2004.

[9] Frank Schwierz. Graphene transistors. *Nature Nanotechnology*, 5(7):487–496, jul 2010.

[10] Gianluca Fiori, Francesco Bonaccorso, Giuseppe Iannaccone, Tomás Palacios, Daniel Neumaier, Alan Seabaugh, Sanjay K. Banerjee, and Luigi Colombo. Electronics based on two-dimensional materials. *Nature Nanotechnology*, 9(10):768–779, oct 2014.

[11] Adrien Allain, Jiahao Kang, Kaustav Banerjee, and Andras Kis. Electrical contacts to two-dimensional semiconductors. *Nature Materials*, 14(12):1195–1205, nov 2015.

[12] F Bonaccorso, Z Sun, T Hasan, and A C Ferrari. Graphene Photonics and Optoelectronics. *Nature Photonics*, 4(9):611–622, aug 2010.

[13] F. H. L. Koppens, T Mueller, Ph. Avouris, a C Ferrari, M S Vitiello, and M Polini. Photodetectors based on graphene, other two-dimensional materials and hybrid systems. *Nature Nanotechnology*, 9(10):780–793, oct 2014.

[14] Fengnian Xia, Han Wang, Di Xiao, Madan Dubey, and Ashwin Ramasubramaniam. Two-dimensional material nanophotonics. *Nature Photonics*, 8(12):899–907, nov 2014.

[15] Kin Fai Mak and Jie Shan. Photonics and optoelectronics of 2D semiconductor transition metal dichalcogenides. *Nature Photonics*, 10(4):216–226, 2016.

[16] K. S. Novoselov A. N. Grigorenko , M. Polini. Graphene plasmonics. *Nat. Photonics*, 6(October):749 – 758, nov 2012.

[17] Wei Han, Roland K Kawakami, Martin Gmitra, and Jaroslav Fabian. Graphene spintronics. *Nat Nano*, 9(10):794–807, 2014.

[18] K. S. Novoselov, A. Mishchenko, A. Carvalho, and A. H. Castro Neto. 2D materials and van der Waals heterostructures. *Science*, 353(6298):aac9439, jul 2016.

Theoretical concepts and literature review

2.1 Graphene family

2.1.1 Crystal lattice

Graphene is a two-dimensional (2D) allotrope of carbon in which three electrons form sp^2 hybridized covalent bonds with the remaining electon held in the p-orbital perpendicular to the plane of the sp^2. The overlap of these p orbitals into a π band leads to the de-localization of charge carriers in graphene which dominates the electrical transport properties.[1–3] hBN is the inorganic analogue of graphene where each pair of carbon atoms is replaced by a boron-nitride pair.[4–6] Similar to graphene it has two electrons per unit cell however due the difference in electronegativity between boron and nitrogen the π-electrons are localized around nitrogen.

Figure 2.1a shows the honeycomb crystal lattice with triangular Bravais lattice vectors:

$$\vec{a}_1 = \frac{a}{2}\left(3, \sqrt{3}\right), \quad \vec{a}_2 = \frac{a}{2}\left(3, -\sqrt{3}\right), \tag{2.1}$$

where $a \approx 1.42\,\text{Å}$ is the nearest neighbour distance between carbon atoms in graphene. The two sub-lattices A and B represent the two atom basis of the unit cell with each atom surrounded by three atoms from a different sub-lattice. The nearest neighbour vectors are:

$$\vec{\delta}_1 = \frac{a}{2}\left(1, \sqrt{3}\right), \quad \vec{\delta}_2 = \frac{a}{2}\left(1, -\sqrt{3}\right), \quad \vec{\delta}_3 = \frac{a}{2}\left(-1, 0\right). \tag{2.2}$$

The reciprocal lattice is also triangular with vectors:

$$\vec{b}_1 = \frac{2\pi}{3a}\left(1, \sqrt{3}\right), \quad \vec{b}_2 = \frac{2\pi}{3a}\left(1, -\sqrt{3}\right). \tag{2.3}$$

Figure 2.1b shows the Brillouin zone of the honeycomb lattice with zone centre
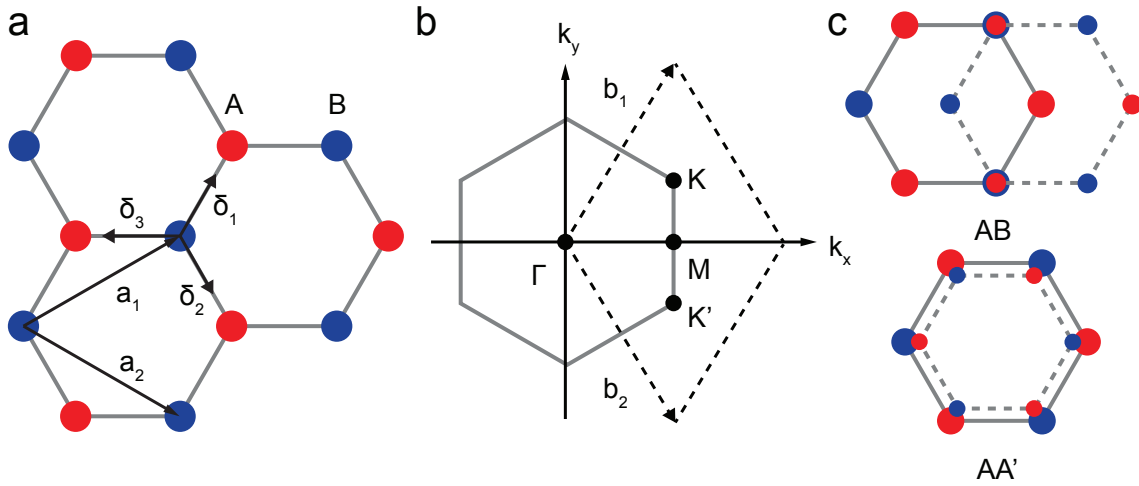
Figure 2.1: **Honeycomb lattice and stacking order.** (a) Triangular Bravais lattice with unit vectors $\vec{a}_1$ and $\vec{a}_2$ and nearest neighbour vectors $\delta_{1,2,3}$. In graphene carbon atoms occupy the A and B sub-lattices whereas for hBN boron and nitrogen atoms occupy an individual sub-lattice. (b) Brillouin zone of honeycomb lattice. Dirac cones are located at the K and K' for graphene (hBN has energy gap). (c) Optimal stacking modes of graphite (AB, top) and hBN (AA', bottom). For illustration purposes the second hexagonal layer has dashed lines and smaller atoms (coloured circles).

(Γ) and high-symmetry points K, K' and M:

$$\vec{K} = \left(\frac{2\pi}{3a}, \frac{2\pi}{3\sqrt{3}a}\right), \quad \vec{K'} = \left(\frac{2\pi}{3a}, -\frac{2\pi}{3\sqrt{3}a}\right), \quad \vec{M} = \left(\frac{2\pi}{3a}, 0\right). \qquad (2.4)$$

Graphite and bulk hBN consist of many monolayers weakly attracted to each other through a van der Waals potential.[3] It is this van der Waals gap that facilitates the exfoliation of individual layers from the bulk material. Adjacent layers can be stacked in different configurations for which an optimal stacking mode exists, Figure 2.1c. In graphite AB stacking is favourable where one carbon atom resides in the centre of the hexagon of the adjacent layer whereas in hBN a nitrogen atom in one layer resides on top of a boron atom in another (AA' configuration).[7]

The electronic structure of graphene arises from both sp^2 hybridized states and π states. The latter forms a single band with conical crossing points at K and K' whereas the former produces occupied and empty bands separated by a sizeable gap. The Fermi energy of undoped graphene is found at these crossing points separating the filled valence and empty conduction bands with zero band-gap. Due to the finite conductivity at zero temperature (a property of chiral Dirac fermions in 2D) graphene can be described as a semimetal.[2]
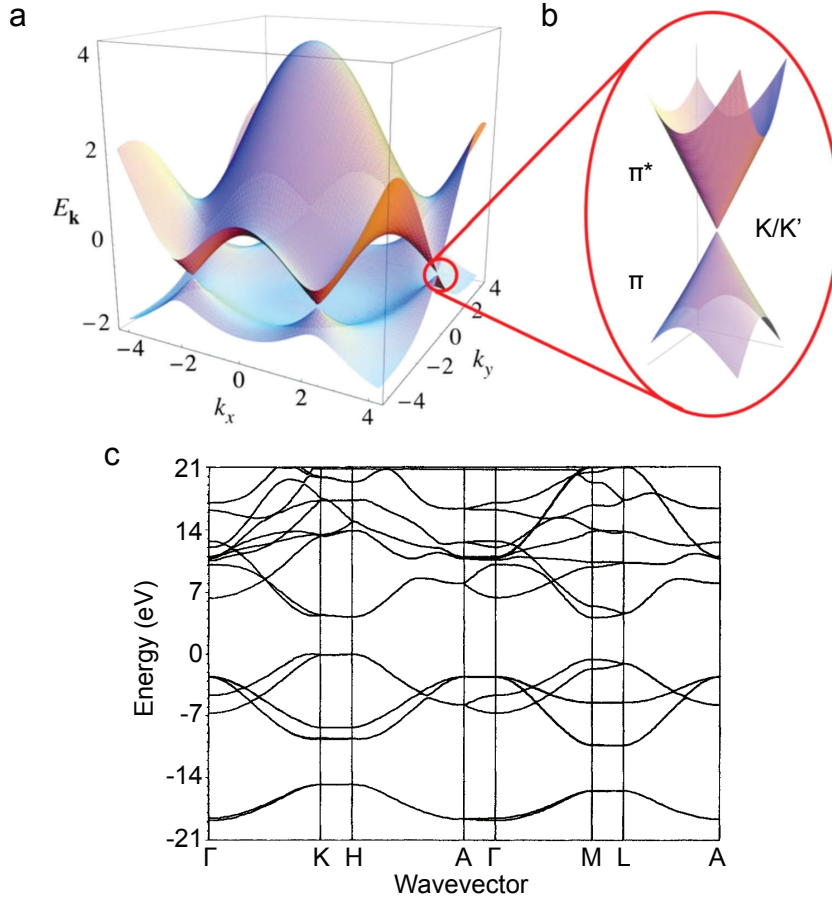
Figure 2.2: **Band structure of graphene and hBN.** (a) Energy spectrum of monolayer graphene (in units of t) in nearest neighbour approximation for $t = 2.7\,\text{eV}$ (b) Zoom of energy bands close to a Dirac point. (c) Energy spectrum of bulk hBN. (a,b) Adapted with permission.[3] (c) Adapted with permission.[5]

2.1.2   Tight-binding formulation

Figure 2.2a shows the band structure of graphene produced by considering only the π-states and nearest-neighbour hopping. Following the work of Wallace a simple tight-binding model is used.[1,3] The Hamiltonian is described by a 2×2 matrix:

$$\hat{H}(\vec{k}) = \begin{pmatrix} 0 & tS(\vec{k}) \\ tS^*(\vec{k}) & 0 \end{pmatrix}, \tag{2.5}$$

where t is the hopping parameter, $\vec{k}$ the wave vector and

$$S(\vec{k}) = \sum_{\vec{\delta}} e^{i\vec{k}\vec{\delta}} = 2\exp\left(\frac{ik_x a}{2}\right)\cos\left(\frac{k_y a\sqrt{3}}{2}\right) + \exp\left(-ik_x a\right). \tag{2.6}$$

The energy bands derived from this Hamiltonian are:

$$E(\vec{k}) = \pm t|S(\vec{k})| = \pm t\sqrt{3 + f(\vec{k})}, \tag{2.7}$$
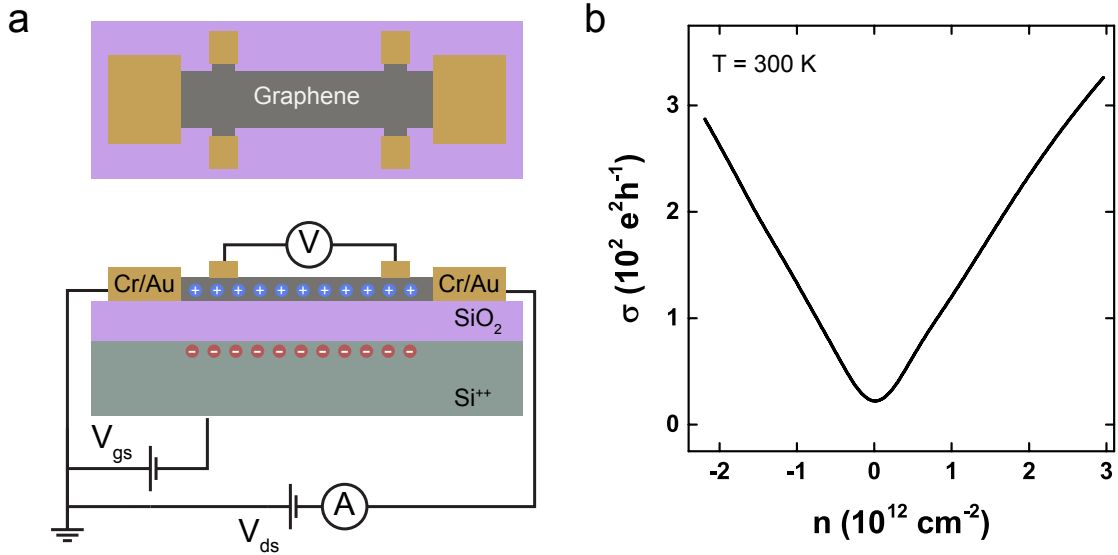
Figure 2.3: **Field-effect transistor.** (a) Schematic of graphene Hall bar device (upper) including electrical connections (lower). (b) Conductivity (σ) vs carrier density (n) for graphene FET at 300 K.

where

$$f(\vec{k}) = 2\cos\left(\sqrt{3}k_y a\right) + 4\cos\left(\frac{\sqrt{3}}{2}k_y a\right)\cos\left(\frac{3}{2}k_x a\right). \tag{2.8}$$

As $S(\vec{K}) = S(\vec{K'}) = 0$ the two bands cross at these points, shown in Figure 2.2b. Figure 2.2c shows the energy spectrum of bulk hBN. Unlike graphene the valence and conduction bands are separated by a forbidden energy gap at the $K(K')$ points. Therefore hBN is an insulator.

Expansion of Equation 2.7 around the Dirac points (K, K') yields linear bands with $E = \pm\hbar v_F |k|$ with the Fermi velocity, $v_F \sim 10^6 \,\mathrm{m\,s^{-1}}$. The Fermi wavevector (k_F) is related to the carrier concentration (n) by:

$$k_F = \sqrt{\frac{4\pi n}{g_s g_v}}, \tag{2.9}$$

where g_s and g_v are the spin and valley degeneracies. Therefore we can relate the Fermi level E_F to n through:

$$E_F = \hbar v_F k_F = \hbar v_F \sqrt{\pi n}. \tag{2.10}$$

The density of states for monolayer graphene is:

$$D(E) = \frac{2}{\pi} \frac{|E|}{\hbar^2 v_F^2}. \tag{2.11}$$

2.1.3   Graphene transistors

Metal-oxide-semiconductor field-effect transistors (MOSFETs) are used to probe the electronic properties of graphene.[8–10] Figure 2.3a shows a schematic of a graphene MOSFET. Graphene is deposited on a silicon substrate capped with a thermally grown oxide (Si^{++}/SiO_2). The thickness of this oxide is chosen such that the optical contrast of graphene is maximised (typically 90 or 290 nm).[11] Metal contacts are deposited and the device is packaged in standard semiconductor chip carriers to connect with measurement equipment. Further details of fabrication methods can be found in later chapters as well as in Appendix A. At the heart of the MOSFET is a metal-oxide-semiconductor structure. Here the metal is the highly doped silicon and the semiconductor is graphene. The physics of such a structure can be explained using a parallel plate capacitor model where the charge per unit area on either plate is: $Q = CV$.[12] Therefore by applying a voltage to the silicon (V_{gs}) a change in carrier density (Δn) of the graphene channel can be induced due to capacitive coupling between the two:

$$\Delta n = \frac{C_g \Delta V_{gs}}{e},\tag{2.12}$$

where the geometric capacitance ($C_g = \varepsilon_0 \varepsilon_r / d$) is approximately $1.19 \times 10^{-8}\,\mathrm{F\,cm^{-2}}$ for 290 nm of SiO_2. For this thickness of SiO_2, V_{gs} is typically limited to $\pm 100\,\mathrm{V}$ which modulates the carrier density by $\Delta n \approx \pm 7.4 \times 10^{12}\,\mathrm{cm^{-2}}$ with the voltage range chosen to prevent dielectric breakdown. Using equation 2.10 the corresponding change in Fermi level is calculated ($E_F = \pm 320\,\mathrm{meV}$).

Figure 2.3b shows the experimentally obtained conductivity of graphene as a function of carrier density with a linear dependence observed for both electron and hole doping. Indeed at high carrier concentrations graphene can be treated as a 2D electron gas with a conductivity describe by the Drude model:

$$\sigma = ne\mu.\tag{2.13}$$

However this assumption breaks down as the carrier concentration approaches zero where graphene has a non-zero minimal conductivity $\sigma_{min} \sim 4e^2/h$.[10]

Graphene has attracted significant attention since the initial experiments over a decade ago.[8–10] The ambipolar field-effect allows the continuous tuning of charge carriers between electrons and holes with room temperature mobilities exceeding $10^5\,\mathrm{cm^2\,V^{-1}\,s^{-1}}$ for high quality graphene devices.[13,14] Unlike other high-mobility materials (e.g. InSb) in graphene an ultra-high mobility is maintained even in doped devices. This allows room temperature ballistic transport to be observed over micrometer length scales.[15] Due to the finite minimum conductivity the ON/OFF ratios in graphene are typically below 10^1 which excludes its use in logic applications though it may prove suitable for high frequency applications.[16] Fundamentally graphene has provided researchers with a system in which physical phenomena such
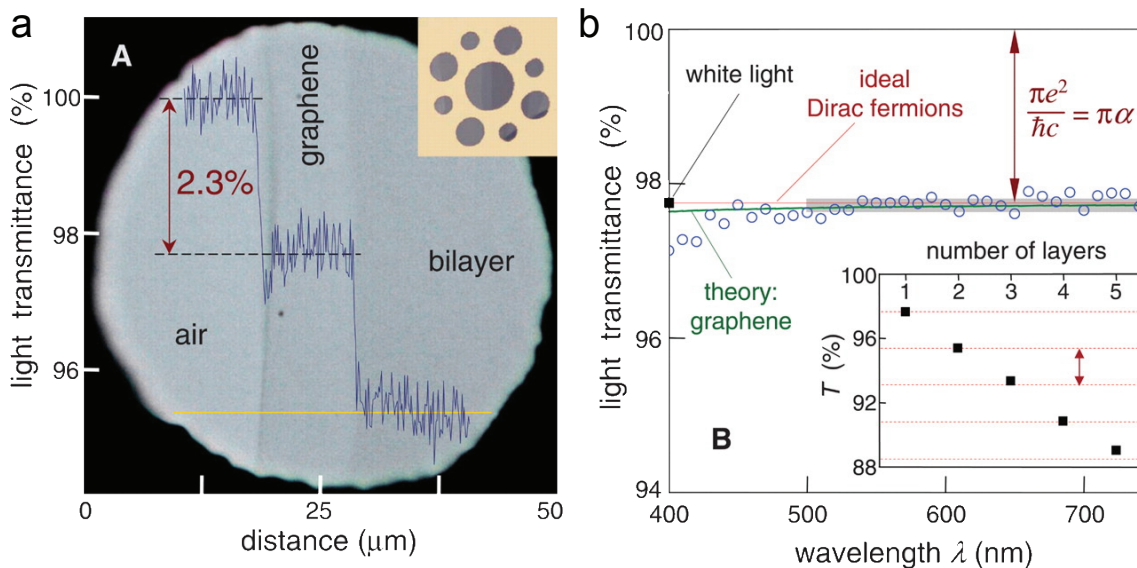
Figure 2.4: **Optical properties of graphene.** (a) Optical micrograph of mono- and bi-layer graphene on metal support (see inset). Line scan profile shows the transmittance along the yellow line. (b) Spectral dependence of transmittance (open circles). Red (green) line indicates behaviour for ideal Dirac fermions (graphene). Inset shows transmittance as a function of layer number. Reproduced with permission.[18]

as the quantum Hall effect can be readily accessed. Indeed there are even proposals to use graphene as a quantum Hall standard.[17]

2.1.4 Optical properties

The band structure of graphene can be approximated by linear Dirac cone around the Fermi energy and the absence of an energy gap allows for uniform absorption across a wide part of the electromagnetic spectrum. Indeed the optical response of graphene is dominated by direct transitions from the valence to conduction band for photon energies above the far-infrared (FIR). Figure 2.4a shows an optical micrograph of mono- and bi-layer graphene suspended on a metal framework with each layer absorbing $\sim 2.3\%$ of light. Interestingly within the linear energy range this value is independent of frequency, Figure 2.4b. From the tight-binding model this universal conductance can be determined by fundamental constants $\sigma(\omega) = \pi e^2/2h$, producing an absorbance of $A(\omega) = 4\pi/c \cdot \sigma(\omega) = \pi\alpha \approx 2.3\%$ where α is the fine structure constant.[18] Electrical doping can shift the Fermi energy by hundreds of meV which can dramatically change the optical absorption through Pauli blocking. In such a scenario optical transitions are suppressed for photon energies below $|2E_F|$.
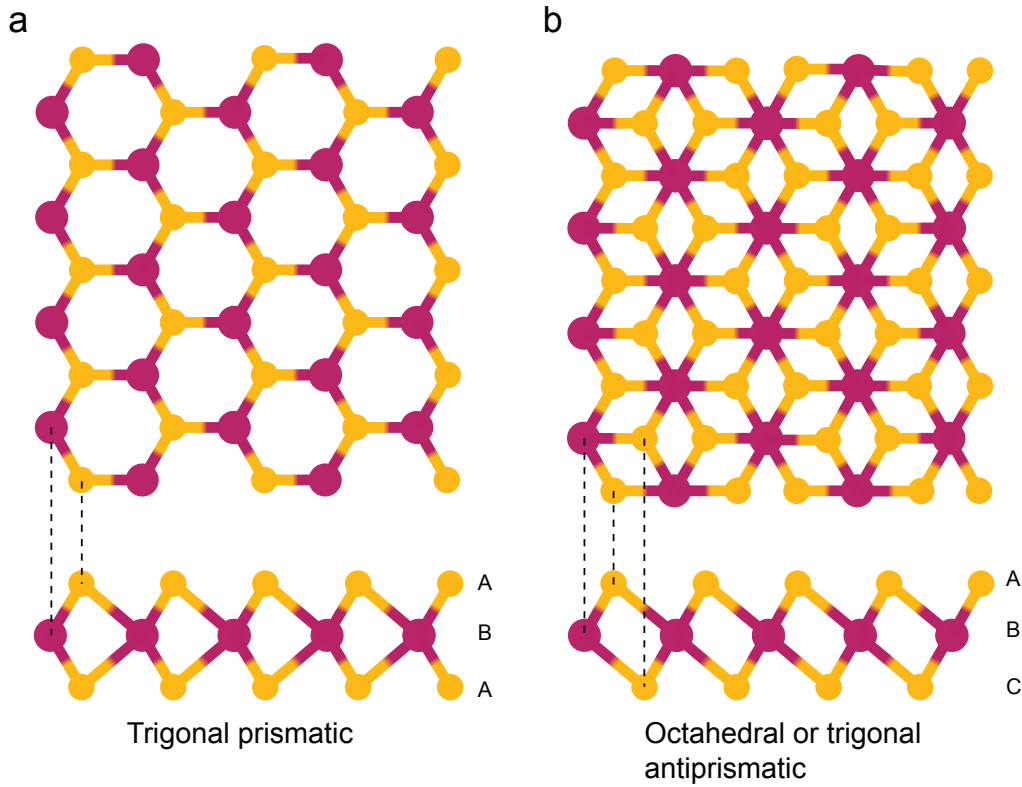
Figure 2.5: **TMD crystal structure.** Trigonal (a) and octahedral (b) atomic coordination as viewed out-of-plane (top) and in-plane (bottom). Transition metal atoms are purple, chalcogen atoms are yellow.

2.2   Transition metal dichalcogenides

Transition metal dichalcogenides (TMDs) are part of the 2D material family that, like graphene, can be exfoliated into atomically thin crystals. Of particular interest are the semiconducting TMDs as the presence of an energy gap in their band structure has a profound influence on their electrical and optical properties.[19,20] Figure 2.5 shows the lattice structure of a prototypical TMD, MX_2, where M represents a transition metal (M = M, W) and X a chalcogen (X = S, Se). Here the metal atom is sandwiched between two chalcogen atoms with both species arranged on triangular lattices. From an out of plane perspective a hexagonal lattice similar to graphene is seen though in this system a monolayer consists of three atomic planes giving a thickness of $\sim 6\,\text{Å}$. The intralayer M-X bonds are covalent whereas adjacent MX_2 layers are weakly coupled by van der Waals forces. The metal and chalcogen atoms can arrange in different coordinations with the most common the trigonal and octahedral, shown in Figure 2.5.[19]

   A theoretical description of the band structure of TMDs requires the use of relativistic Density Functional Theory (DFT) due the intrinsic spin-orbit coupling.[21] Figure 2.6a shows the band structure of MoS_2 as the thickness is reduced from bulk to monolayer. For n-layers (where n$\geq$ 2) the lowest energy transition is indirect and

originates from the valence band maximum found at the Γ point. However upon reducing $n = 1$ this transition is direct with the valence band maximum now found at K.

The semiconducting nature of TMDs make them suitable in transistor logic applications. Figure 2.6b shows the room temperature transconductance of monolayer WS_2. As gate voltage is swept from $-60\,\text{V} < V_{gs} < 60\,\text{V}$ the source-drain current increases from $10^{-11}\,\text{A}$ to $> 10^{-5}\,\text{A}$ giving an ON/OFF ratio greater than 10^6. In Figure 2.6c strong photoluminescence of WSe_2 is observed due to the direct transition which favours the radiative recombination of photo-excited charges. The absorption spectra of TMDs exhibit sharp resonance features that correspond to excitonic transitions. Excitons are quasi-particles that exist because of the Coulomb attraction between photoexcited electron-hole pairs, see inset Figure 2.6c. For monolayer TMDs theoretical calculations predict large exciton binding energies ($E_B = 0.5 - 1\,\text{eV}$), due to reduced dielectric screening, which is an order of magnitude larger than those found in conventional semiconductors.[20,23] This allows the observation of excitonic effects at room temperature.

The direct bandgap in monolayer TMDs occurs at the K and K' points in the hexagonal Brillouin zone. Having two or more minima in the conduction band at equal energies but at different positions in momentum space gives electrons a valley degree of freedom (DOF).[25] Unlike graphene, monolayer TMDs lack a centre of inversion symmetry which means that electrons with different momenta have a different energy spectrum. Figure 2.7a shows that the origin of the lack of inversion symmetry in monolayer TMDs arises because the metal and chalcogen atoms lie in different planes. Inverting a vector that points from the centre to a chalcogen atom will point to a vacant site. Inversion symmetry breaking leads to valley-dependent optical selection rules at the K and K' points due to the contrasting circular dichroism at opposing points in momentum space, see Figure 2.7b.[26] Incoming circularly polarized light will excite electrons of a particular spin and due to spin-orbit coupling this will define the momentum of the electron. Spin-orbit coupling arises from the d-orbitals of the transition metals and causes the conduction and valence bands to become spin split. For instance, left-handed or negative helicity (σ^-) photons will excite spin-up electrons at the K point. Right-handed or positive helicity (σ^+) photons of the same energy (e.g. red arrows) will excite spin-down electrons at the K' point.[27-29] These findings could allow the realisation of valleytronic devices whereby the population of one valley or another could be used to store and manipulate information.[20,23]
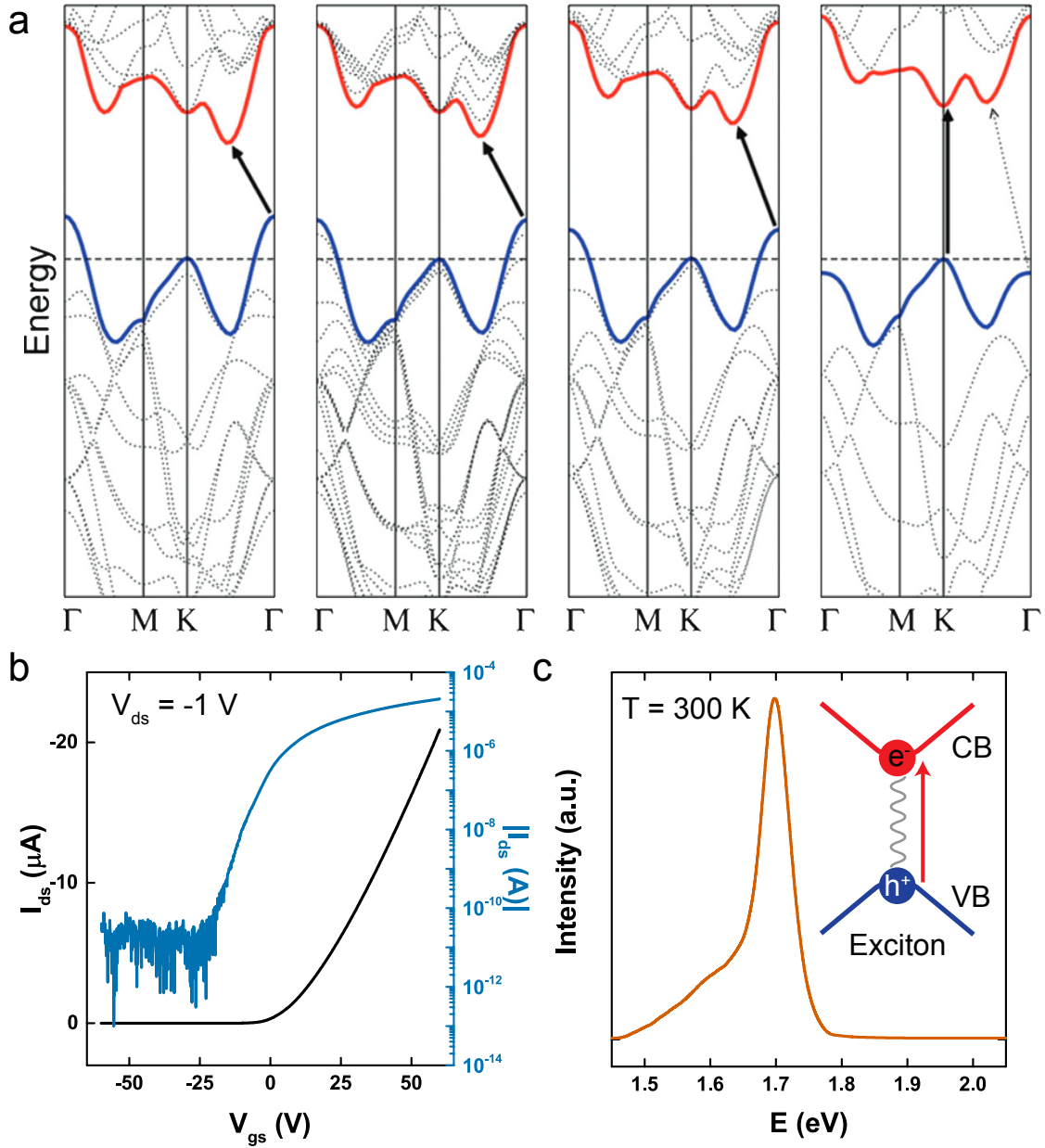
Figure 2.6: **TMD band structure and optoelectronic properties.** (a) MoS_2 band structure for bulk, quad-layer, bi-layer and monolayer (from left to right). Adapted with permission.[22] (b) Transconductance of WS_2 monolayer FET. (c) Room temperature photoluminescence of monolayer WSe_2. The inset illustrates the formation of an exciton due to the Coulomb attraction between a photoexcited electron-hole pair.
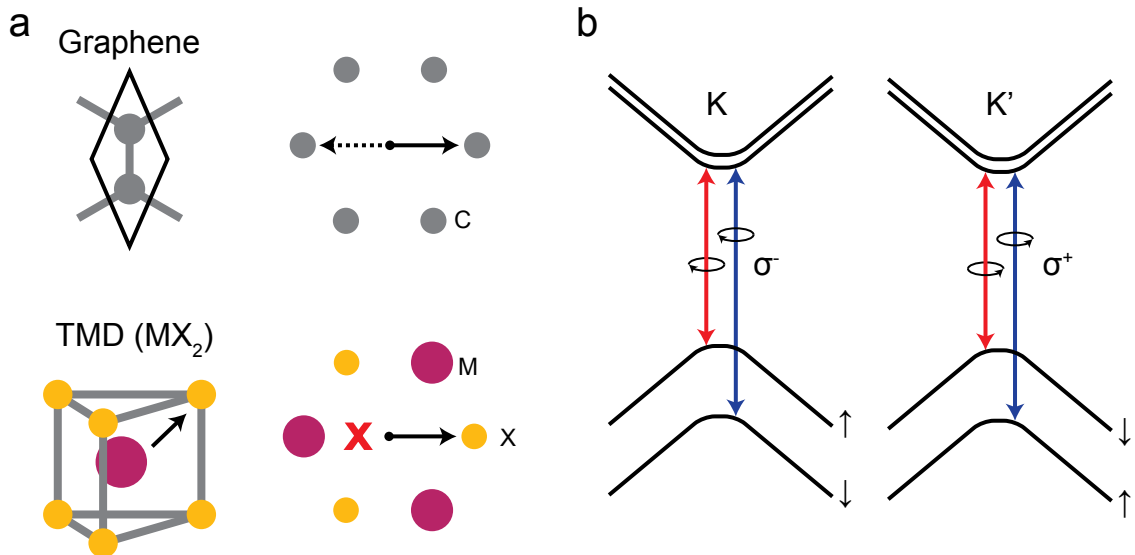
Figure 2.7: **Inversion symmetry and valley selection rules.** (a) The unit cell of graphene contains two carbon atoms (grey spheres). Graphene has inversion symmetry because any vector (black arrow) from the centre point (black circle) to a carbon atom can be inverted and still point to a carbon atom. To break inversion symmetry the two sublattices have to become inequivalent.[24] In TMDs the metal (M, maroon spheres) and chalcogen (X, yellow spheres) atoms lie in different planes. Inverting a vector that points from the centre to a chalcogen atom will point to a vacant site - resulting in a lack of inversion symmetry. (b) The lack of inversion symmetry gives rise to valley optical selection rules. Incoming circularly polarized light will excite electrons of a particular spin and due to spin-orbit coupling this will define the momentum of the electron.

2.3 van der Waals heterostructures

Layer-by-layer assembly of 2D materials can be used to produce complicated heterostructures. Unlike traditional 3D heterostructures, those based on atomically thin materials are primarily driven by interface effects due to the absence of bulk material, with this interlayer interaction able redistribute charges and induce structural changes. The strength of this interaction is governed by the alignment (or misalignment) of the crystallographic axes of one layer with those of another layer.[30]

Indeed this emerging field of research has already proved fruitful with the creation of high-quality electronic devices,[14,31] that has enabled the observation of several physical phenomena including Hofstadters' butterfly,[32–34] topological currents,[35] and even unconventional superconductivity.[36]

2.4 Optoelectronic Devices

Figure 2.8 shows a number of optoelectronic devices based on 2D materials. These include those based on a single material where the active area could be confined to interfaces with metal electrodes or extended to encompass the entire channel, Figure
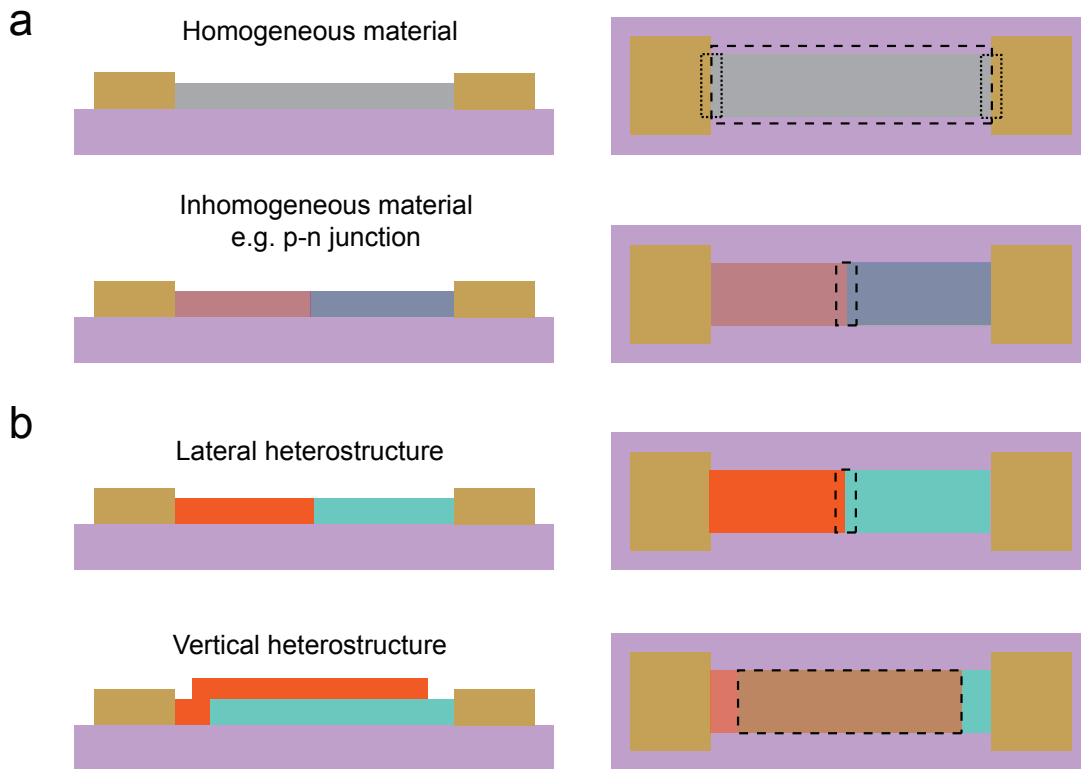
Figure 2.8: **Optoelectronic device structures.** (a) Homogeneous channel material (upper) can be doped (e.g. chemically) to create junctions within material (lower). (b) Two atomically thin materials combined as lateral (upper) or vertical heterostructures (lower) form the channel. Side view of structures shown on left, top view on right. The dashed lines indicate the active area which can be confined to the contacts (dotted line).

2.8a. Through localised electrical or chemical control of doping, interfaces can be formed and dynamically controlled within the material creating, for example, pn-junctions - an essential optoelectronic device. Combinations of two or more materials allows the creation of heterostructure devices in which the interfaces are lateral or vertical. Large active areas can be achieved in the latter as shown schematically in Figure 2.8b.

2.4.1   Figures of Merit

To make a comparison of the different types of photodetectors as well as the choice of photoactive material one first needs to explain the different terminology used, discuss the spectral response of the device, and provide standardized figures of merit. Here, the most relevant figures of merit are discussed.[37–39] The basic measurement principle of a photodetector is recording the electrical response to an optical signal which can vary in power, wavelength, and modulation frequency. The electrical response to these variations depends on the photoactive material and the photodetection mechanism. Typically the entire device can be illuminated, known as flood illumination, or

Table 2.1: Common figures of merit for photodetectors

Metric	Symbol	Equation[a]	Units
External Quantum Efficiency	η_e, EQE	$(I_{pc}/q)/\phi_{in}$	-
Internal Quantum Efficiency	η_i, IQE	$(I_{pc}/q)/\phi_{abs}$	-
Gain	G	$\mu\tau E/L$	-
Responsivity	R	I_{pc}/P_{opt}	A/W
Bandwidth (-3 dB)	f_{-3dB}	$\sim 0.35/\tau$	Hz
Noise Equivalent Power	NEP	S_A/R	$W/\sqrt{Hz}$
Detectivity	D^*	$\sqrt{A}/NEP$	$cm\sqrt{Hz}/W$
Linear Dynamic Range	LDR	$10 \times \log_{10}(P_{sat}/NEP)$	dB

[a] Unless other units specified; I_{pc} = photocurrent, ϕ_{in} = incident photon flux, ϕ_{abs} = absorbed photon flux, μ = free carrier mobility, τ = photoexcited carrier lifetime, E = electric field across channel of length L, $P_{opt}/A = \phi_{in}hc/\lambda$ = optical power density, A = device area, S_A noise spectral density (current), P_{sat} = saturation power.

regions locally illuminated under a focussed beam. To experimentally determine the spatial origin of the photoresponse a laser is often used to illuminate at sub-micron scales in techniques such as scanning photocurrent microscopy (SPCM).

Table 2.1 provides a summary of the key figures of merit. The external/internal quantum efficiency (EQE/IQE) describes the number of electrons extracted at the electrodes per incident/absorbed photon. For efficiencies greater than 1 a gain (G) mechanism is required. This requires an imbalance between the mobile carrier transit time and trapped carrier lifetime (τ). The transit time ($t_r = L/\mu E$) is the time taken for a carrier with mobility μ to travel between electrodes separated by a distance L under an applied electric field E. Responsivity ($R = I_{pc}/P_{opt}$) is the ratio between photocurrent and incident optical power, measured in units of A/W. The -3 dB bandwidth is the modulation frequency at which the output power drops by 1/2. This can be used to estimate the response time of the device using $f_{-3dB} \sim 0.35/\tau$. Noise is present in all electronic devices. To quantify this the noise spectral density ($S_{A(V)}$) is acquired by taking a Fourier transform of the current (voltage) over a given time interval. In photodetectors the Noise Equivalent Power ($NEP = S_A/R$) is defined as the optical power that gives a signal-to-noise ratio of 1 (at 1 Hz bandwidth). As the NEP scales with the square-root of device area (A) the specific detectivity is used, $D^* = \sqrt{A}/NEP$. Generally it should be specified at which wavelength and modulation frequency these values are reported. Finally the linear dynamic range is the decades over which the electrical response is linear with optical power. Defined as $LDR = 10 \times 10 \log_{10}(P_{sat}/NEP)$ where P_{sat} is the power at which the response deviates from this linearity.
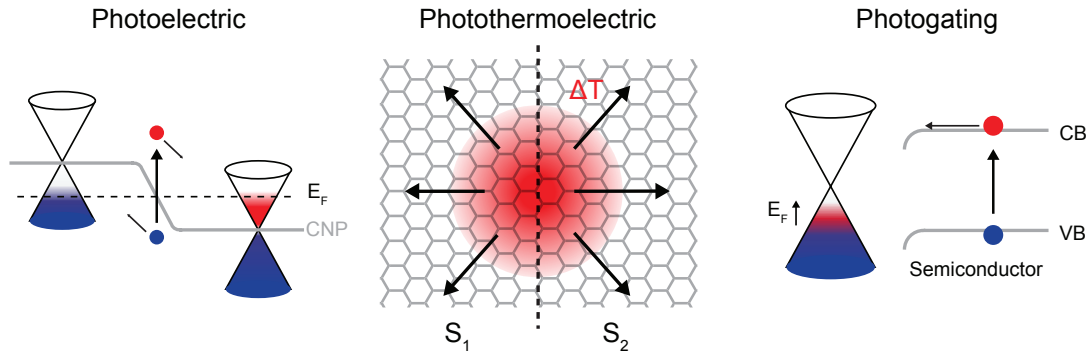
Figure 2.9: **Photodetection mechanisms.** Photovoltaic (a), photothermoelectric (b) and photogating (c) effects. ΔT is electron temperature, $S_{1,2}$ are Seebeck coefficients, E_F Fermi level, CNP charge neutrality point, CB (VB) is the conduction (valence) band level.

2.4.2 Origin of Noise

Noise is omnipresent in all measurements and manifests from a number of different mechanisms. Johnson or thermal noise arises due to random motion of charge carriers which for a resistor (R) at temperature (T) is $S_v = 4k_bTR\Delta f$, where Δf is the bandwidth over which the noise is measured. This is present in the absence of current flow. Flicker noise, also known as 1/f or pink noise, has a power dependence on the inverse of frequency (i.e. 1/f). The physical origin of 1/f noise is unclear though it is usually found at $f < 100$ kHz. This is the dominant source of noise in graphene.[40] In semiconductors free carrier densities constantly fluctuate through various generation and recombination (G-R) processes. G-R noise typically originates from inter-band or trap state transitions.[37] Shot noise is the random fluctuations in the number of electrons or photons because of their discrete nature, $I_{shot}^2 = 2qI\Delta f$. Other sources often dominate over shot noise with exceptions found in measurements at high frequencies and low temperatures.

2.5 Photodetection mechanisms

To create atomically thin photodetectors the mechanisms behind their photo-detection must be understood. In this section the main detection mechanisms for graphene-based photodetectors are outlined which can be readily extended to TMDs.

2.5.1 Photoelectric effect

In the photoelectric effect to generate a photocurrent charge carriers have to be photoexcited, separated and extracted at the electrodes. This separation occurs at built-in electric fields provided by a difference in doping between regions, Figure 2.9a. These can be created at pn-junctions within graphene or at metal-graphene

interfaces. Subsequent extraction occurs either through diffusion in short-circuit configuration or by applying an external source-drain bias.[41] In the literature surrounding graphene-based photodetectors this is also known as the 'photovoltaic effect'.

2.5.2 Photothermoelectric Effect

At a junction between two materials with different Seebeck coefficients a voltage is generated when the materials are held at different temperatures.[42] In graphene absorption of light creates a population of hot carriers with a temperature above that of the lattice. When illuminating an interface between two regions with different Seebeck coefficients ($S_{1,2}$) a photovoltage is generated (ΔV), see Figure 2.9b. Therefore:

$$\Delta V = (S_1 - S_2)\Delta T, \tag{2.14}$$

where the sign is dictated by either gradients. This is known as photothermoelectric effect (PTE). The Seebeck coefficient can be expressed using the Mott relation[43,44]:

$$S = -\frac{\pi^2}{3e}\frac{k_b^2 T_e}{\sigma(\mu)}\left.\frac{\partial \sigma(E)}{\partial E}\right|_{E=E_F} = \frac{2\pi^2 k_B T_e}{3q T_F}, \tag{2.15}$$

where T_e is the electron temperature, $T_F = E_F/k_B$ the Fermi temperature, q the electron charge and k_B the Boltzmann constant. Equation 2.15 assumes that the mobility is independent of Fermi energy E_F. The Seebeck coefficient can be tuned with gate voltage reaching $S \sim 100\,\mu\text{V}\,\text{K}^{-1}$ at room temperature,[45] with the sign determined by whether the charge carriers are electrons or holes.[44]

In steady-state conditions the energy given to hot carriers is $P_{opt} \propto C_h T_h$ where P_{opt} is the incident optical power and C_h the heat capacity, which scales as $C_h \propto T_h^2$. The supercollision model of hot carrier cooling in graphene predicts a photocurrent power dependence of:[46,47]

$$I_{PTE} \propto (P_{\text{opt}})^{\frac{2}{3}}. \tag{2.16}$$

Equation 2.16 assumes that hot carriers thermalise at temperatures far greater than the lattice temperature (T_l), $T_h \gg T_l$. In principle measurement of this power dependence could be used to determine the photogeneration mechanism. However at room temperature this assumption often breaks down (as $T_h - T_l \ll T_l$) and the exponent becomes ~ 1.[46,47] Correct determination of the PTE effect requires independent electrostatic control of carrier concentrations in two regions. From this a distinctive six-fold photocurrent pattern is observed corresponding to p-n, p-p', p'-p, n-p, n-n' and n'n junctions.[48]

2.5.3   Photogating Effect

To increase the absorption of graphene-based photodetectors a semiconducting material is placed in close proximity to the graphene channel. Upon illumination a photoexcited charge carrier is transferred from the semiconductor to graphene. This changes the carrier density in the graphene FET which manifests in electrical measurements as a shift in the charge neutrality point (V_{CNP}) - effectively a photo-activated gate, hence the name. Such a system can be treated as a photoconductor with distinct light-absorbing and current-carrying regions. The photocurrent (I_{pc}) flowing in a device of area $A = WL$ and thickness D is described by:[49]

$$I_{pc} = (\sigma E)WD = (q\mu n E)WD, \tag{2.17}$$

where σ is the conductivity, E the electric field across channel and μ the mobile carrier mobility, with the following definition for the number of photogenerated carriers (n);

$$n = \frac{\eta(P_{opt}/h\nu)\tau}{WLD}, \tag{2.18}$$

which includes the number of incident photons ($P_{opt}/h\nu$), quantum efficiency (η) and recombination rate ($1/\tau$). By using the earlier definition of responsivity ($R = I_{pc}/P_{opt}$) we arrive at:

$$R = \left(\frac{q}{h\nu}\right)\eta\left(\frac{\mu\tau E}{L}\right) = \left(\frac{q}{h\nu}\right)\eta G. \tag{2.19}$$

The responsivity of a typical hybrid graphene photodetector depends on 3 terms: the first is comprised of physical constants whilst the second and third terms relate to the quantum efficiency and gain of the system respectively, both of which need to be maximised.

Light will be absorbed by a semiconductor if the incident photons have energy greater than the band gap ($h\nu \geq E_g$). In this case electron-hole pairs are generated which form an exciton with an intrinsic efficiency, (η_{gen}) that relates to the absorption coefficient of the material. To create free charges the Coulomb force between electron and hole must be overcome. This can happen under the influence of large electric fields or due to thermal energy and this process has an associated efficiency term (η_{diss}). Charges are transferred between semiconductor and graphene in the presence of a potential barrier at the semiconductor-graphene interface or from a charge trapping mechanism in the semiconductor. In addition clean interfaces are required for efficient charge transfer (η_{trans}). Therefore the quantum efficiency can be split into three terms:

$$\eta = \eta_{gen}\eta_{diss}\eta_{trans} \tag{2.20}$$

Applying a bias voltage to the graphene channel allows the transferred charge to be extracted at the drain contact. To preserve electrical neutrality a charge must be simultaneously injected at the source. This process of charge recirculation can occur multiple times before eventual recombination with the trapped charge which we can identify as the gain term in equation 2.19. To achieve the largest gain the ratio between the trapped carrier lifetime (τ) and free carrier transit time ($t_{tr} = L/\mu E$) must be maximised:

$$G = \frac{\tau}{t_{tr}}. \tag{2.21}$$

Long-lived charge trapping is achieved by the spatial separation of photoexcited charges across the interface as explained above. Clearly the magnitude of τ provides the limit on the photodetector response time and as such there is a trade-off between gain and bandwidth. To minimise the transit time we require a high mobility channel, short electrode spacing and large electric fields. Graphene is the most promising material to achieve these conditions because of the unique situation in which an ultra-high carrier mobility can be accessed at the surface with micron scaled devices readily fabricated using standard electron-beam lithography techniques.

2.6 Literature review of graphene-based photodetectors

Given the rapid progress in the field of graphene-based photodetectors it is worthwhile to present a summary of the available literature. Figure 2.10 presents several plots each of which compare two key figures of merit from Section 2.4.1. The data for this figure can be found in Table B.1 (Appendix B) and was acquired from journal papers published between 2010 and 2017. Figure 2.10a shows a comparative plot of responsivity against bandwidth. Pristine graphene photodetectors have been shown to operate at GHz frequencies though their responsivity is limited by low absorption.[50] Increased responsivities are reported for both chemical functionalisation and by combining with semiconducting materials - although this is at the cost of bandwidth. The low NEP in graphene-hybrid detectors results in a system with large LDR and high responsivity, Figure 2.10b. A large LDR can be achieved in functionalised graphene photodetectors although these typically have a lower responsivity. In terms of spectral response, Figure 2.10c shows that both type of detectors are suited to a very wide range of incident photon energy. Interestingly GO photodetectors are capable of detecting light from UV to THz energies in spite of their generally poorer performance.

Due to their atomically thin nature graphene-based photodetectors are promising for next-generation flexible and wearable electronics. Furthermore they could

introduce functionalities not available in bulk semiconductors such as polarisation sensitivity and strain tunable response.[20] Hybrid graphene photodetectors can already outperform conventional CMOS based technology with a spectral range that extends into the MIR. As more than 2,000 layered materials have been identified so far optoelectronic devices based on two-dimensional materials and their heterostructures will be a rich topic of investigation for many years to come.
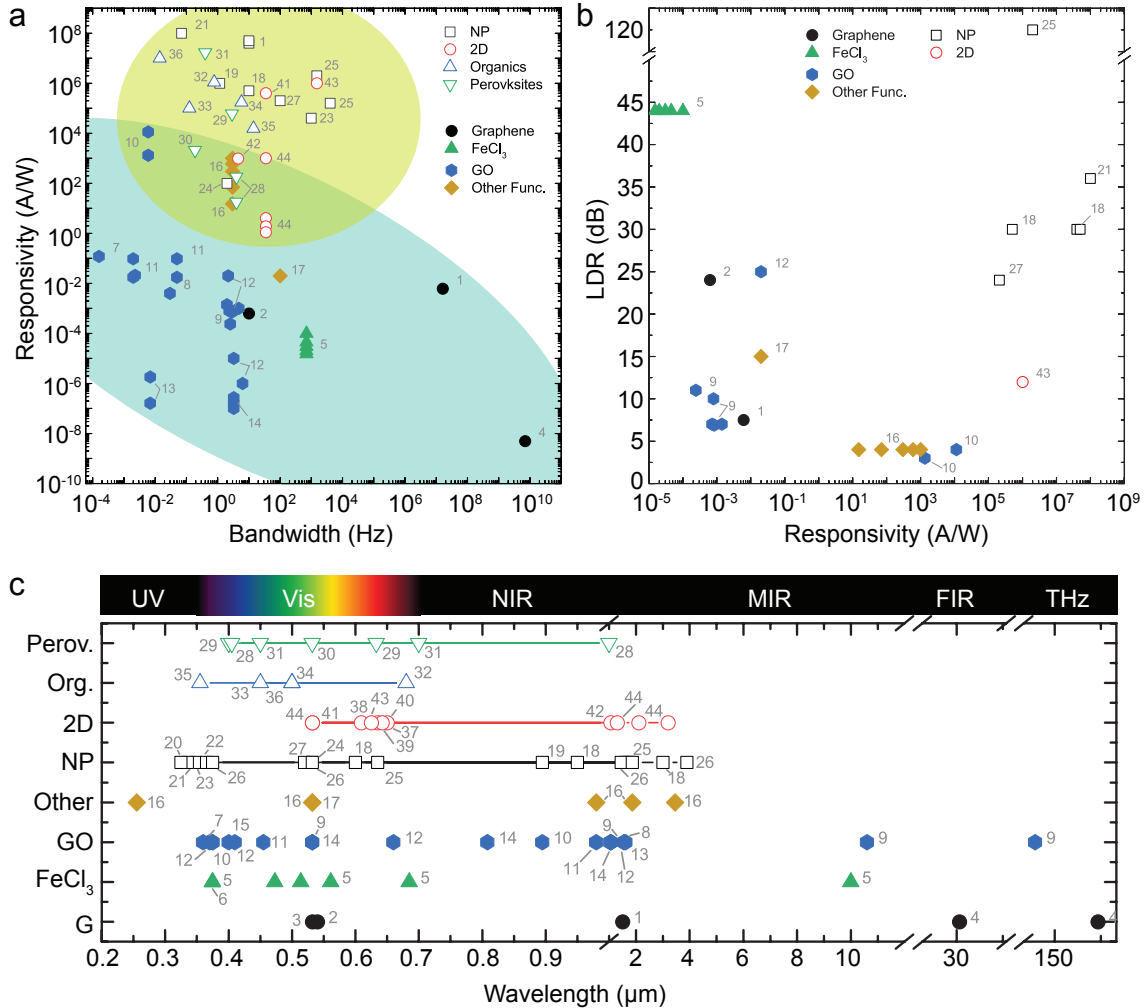
Figure 2.10: **Literature review of graphene based photodetectors and comparison of performance** (a) Responsivity vs bandwidth and (b) LDR vs responsivity for functionalised (filled symbols) and heterostructure (open symbols) graphene photodetectors. (c) Measured operational wavelength for different graphene-based photodetectors. Points are fixed wavelength whereas lines represent spectral scans. The number associated with each point relates to the reference found in Table B.1 (Appendix B) where the complete data set can be found. NP = nanoparticles, 2D = TMD heterostructures.

References

[1] P. R. Wallace. The Band Theory of Graphite. *Physical Review*, 71(9):622–634, may 1947.

[2] M. I. Katsnelson. Zitterbewegung, chirality, and minimal conductivity in graphene. *The European Physical Journal B*, 51(2):157–160, may 2006.

[3] A. H.. Castro Neto, F. Guinea, NMR M. R.. Peres, K. S.. Novoselov, and A. K.. Geim. The electronic properties of graphene. *Reviews of Modern Physics*, 81(1):109–162, jan 2009.

[4] E. Doni and G. Pastori Parravicini. Energy bands and optical properties of hexagonal boron nitride and graphite. *Il Nuovo Cimento B Series 10*, 64(1):117–144, nov 1969.

[5] Yong-Nian Xu and W. Y. Ching. Calculation of ground-state and optical properties of boron nitrides in the hexagonal, cubic, and wurtzite structures. *Physical Review B*, 44(15):7787–7798, oct 1991.

[6] M. Topsakal, E. Aktürk, and S. Ciraci. First-principles study of two- and one-dimensional honeycomb structures of boron nitride. *Physical Review B*, 79(11):115442, mar 2009.

[7] Oded Hod. Graphite and Hexagonal Boron-Nitride have the Same Interlayer Distance. Why? *Journal of Chemical Theory and Computation*, 8(4):1360–1369, apr 2012.

[8] Konstantin S Novoselov, A K Geim, S V Morozov, D Jiang, Y Zhang, S V Dubonos, I V Grigorieva, and A A Firsov. Electric Field Effect in Atomically Thin Carbon Films. *Science*, 306(5696):666–669, oct 2004.

[9] Zhang Yuanbo, Tan Yan-Wen, Horst L Stormer, and Philip Kim. Experimental observation of the quantum Hall effect and Berry's phase in graphene. *Nature*, 438(7065):201–204, nov 2005.

[10] K S Novoselov, A K Geim, S V Morozov, D Jiang, M I Katsnelson, I V Grigorieva, S V Dubonos, and A A Firsov. Two-dimensional gas of massless Dirac fermions in graphene. *Nature*, 438(7065):197–200, nov 2005.

[11] P. Blake, E. W. Hill, A. H. Castro Neto, K. S. Novoselov, D. Jiang, R. Yang, T. J. Booth, and A. K. Geim. Making graphene visible. *Applied Physics Letters*, 91(6):063124, aug 2007.

[12] DA Neamen. *Semiconductor physics and devices, 3rd edition*. 2003.

[13] K.I. Bolotin, K.J. Sikes, Z. Jiang, M. Klima, G. Fudenberg, J. Hone, P. Kim, and H.L. Stormer. Ultrahigh electron mobility in suspended graphene. *Solid State Communications*, 146(9-10):351–355, jun 2008.

[14] L Wang, I. Meric, P. Y. Huang, Q. Gao, Y. Gao, H. Tran, T. Taniguchi, K. Watanabe, L. M. Campos, D. A. Muller, J. Guo, P. Kim, J. Hone, K. L. Shepard, and C. R. Dean. One-Dimensional Electrical Contact to a Two-Dimensional Material. *Science*, 342(6158):614–617, nov 2013.

[15] Alexander S. Mayorov, Roman V. Gorbachev, Sergey V. Morozov, Liam Britnell, Rashid Jalil, Leonid A. Ponomarenko, Peter Blake, Kostya S. Novoselov, Kenji Watanabe, Takashi Taniguchi, and A. K. Geim. Micrometer-Scale Ballistic Transport in Encapsulated Graphene at Room Temperature. *Nano Letters*, 11(6):2396–2399, jun 2011.

[16] K. S. Novoselov, V. I. Falko, L. Colombo, P. R. Gellert, M. G. Schwab, and K. Kim. A roadmap for graphene. *Nature*, 490(7419):192–200, oct 2012.

[17] R. Ribeiro-Palau, F. Lafont, J. Brun-Picard, D. Kazazis, A. Michon, F. Cheynis, O. Couturaud, C. Consejo, B. Jouault, W. Poirier, and F. Schopfer. Quantum Hall resistance standard in graphene devices under relaxed experimental conditions. *Nature Nanotechnology*, 10(11):965–971, nov 2015.

[18] R. R. Nair, P. Blake, A. N. Grigorenko, K. S. Novoselov, T. J. Booth, T. Stauber, N. M R Peres, and A. K. Geim. Fine Structure Constant Defines Visual Transparency of Graphene. *Science*, 320(5881):1308–1308, jun 2008.

[19] Manish Chhowalla, Hyeon Suk Shin, Goki Eda, Lain-Jong Li, Kian Ping Loh, and Hua Zhang. The chemistry of two-dimensional layered transition metal dichalcogenide nanosheets. *Nature Chemistry*, 5(4):263–275, 2013.

[20] Fengnian Xia, Han Wang, Di Xiao, Madan Dubey, and Ashwin Ramasubramaniam. Two-dimensional material nanophotonics. *Nature Photonics*, 8(12):899–907, nov 2014.

[21] Z. Y. Zhu, Y. C. Cheng, and U. Schwingenschlögl. Giant spin-orbit-induced spin splitting in two-dimensional transition-metal dichalcogenide semiconductors. *Physical Review B*, 84(15):153402, oct 2011.

[22] Andrea Splendiani, Liang Sun, Yuanbo Zhang, Tianshu Li, Jonghwan Kim, Chi Yung Chim, Giulia Galli, and Feng Wang. Emerging photoluminescence in monolayer MoS2. *Nano Letters*, 10(4):1271–1275, 2010.

[23] Kin Fai Mak and Jie Shan. Photonics and optoelectronics of 2D semiconductor transition metal dichalcogenides. *Nature Photonics*, 10(4):216–226, 2016.

[24] Wang Yao, Di Xiao, and Qian Niu. Valley-dependent optoelectronics from inversion symmetry breaking. *Physical Review B*, 77(23):235406, jun 2008.

[25] A. Rycerz, J. Tworzydło, and C. W. J. Beenakker. Valley filter and valley valve in graphene. *Nature Physics*, 3(3):172–175, mar 2007.

[26] Di Xiao, Gui-Bin Liu, Wanxiang Feng, Xiaodong Xu, and Wang Yao. Coupled Spin and Valley Physics in Monolayers of MoS 2 and Other Group-VI Dichalcogenides. *Physical Review Letters*, 108(19):196802, may 2012.

[27] Hualing Zeng, Junfeng Dai, Wang Yao, Di Xiao, and Xiaodong Cui. Valley polarization in MoS2 monolayers by optical pumping. *Nature Nanotechnology*, 7(8):490–493, aug 2012.

[28] Kin Fai Mak, Keliang He, Jie Shan, and Tony F. Heinz. Control of valley polarization in monolayer MoS2 by optical helicity. *Nature Nanotechnology*, 7(8):494–498, aug 2012.

[29] Ting Cao, Gang Wang, Wenpeng Han, Huiqi Ye, Chuanrui Zhu, Junren Shi, Qian Niu, Pingheng Tan, Enge Wang, Baoli Liu, and Ji Feng. Valley-selective circular dichroism of monolayer molybdenum disulphide. *Nature Communications*, 3(1):887, jan 2012.

[30] K. S. Novoselov, A. Mishchenko, A. Carvalho, and A. H. Castro Neto. 2D materials and van der Waals heterostructures. *Science*, 353(6298):aac9439, jul 2016.

[31] C R Dean, a F Young, I Meric, C Lee, L Wang, S Sorgenfrei, K Watanabe, T Taniguchi, P Kim, K L Shepard, and J Hone. Boron nitride substrates for high-quality graphene electronics. *Nature nanotechnology*, 5(10):722–726, oct 2010.

[32] B. Hunt, J. D. Sanchez-Yamagishi, A. F. Young, M. Yankowitz, B. J. LeRoy, K. Watanabe, T. Taniguchi, P. Moon, M. Koshino, P. Jarillo-Herrero, and R. C. Ashoori. Massive Dirac Fermions and Hofstadter Butterfly in a van der Waals Heterostructure. *Science*, 340(6139):1427–1430, jun 2013.

[33] C. R. Dean, L. Wang, P. Maher, C. Forsythe, F. Ghahari, Y. Gao, J. Katoch, M. Ishigami, P. Moon, M. Koshino, T. Taniguchi, K. Watanabe, K. L. Shepard, J. Hone, and P. Kim. Hofstadter's butterfly and the fractal quantum Hall effect in moiré superlattices. *Nature*, 497(7451):598–602, may 2013.

[34] L. A. Ponomarenko, R. V. Gorbachev, G. L. Yu, D. C. Elias, R. Jalil, A. A. Patel, A. Mishchenko, A. S. Mayorov, C. R. Woods, J. R. Wallbank, M. Mucha-Kruczynski, B. A. Piot, M. Potemski, I. V. Grigorieva, K. S. Novoselov, F. Guinea, V. I. Fal'ko, and A. K. Geim. Cloning of Dirac fermions in graphene superlattices. *Nature*, 497(7451):594–597, may 2013.

[35] R. V. Gorbachev, J. C. W. Song, G. L. Yu, A. V. Kretinin, F. Withers, Y. Cao, A. Mishchenko, I. V. Grigorieva, K. S. Novoselov, L. S. Levitov, and A. K. Geim. Detecting topological currents in graphene superlattices. *Science*, 346(6208):448–451, oct 2014.

[36] Yuan Cao, Valla Fatemi, Shiang Fang, Kenji Watanabe, Takashi Taniguchi, Efthimios Kaxiras, and Pablo Jarillo-Herrero. Unconventional superconductivity in magic-angle graphene superlattices. *Nature*, 556(7699):43–50, mar 2018.

[37] T. S. Moss, G. J. Burrell, B. Ellis, and M. Ali Omar. *Semiconductor Opto-Electronics*, volume 27. Butterworth & Co. (Publishers) Ltd, London, 1974.

[38] N. C L Hess, D. J. Carlson, J. D. Inder, E. Jesulola, J. R. Mcfarlane, and N. A. Smart. *Clinically meaningful blood pressure reductions with low intensity isometric handgrip exercise. A randomized trial*, volume 65. Cambridge University Press, Cambridge, 2016.

[39] Yugang Sun and John A. Rogers. *Semiconductor Nanomaterials for Flexible Technologies: From Photovoltaics and Electronics to Sensors and Energy Storage*. Elsevier, London, 2010.

[40] Alexander A Balandin. Low-frequency 1/f noise in graphene devices. *Nature Nanotechnology*, 8(8):549–555, aug 2013.

[41] F. H. L. Koppens, T Mueller, Ph. Avouris, a C Ferrari, M S Vitiello, and M Polini. Photodetectors based on graphene, other two-dimensional materials and hybrid systems. *Nature Nanotechnology*, 9(10):780–793, oct 2014.

[42] T. J. Seebeck. Ueber die magnetische Polarisation der Metalle und Erze durch Temperatur-Differenz. *Annalen der Physik*, 82(2):133–160, jan 1826.

[43] Melvin Cutler and N. F. Mott. Observation of Anderson Localization in an Electron Gas. *Physical Review*, 181(3):1336–1340, may 1969.

[44] E. H. Hwang, E. Rossi, and S. Das Sarma. Theory of thermopower in two-dimensional graphene. *Physical Review B - Condensed Matter and Materials Physics*, 80(23):1–5, 2009.

[45] K. J. Tielrooij, L. Piatkowski, M. Massicotte, A. Woessner, Q. Ma, Y. Lee, K. S. Myhro, C. N. Lau, P. Jarillo-Herrero, N. F. van Hulst, and F. H. L. Koppens. Generation of photovoltage in graphene on a femtosecond timescale through efficient carrier heating. *Nature Nanotechnology*, 10(5):437–443, may 2015.

[46] Justin C W Song, Michael Y. Reizer, and Leonid S. Levitov. Disorder-assisted electron-phonon scattering and cooling pathways in graphene. *Physical Review Letters*, 109(10):1–5, 2012.

[47] Matt W. Graham, Su-Fei Shi, Daniel C. Ralph, Jiwoong Park, and Paul L. McEuen. Photocurrent measurements of supercollision cooling in graphene. *Nature Physics*, 9(2):103–108, dec 2013.

[48] N. M. Gabor, J. C. W. Song, Q. Ma, N. L. Nair, T. Taychatanapat, K. Watanabe, T. Taniguchi, L. S. Levitov, and P. Jarillo-Herrero. Hot Carrier-Assisted Intrinsic Photoresponse in Graphene. *Science*, 334(6056):648–652, nov 2011.

[49] S.M. Sze and Kwok K. Ng. *Physics of Semiconductor Devices*, volume 16. John Wiley & Sons, Inc., Hoboken, NJ, USA, oct 2006.

[50] Thomas Mueller, Fengnian Xia, and Phaedon Avouris. Graphene photodetectors for high-speed optical communications. *Nature Photonics*, 4(5):297–301, mar 2010.

Experimental techniques

J. D. Mehew fabricated the graphene devices and contributed to the writing of the manuscript associated with this chapter.

3.1   Introduction

The growing interest in the fundamental science and applications of two-dimensional materials and their heterostructure has arisen largely due to the ease at which these systems can be prepared. Mechanical exfoliation of bulk crystals with adhesive tape and subsequent transfer to substrates has been crucial to the rapid prototyping of devices based on 2D materials. This simple process has been refined over the past decade to increase the yield and lateral size of exfoliated flakes.

3.2   Fabrication of 2D heterostructures

The thinning of bulk crystals can be achieved with a combination of tapes each with different properties. For example, high tack tape can readily cleave TMDs whilst water soluble tape is necessary for producing the clean, residue free interfaces. Appropriate preparation of the substrate is also necessary to facilitate the transfer of crystals from the tape. Typically, an O_2 plasma and heat treatment are used to enhance the adhesion between atomically thin crystals and the target substrate,[1] however care must be taken not to over-functionalize the surface such that the electronic properties of the crystal are adversely affected. This approach provides a reliable way to produce large area graphene and hBN on SiO_2. For TMDs it has been found that exfoliation onto PMMA (Poly-methyl methacrylate), PDMS

(Polydimethylsiloxane), or PPC (polypropylene carbonate) has a greater success rate than onto SiO_2.

Aside from increased flake yield, exfoliation onto polymers additionally allows the creation of heterostructures through layer by layer assembly of exfoliated crystals, known in this thesis as the 'dry transfer technique'.[2,3] Crystals are brought into close proximity to one another and adhere through van der Waals interactions. This lamination has an intrinsic self-cleaning mechanisms where contamination, typically hydrocarbons,[4] collects into bubbles leaving the rest of the interface contamination free.

In this thesis, PMMA has been used as the transfer scaffold because it leaves less residue than PDMS, is readily available (from use as resist in electron-beam lithography), and can be easily removed in acetone (unlike PPC which requires chloroform).[3]

3.2.1 Dry transfer technique

The dry transfer technique allows the layer by layer assembly of heterostructures. In this way complicated structures can be formed with atomically thin crystals. Figure 3.1 a shows the steps required to prepare a stack of atomically thin layers: A bulk crystal is thinned using electronic grade semiconductor tape. Thin flakes are mechanically transferred onto a polymer assembly (PMMA/PVA, 400/400 nm) at a temperature of $110\,°C$. After identifying the appropriate flakes (i.e. lateral size and thickness) under an optical microscope, a ring ($d \sim 5$ mm) is scored in the PMMA/PVA with sharp tweezers under a low magnification objective (x5). Using fined-tipped tweezers DI water can be dropped into the score dissolving the PVA. The hydrophobic nature of Si and PMMA draws the water to the centre of the scored ring, detaching the PMMA from the Si substrate. Immersing the Si/PVA/PMMA stack in DI H_2O allows the membrane to float on the surface of the liquid whilst the Si substrate is removed. Subsequently, the membrane is scooped out with the transfer arm, essentially a PMMA coated washer stuck to a metal plectrum, and baked on a hot plate for 10 minutes at $90\,°C$ to improve conformity between the two.

To align the membrane and target crystals two translation stages are used, one with the transfer arm capable of motion in the X, Y and Z directions as well as about the pitch and yaw axes, see Figure 3.1b, and the other with the target crystal capable of X', Y' and θ (rotational) motion. These stages are mounted under a long-working distance objective complete with a beam-splitter combining a CCD camera and fibre-coupled white light source. Both the illumination and detection lines are equipped with colour filters used to enhance the contrast of atomically thin materials.[5]

This technique can be used in two ways: to deposit a flake from PMMA to a
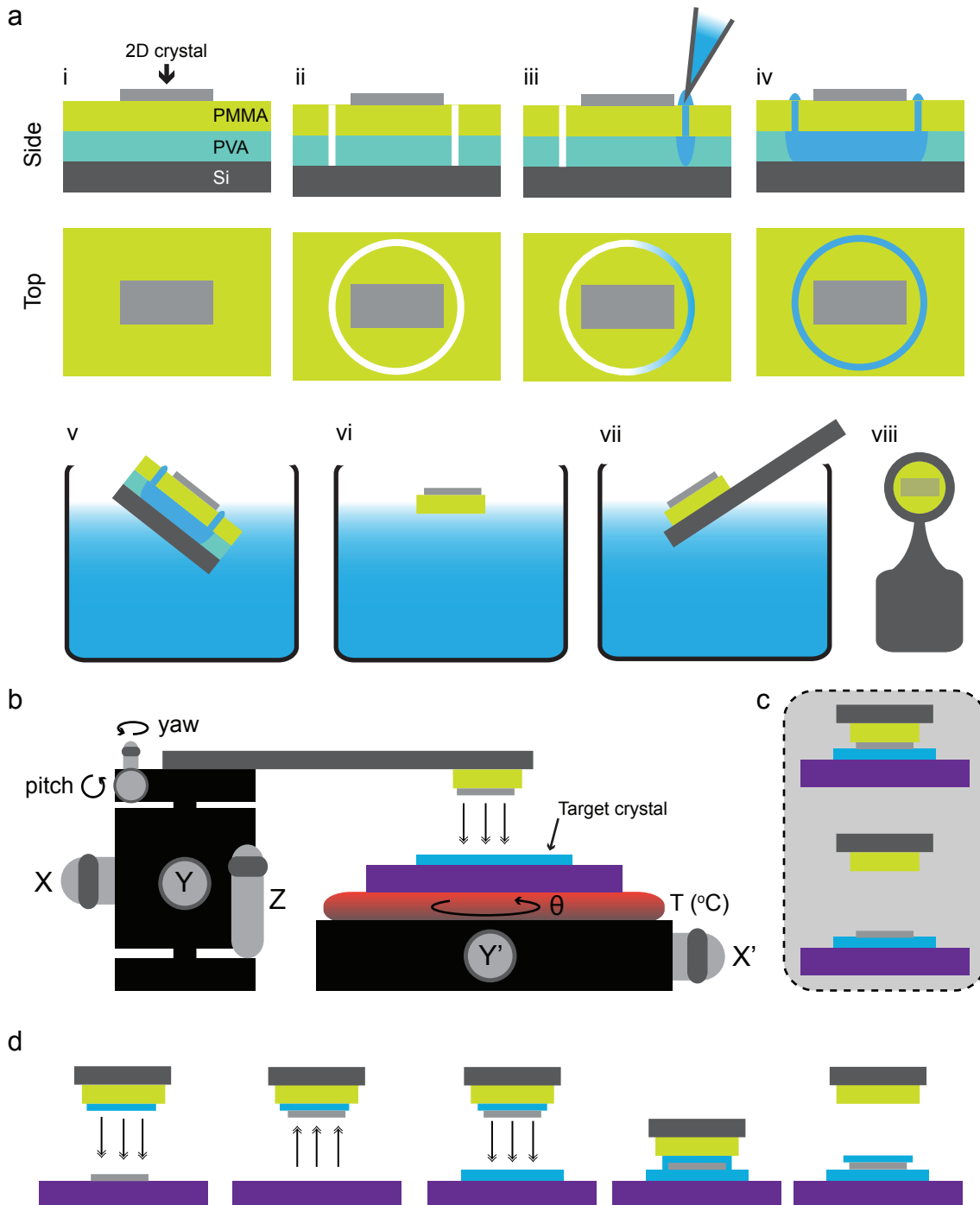
Figure 3.1: **Dry transfer technique** (a) Flake exfoliation and membrane preparation process, see main text for details. (b) Schematic of stacking set-up. The 2D crystal on membrane can be translated in the X, Y, Z, pitch and yaw axes to align with the target crystal. This is fixed on a temperature controlled rotational stage (X', Y', θ). The flake peel (c) and pick-up (d) ways of fabricating heterostructures.
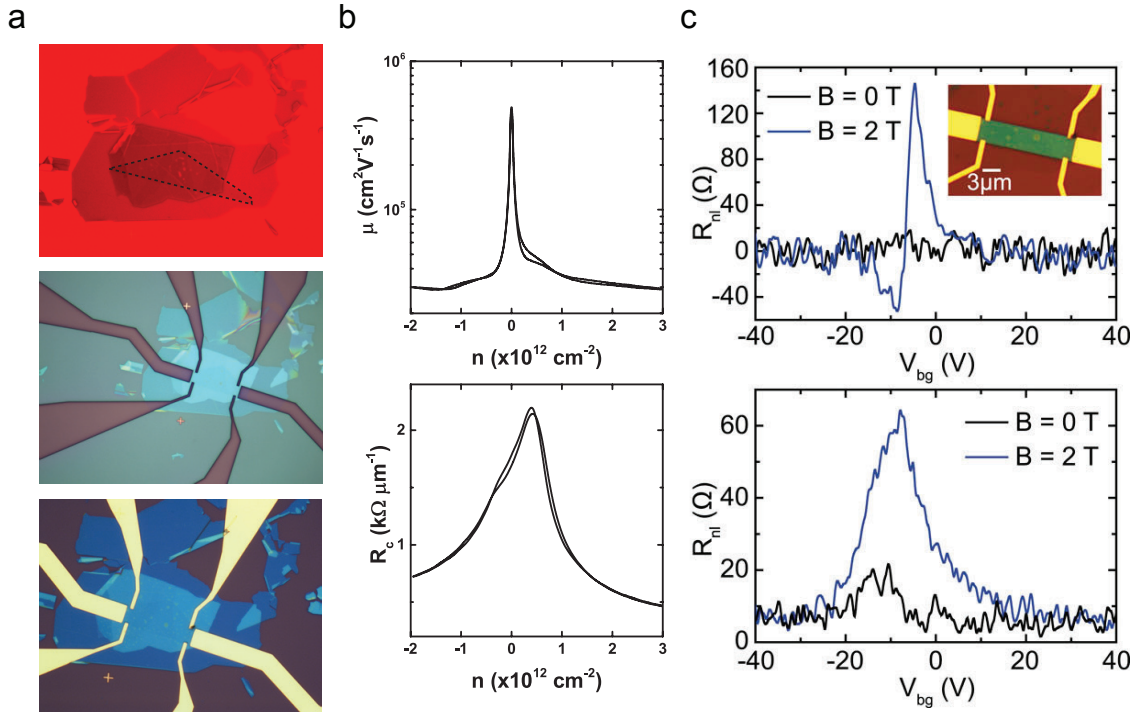
Figure 3.2: **Encapsulated graphene FET** (a) Optical images of fabrication process. From top to bottom: heterostructure under red illumination, contact design after plasma etch ($CHF_3:O_2$), device with Cr/Au (15/50 nm) leads. (b) Mobility (μ) and contact resistance (R_c) as a function of carrier density. (c) Non-local measurement in magnetic field with (lower) and without (upper) optocoupler circuit demonstrating the removal of spurious signals. Upper inset shows device after final etch. Reused under Creative Commons License (CC-BY 4.0).[6]

substrate (Figure 3.1c) or to pick up additional flakes onto the PMMA flake before the final transfer step (Figure 3.1d). The former case is used to transfer TMD flakes from PMMA to SiO_2/Si whilst the latter can be used to encapsulate flakes in hBN.

3.2.2 1D Contacts

The carrier mobility of graphene on SiO_2 is known to be limited by scattering from charged impurities, surface roughness and SiO_2 optical phonons.[7,8] On the other hand hBN is an atomically thin dielectric, lattice matched to within 1% of graphene, with minimal charge traps and high energy optical phonons. This makes it an ideal substrate for high mobility graphene devices, with mobilities approaching those of suspended devices.[8] Furthermore graphene can be encapsulated in hBN (hBN/SLG/hBN) isolating it from external sources of contamination. By plasma etching through the structure a single edge of graphene can be exposed due to the different etch rates of hBN and graphene. Unlike typical fabrication routes where the metal is deposited on top of graphene here the electrical connection is formed by a one-dimensional edge contact.[9] In this geometry the room temperature mobility of graphene reaches its maximal value limited by acoustic phonon scattering.[7,9]

Figure 3.2a illustrates the fabrication process for such a geometry. The hBN /SLG /hBN heterostructure was created using the dry transfer technique and electron-beam lithography was used to define the contact area before dry etching (CHF_3:O_2 plasma) and metallization (Cr/Au 15/50 nm). Finally the device was dry etched into a Hall bar geometry. The mobility was extracted using the Drude model from an AC lock-in measurement of the conductivity whilst the carrier density was modulated using the hBN/SiO_2/Si^{++} gate, Figure 3.2b. At carrier densities relevant for most applications ($n \geq 1 \times 10^{12}$ cm^{-2}) the mobility exceeds $\mu = 40,000$ cm^2 V^{-1} s^{-1} and the contact resistance R_c is less than $500\,\Omega\,\mu$m^{-1}. This high quality heterostructure was used to test a novel circuit built for high impedance and non-local measurements, Figure 3.2c.[6]

3.3   Raman spectroscopy

Raman spectroscopy is an optical technique in which light is used to probe the properties of a material. Over the last 80 years the vibrational and rotational modes of molecules have been catalogued providing the scientific community with a non-destructive detection and identification technique. Similarly, in solid state physics the fingerprints of collective oscillations of atoms, i.e. phonons, have been used to characterise materials.

In this technique an absorbed photon will excite an electron from an occupied state, such as in the valence band to an unoccupied state, which could be a sub-gap virtual state or a real state above the conduction band. Upon relaxation a photon of a different energy is emitted due to inelastic scattering. The system is now in a different vibrational state either higher (Stokes) or lower (anti-Stokes) in energy than the initial state. The Raman shift ($\Delta\omega$) is the difference in energies between these states and can be expressed as

$$\Delta\omega = \left(\frac{1}{\lambda_0} - \frac{1}{\lambda_1}\right). \tag{3.1}$$

Normally the Raman shift is reported in units of reciprocal centimetres $\Delta\omega$[cm^{-1}] and so we can modify Equation 3.1 to:

$$\Delta\omega[\text{cm}^{-1}] = \left(\frac{1}{\lambda_0[\text{nm}]} - \frac{1}{\lambda_1[\text{nm}]}\right)\frac{10^7[\text{nm}]}{\text{cm}}. \tag{3.2}$$

In the following sections the theoretical explanation for this shift will be presented from both a classical and quantum viewpoint.
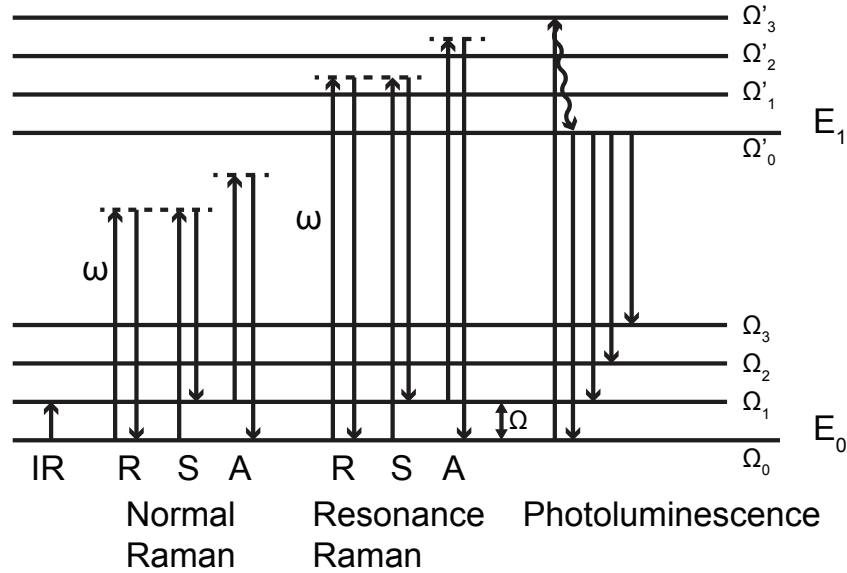
Figure 3.3: Energy level diagram for infra-red (IR), normal and resonance Raman, and photoluminescence spectroscopy. The Raman transitions include Rayleigh (R), Stokes (S) and anti-Stokes (A) processes. E_n and Ω_n are the electronic and vibrational energy levels respectively whilst ω (Ω) is the photon (phonon) frequency.

3.3.1 Classical theory of Raman spectroscopy

In the classical theory of Raman spectroscopy the system is treated as a diatomic molecule which has various vibrational and rotational degrees of freedom. Upon excitation a dipole is formed which interacts with these vibrational or rotation states. Therefore, in a solid crystal we can use the same argument as a diatomic molecule, with added simplicity from the absence of rotational states.

If a molecule is irradiated by an oscillating electromagnetic field of the form $\vec{E} = E_0 \cos(\omega t)$, e.g. by means of a laser beam, an electric dipole moment $\vec{P}$ will be induced:[10]

$$\vec{P} = \hat{\boldsymbol{\alpha}} \vec{E} \tag{3.3}$$

where $\hat{\boldsymbol{\alpha}}$ is the polarisability tensor of the molecule. If the molecule is vibrating at a frequency Ω the vibration coordinate $\vec{Q}$ can be expressed as:

$$\vec{Q} = \vec{Q_0} \cos(\Omega t). \tag{3.4}$$

The polarisability can be expressed as a function of Q which in the harmonic (1st order) approximation becomes:

$$\hat{\boldsymbol{\alpha}} = \hat{\boldsymbol{\alpha}}_0 + \left(\frac{\partial \hat{\boldsymbol{\alpha}}}{\partial \vec{Q}} \right) \vec{Q}. \tag{3.5}$$

Combining equation 3.3 with equations 3.4 and 3.5 and making use of trigonometric

identities the following expression is obtained:

$$
\begin{aligned}
\vec{P} \; = \;& \hat{\boldsymbol{\alpha}}_0 \vec{E}_0 \cos(\omega t) \\
&+ \frac{1}{2} \left(\frac{\partial \hat{\boldsymbol{\alpha}}}{\partial \vec{Q}} \right) \vec{Q}_0 \vec{E}_0 \cos \left\{ (\omega - \Omega) t \right\} \\
&+ \frac{1}{2} \left(\frac{\partial \hat{\boldsymbol{\alpha}}}{\partial \vec{Q}} \right) \vec{Q}_0 \vec{E}_0 \cos \left\{ (\omega + \Omega) t \right\}
\end{aligned}
\tag{3.6}
$$

Equation 3.6 has three distinct parts to it; the first is Rayleigh scattering where an oscillating dipole radiates light at a frequency ω, whilst the second and third terms describe the inelastic (Raman) scattering at a frequency of $\omega - \Omega$ (Stokes) and $\omega + \Omega$ (Anti-Stokes), which can be seen schematically in Figure 3.3. Clearly, the light can only be scattered by a phonon mode if $\left(\partial \hat{\boldsymbol{\alpha}} / \partial \vec{Q} \right)_0$ is non-zero. The modes which will be active can be determined through group theory, optical selection rules, and symmetry rules.[10]

3.3.2   Quantum theory of Raman spectroscopy

In the quantum description of the Raman process the oscillating dipole approach is neglected in favour of one involving the quantum transition of an electron from an initial to final state upon interaction with the electromagnetic (EM) field. This transition probability per unit time (W_m) is calculated in the time-dependent perturbation framework using Fermi's golden rule:

$$
W_m \cong \frac{2\pi}{\hbar} \mid \mathcal{H}_{ml} \mid^2 \rho(E_m),
\tag{3.7}
$$

where $\mathcal{H}$ is the perturbed Hamiltonian and $\rho(E_m)$ the joint density of states. The Born-Oppenheimer approximation has been applied to the Hamiltonian describing the system. In this way the eigenfunctions of the electronic and vibrational states are separated. For this system, energy and crystal momentum must be conserved which requires:

$$
\begin{aligned}
\hbar \omega_s &= \hbar \omega_i \pm \hbar \Omega, \\
\hbar k_s &= \hbar k_i \pm \hbar Q,
\end{aligned}
\tag{3.8}
$$

where ω_i (ω_s) is the incident (Raman) photon frequency, Ω the phonon frequency, k_i (k_s) the incident (Raman) photon wavevector and Q the phonon wavevector.

A notable difference between the classical and quantum theories is the explanation of the intensity of the Stokes and anti-Stokes emissions. Given the quantisation of phonon energies, low energy states are more likely to be occupied than higher energy states with the phonon population described by the Bose-Einstein distribution. As the Stokes (anti-Stokes) process creates (annihilates) a phonon the intensity

Figure 3.4: **Phonon dispersion in graphene** The modes with in-plane (i) longitudinal (L) and transverse (T) motions are much stronger than those out-of-plane (o). Adapted with permission.[15]

ratio arising from these processes is determined by normalization factors:[10]

$$\frac{I_{as}}{I_S} = Ce^{E_q/k_B T},\tag{3.9}$$

where C is a constant that accounts for the optical properties of the system. Rearranging Equation 3.9 the phonon temperature can be determined:

$$T = \frac{1}{k_B\left[\ln C - \ln\left(\frac{I_{aS}}{I_S}\right)\right]},\tag{3.10}$$

This is not necessarily valid for high-energy phonons as the anti-Stokes scattering may be dominated by a phenomenon known as Stokes-anti-Stokes (SAS) scattering.[11]

3.3.3 Raman spectrum of Graphene

Raman spectroscopy has become ubiquitous in the study of graphene. Building upon almost 50 years of research into the Raman spectrum of graphite, this powerful tool can be used to determine the characteristics of phonons in graphene and reveal information about the crystal including the presence of defects,[12] degree of doping[13] and number of layers.[14]

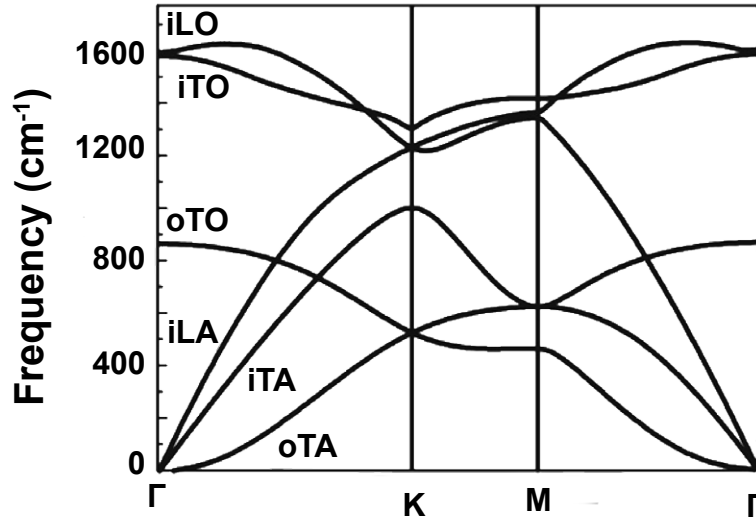Graphene has 6 phonon branches: 3 acoustic (A) and 3 optical (O), Figure 3.4. The modes with in-plane (i) longitudinal (L) and transverse (T) motions are much stronger than those out-of-plane (o). The 2 atoms in the unit cell of graphene result in six normal modes at the Brillouin zone centre (Γ): A_{2u}, B_{2g}, E_{1u}, E_{2g}. Both the out-of-plane B_{2g} and in-plane E_{2g} modes are doubly degenerate with the latter mode
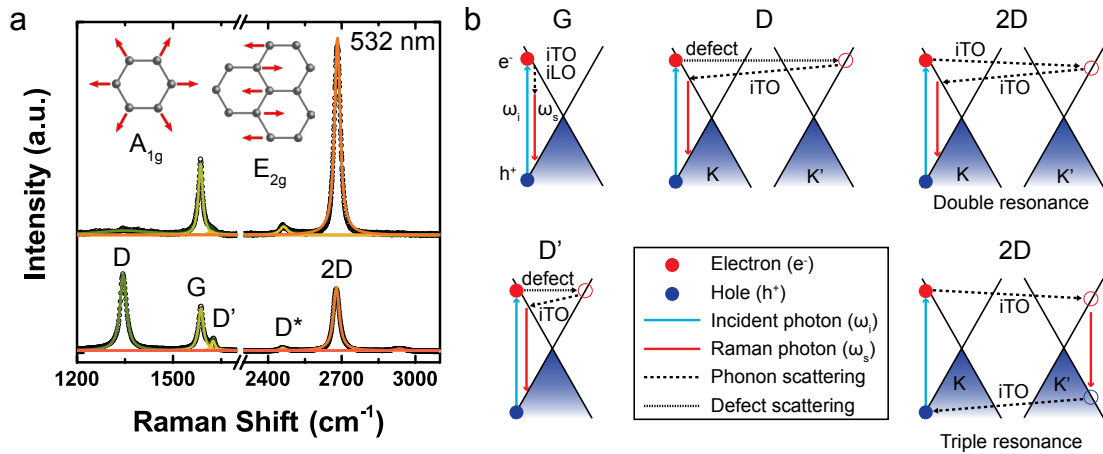
Figure 3.5: **Raman spectra and phonon processes in graphene** (a) Raman spectra of pristine (upper) and defective (lower) graphene. Measured data black spheres, Lorentzian fit coloured lines. Inset show atomic modes of A_{1g} and E_{2g}. (b) Main phonon processes in SLG. Incident (scattered) photon shown in blue (red). Scattering from phonons (defects) are shown with dashed (dotted) lines. Electrons and holes are represented by red and blue spheres respectively.

Raman active.[16]

   Raman spectra of monolayer graphene are shown in Figure 3.5a. The phonon displacement pattern for the Raman active A_{1g} (K) and E_{2g} (Γ) modes are also shown. In Figure 3.5a, a number of distinct peaks are observed, each fit with a Lorentzian profile. The G peak comes from the iTO and iLO phonon modes located at the Γ point whilst the D peak comes from iTO phonons around K, see Figure 3.5b. Breathing modes of the six atom ring are responsible for the D peak which only appears in the presence of defects shown by the dotted lines. The D' is the intra-valley equivalent of the inter-valley D peak and again is defect activated. The lower spectrum in Figure 3.5a comes from a fluorinated graphene monolayer. In this material fluorine atoms are covalently bonded to the out-of-plane electronic orbitals of the carbon atoms in graphene. Contrasted with the upper pristine spectrum the D and D' peaks are now observed due to this disruption to the pristine crystal. The 2D peak is the D peak overtone however no defect is required for activation due to the dual phonon process providing conservation of momentum.

   A single Lorentzian can be used to fit the 2D peak of single-layer graphene (SLG) however for bilayer graphene (BLG) multiple Lorentzians are required, Figure 3.6a. Due to the interlayer interaction both the conduction and valence bands split in two but of the four bands only two are coupled to the incident light. Furthermore two TO phonons can couple to all four bands resulting in four processes contributing to the four peaks that form the 2D peak in BLG Figure 3.6b.[16]
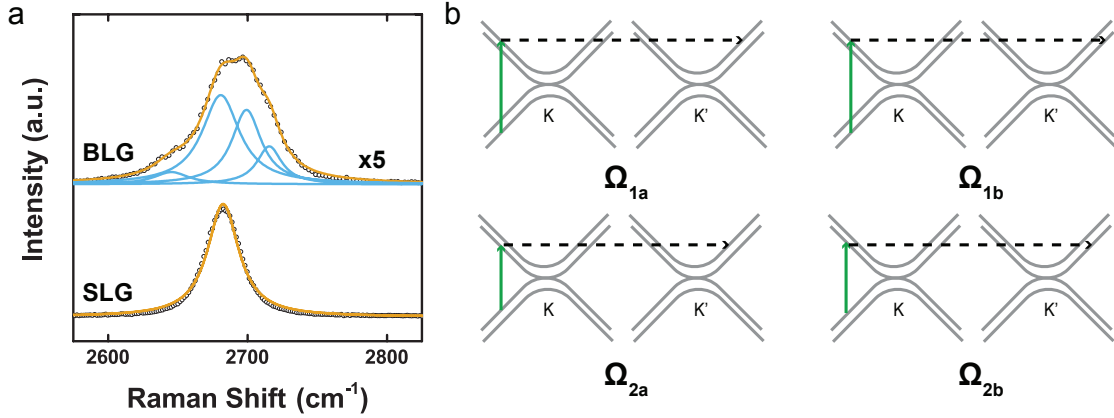
Figure 3.6: **Bilayer graphene Raman** (a) 2D peak of single-layer graphene (SLG), bottom, and bilayer graphene (BLG), top. (b) Phonon processes contributing to the 2D peak in BLG.

Influence of doping and strain on the Raman spectrum of graphene

The 2D nature of graphene means that (i) the number of charge carriers can be modulated over several orders of magnitude in FET geometry and (ii) high levels of mechanical strain can be induced. The latter will clearly modify the phonon frequencies due to changes in lattice constants whilst the former induces changes due to non-adiabatic electron-phonon coupling and chemical bond modification.[17]

Often doping and strain are induced at the same time for example as a consequence of fabrication or annealing processes and separation of the two typically requires the independent characterisation through complementary techniques such as electrical measurements. In the work of Ji Eun Lee and colleagues,[18] a method for the decomposition of strain and doping contributions to the changes in the Raman peak positions was presented.

Figure 3.7 show spatially resolved maps of the G peak position for graphene on SiO_2 before (a) and after (b) annealing at $400\,°C$ which results in an up shift of the average G peak position by 25 cm^{-1}. The 2D peak is also shifted after the anneal without the emergence of the D peak, Figure 3.7c. Interestingly, a correlation between the peak positions is revealed by plotting the G and 2D frequencies measured at each spatial location, Figure 3.7d.

A strain and doping free reference point (**O**) was acquired from free-standing graphene from which the predicted behaviour under random uni-axial strain is plotted, dashed black line Figure 3.7d. The data from as-exfoliated samples agree well with this and indicate that graphene on SiO_2 is subject to tensile strain. Influence of hole doping is shown by the dashed magenta line. Upon annealing the data points now reveal an increase in hole doping as well as a change from tensile to compressive strain. This can be understood in a simple vector model:[18] For any set of ω_{2D}, ω_G, the vector **OP** can be decomposed into the strain/doping free direction **OH/OT** with unit vectors e_H/e_T (tensile) and $-e_T$ for compressive strain. These
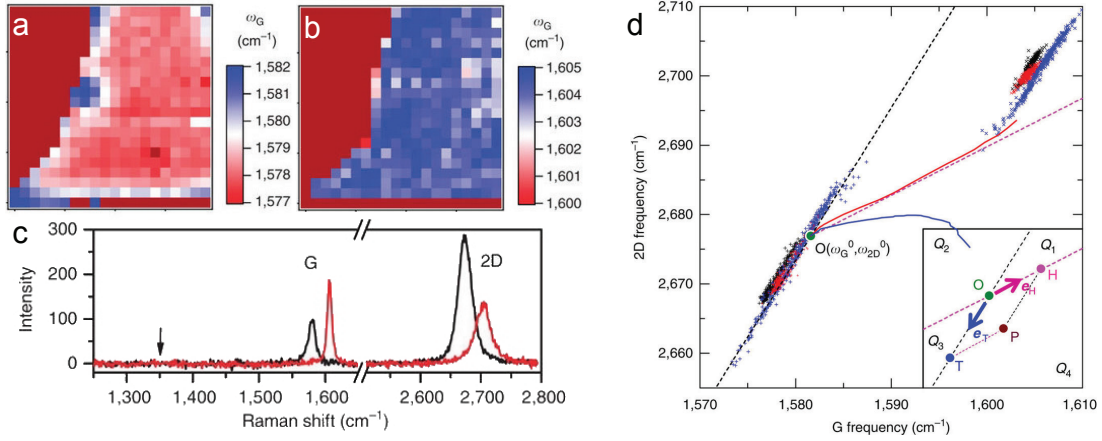
Figure 3.7: Spatial Raman maps of G peak position for pristine (a) and annealed (b) samples. (c) Comparison of full spectrum for pristine (black) and annealed (red). (d) Correlation between G and 2D peak positions for pristine (+) and annealed (x) samples. Inset shows vector decomposition of doping and strain. Reused with permission.[18]

unit vectors are known from previous works to be:

$$\mathbf{e_T} = (\Delta\omega_{2D}/\Delta\omega_G)\,\epsilon^{\text{uniaxial}} = 2.2 \pm 0.2,$$
$$\mathbf{e_H} = (\Delta\omega_{2D}/\Delta\omega_G)\,n^{\text{hole}} = 0.70 \pm 0.05. \tag{3.11}$$

This allows for the measurement of strain in graphene devices providing that the change in doping, if any, arises due to holes. Analysis with electron doped samples becomes more complicated due to increased non-linearity at high carrier concentrations.

3.3.4   Raman spectrum of TMDs

The atomic structure of transition metal dichalcognides (TMDs) has greater complexity than graphene due to the M-X-M (metal, chalcogen, metal) arrangement. As such these system exhibit a rich variety in lattice dynamics with a layer dependence of the symmetry, force constants and peak frequency.[19]

Bulk MX_2 has six atoms in the unit cell which gives 3 acoustic (A) and $3N-3 = 15$ optical (O) phonon modes. From the D_{6h} point group symmetry of MX_2 the lattice vibrations at the Γ point can be expressed as:[20]

$$\Gamma = A_{1g} + 2A_{2u} + 2B_{2g} + B_{1u} + E_{1g} + 2E_{1u} + 2E_{2g} + E_{2u}, \tag{3.12}$$

where one of the A_{2u} and E_{1u} modes is acoustic whilst the other is IR active. Both B_{2g} modes are inactive, as are the B_{1u} and E_{2u} modes. The Raman active modes are A_{1g}, E_{1g} and both E_{2g}. Figure 3.8 shows a schematic of the atomic motions associated with these modes (a) and the correspond Raman peaks for few-layer
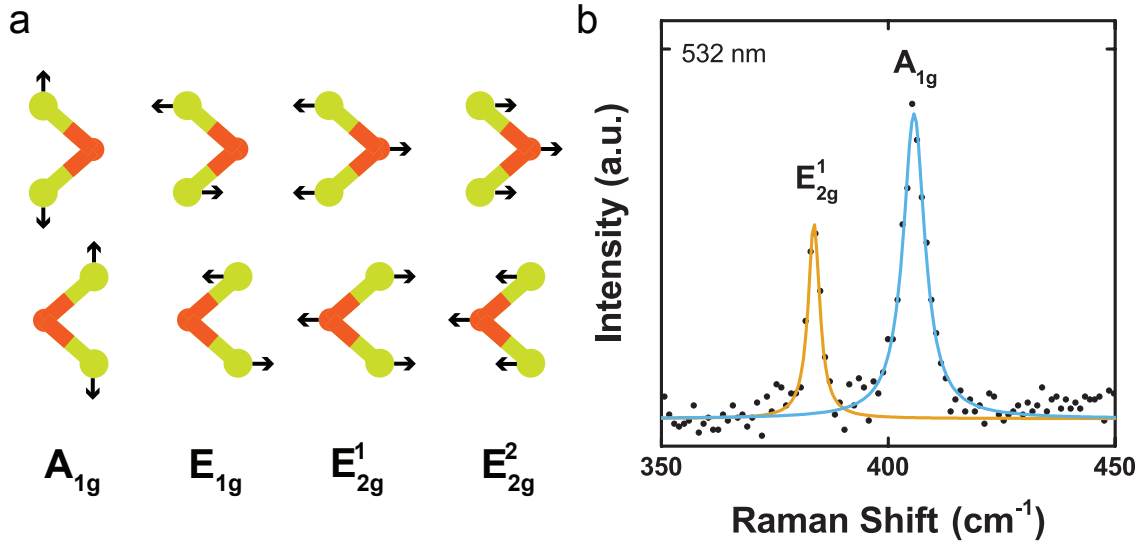
Figure 3.8: **Bulk MX$_2$ Raman active modes** (a) From left to right: A$_{1g}$, E$_{1g}$, E$_{2g}^1$ and E$_{2g}^2$ modes. (b) Raman spectra of few-layer MoS$_2$.

MoS$_2$ (b). The lack of translational symmetry in few-layer TMDs means that even and odd numbers of layers possess different modes due to their symmetry.

3.4 Optoelectronic characterisation

To characterise the properties of the optoelectronic devices presented in this thesis a number of techniques have been employed. Central to the majority of these is the hybridisation of an upright microscope (Olympus BX-50) with automated x-y-z stage (Prior Scientific) and spectrometer (Princeton Instruments SP2500). White light illumination is provided by an LED whilst a multichannel laser bank provides coherent light from UV to NIR ($\lambda = 375, 473, 514, 561, 685$ nm), see Figure 3.9a. Simultaneous electrical measurements are possible with use of an integrated PCB and BNC breakout box. A custom-developed vacuum chamber compatible with the existing stage/microscope assembly allows the characterisation of materials and devices in vacuum and/or under controlled atmosphere (Figure 3.9b,c).

3.4.1 Scanning Photocurrent Mapping

Scanning Photocurrent Microscopy (SPCM) allows the spatial mapping of the photocurrent signal. A laser beam is focussed onto the sample and the resultant photocurrent recorded as a function of position. The diffraction limited spot size and 10 nm resolution of the stage allows the local photoconductivity to be mapped out with sub-micrometer precision.
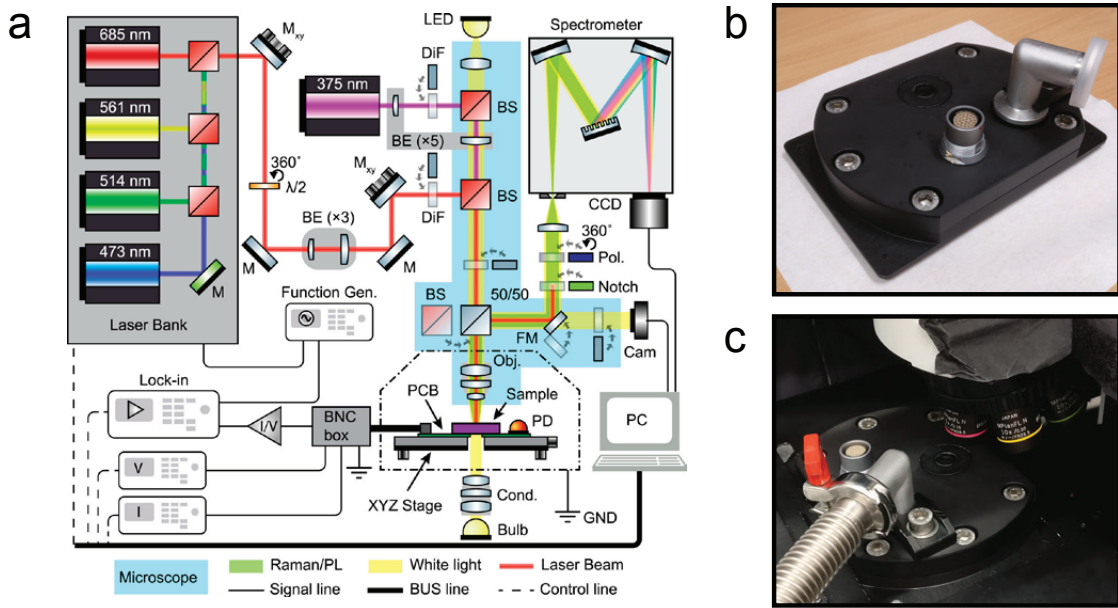
Figure 3.9: **Integrated microscope set-up** (a) Schematic of integrated microscope capable of scanning photocurrent mapping, Raman, photoluminescence (PL) and reflection/transmission measurements. Light sources include lasers, LEDs and bulbs. Simultaneous electrical measurements are possible due to integration of PCB circuitry into light-tight enclosure (dot-dashed line). Abbreviations: mirror (M), kinematic mirror (M_{xy}), half-wavelength plate ($\lambda/2$), beam expander (BE, followed by magnification), drop-in filter (DiF), beam splitter (BS, dichroic in red), Polariser/Analyser (Pol.), white light (WL), voltage (V) or current (I) sources/meters, flip mirror (FM), sample holder (PCB), photodetector (PD), condenser (Cond), microscope objective (Obj), imaging camera (Cam), spectroscopy camera (CCD), ground line (GND). Reused under Creative Commons License (CC-BY 4.0).[21] (b) Photo of vacuum chamber ($P_{min} \leq 10^5$ mbar) developed by Gareth F. Jones with assistance from the author for characterising air sensitive materials. (c) Placement under microscope assembly.

3.4.2   Luminescence

Luminescence spectroscopy probes the radiative recombination of materials either under optical (*photo-luminescence*) or electrical (*electro-luminescence*) excitation. Due to the direct band gap and large exciton binding energy of monolayer TMDs strong light emission can be observed even at room temperature. As such these materials are promising for light-emitting applications.

3.4.3   External Quantum Efficiency

A separate set-up was used to characterise the external quantum efficiency, spectral responsivity, and transient response of various photodetectors. These measurements were performed in a custom built vacuum chamber (10^{-3} mbar) using a xenon lamp, monochromator, and collimating optics (Oriel TLS-300X), to provide a spectrally tunable incident light source. Neutral density (ND) filters and a motorized chopper
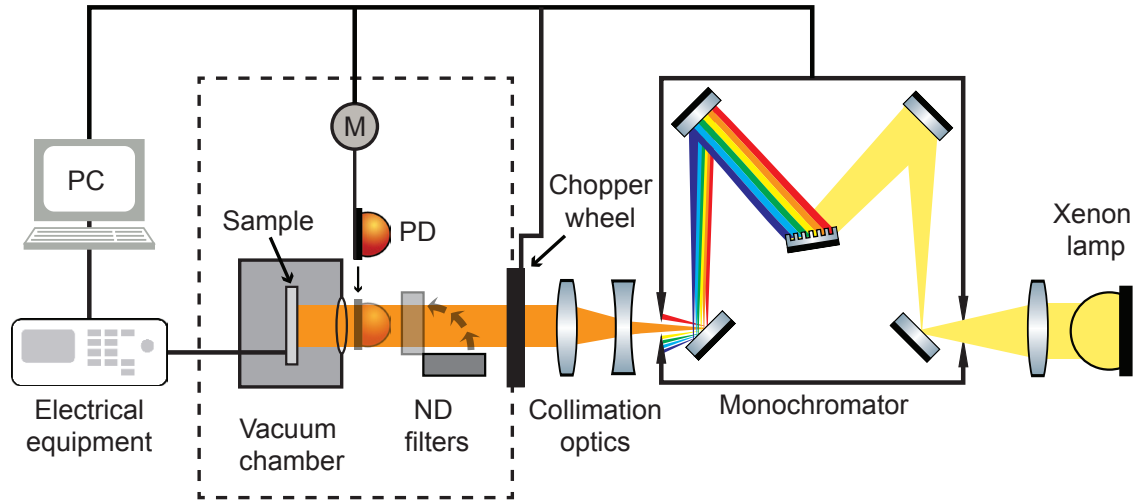
Figure 3.10: **Schematic of EQE set-up** Xenon lamp and monochromator provide spectrally tunable light source whilst a chopper wheel and neutral density (ND) filters modulate and attenuate the signal. A photodiode (PD) is mounted on a linear actuator (M). The sample is placed in a vacuum chamber ($P_{\min} \leq 10^{-6}$ mbar) capable of *in-situ* annealing and housed inside a light-tight enclosure (dashed lines). A vacuum feedthrough connects the sample to the electrical measurement equipment. The equipment is automated by using a PC to control and read data from the monochromator, chopper wheel, photodiode and equipment.

wheel are used to attenuate and modulate the incident signal, respectively. Power calibrations were initially performed with a ThorLabs PM320E power meter equipped with a S130VC sensor and monitored in between measurements by a Thorlabs FDS1010 photodiode mounted on a linear actuator, see Figure 3.10.

References

[1] Yuan Huang, Eli Sutter, Norman N. Shi, Jiabao Zheng, Tianzhong Yang, Dirk Englund, Hong-Jun Gao, and Peter Sutter. Reliable Exfoliation of Large-Area High-Quality Flakes of Graphene and Other Two-Dimensional Materials. *ACS Nano*, 9(11):10612–10620, nov 2015.

[2] Andres Castellanos-Gomez, Michele Buscema, Rianda Molenaar, Vibhor Singh, Laurens Janssen, Herre S.J. Van Der Zant, and Gary A. Steele. Deterministic transfer of two-dimensional materials by all-dry viscoelastic stamping. *2D Materials*, 1(1), 2014.

[3] Filippo Pizzocchero, Lene Gammelgaard, Bjarke S. Jessen, José M. Caridad, Lei Wang, James Hone, Peter Bøggild, and Timothy J. Booth. The hot pick-up technique for batch assembly of van der Waals heterostructures. *Nature Communications*, 7(May):11894, jun 2016.

[4] S. J. Haigh, A. Gholinia, R. Jalil, S. Romani, L. Britnell, D. C. Elias, K. S. Novoselov, L. A. Ponomarenko, A. K. Geim, and R. Gorbachev. Cross-sectional imaging of individual layers and buried interfaces of graphene-based heterostructures and superlattices. *Nature Materials*, 11(9):764–767, sep 2012.

[5] P. Blake, E. W. Hill, A. H. Castro Neto, K. S. Novoselov, D. Jiang, R. Yang, T. J. Booth, and A. K. Geim. Making graphene visible. *Applied Physics Letters*, 91(6):063124, aug 2007.

[6] Adolfo De Sanctis, Jake D. Mehew, Saad Alkhalifa, Callum P. Tate, Ashley White, Adam R. Woodgate, Monica F. Craciun, and Saverio Russo. Novel circuit design for high-impedance and non-local electrical measurements of two-dimensional materials. *Review of Scientific Instruments*, 89(2):024705, feb 2018.

[7] Jian-Hao Chen, Chaun Jang, Shudong Xiao, Masa Ishigami, and Michael S. Fuhrer. Intrinsic and extrinsic performance limits of graphene devices on SiO2. *Nature Nanotechnology*, 3(4):206–209, apr 2008.

[8] C R Dean, a F Young, I Meric, C Lee, L Wang, S Sorgenfrei, K Watanabe, T Taniguchi, P Kim, K L Shepard, and J Hone. Boron nitride substrates for high-quality graphene electronics. *Nature nanotechnology*, 5(10):722–726, oct 2010.

[9] L. Wang, I. Meric, Pinshane Y. Huang, Q. Gao, Y. Gao, H. Tran, T. Taniguchi, K. Watanabe, L. M. Campos, David A. Muller, J. Guo, P. Kim, James Hone, K. L. Shepard, and Cory R. Dean. One-Dimensional Electrical Contact to a Two-Dimensional Material. *Science*, 342(6158):614–617, nov 2013.

[10] D. A. Long. *Introductory Raman Spectroscopy. John R. Ferraro, Kazuo Nakamoto and Chris W. Brown. Academic Press, Amsterdam, Second Edition, 2003. xiii + 434*, volume 36. Academic Press, 2005.

[11] Ado Jorio, Mark Kasperczyk, Nick Clark, Elke Neu, Patrick Maletinsky, Aravind Vijayaraghavan, and Lukas Novotny. Optical-Phonon Resonances with Saddle-Point Excitons in Twisted-Bilayer Graphene. *Nano Letters*, 14(10):5687–5692, oct 2014.

[12] M.A. Pimenta, G. Dresselhaus, M.S. Dresselhaus, L.G. Cançado, Ado Jorio, and R. Saito. Studying disorder in graphite-based systems by Raman spectroscopy. *Physical Chemistry Chemical Physics*, 9(11):1276–1291, mar 2007.

[13] A Das, S Pisana, B Chakraborty, S Piscanec, S K Saha, U V Waghmare, K S Novoselov, H R Krishnamurthy, A K Geim, A C Ferrari, and A K Sood. Monitoring dopants by Raman scattering in an electrochemically top-gated graphene transistor. *Nature Nanotechnology*, 3(4):210–215, apr 2008.

[14] A. C. Ferrari, J. C. Meyer, V. Scardaci, C. Casiraghi, M. Lazzeri, F. Mauri, S. Piscanec, D. Jiang, K. S. Novoselov, S. Roth, and A. K. Geim. Raman spectrum of graphene and graphene layers. *Physical Review Letters*, 97(18):187401, oct 2006.

[15] L. M. Malard, M. A. Pimenta, G. Dresselhaus, and M. S. Dresselhaus. Raman spectroscopy in graphene. *Physics Reports*, 473(5-6):51–87, apr 2009.

[16] Andrea C. Ferrari and Denis M. Basko. Raman spectroscopy as a versatile tool for studying the properties of graphene. *Nature Nanotechnology*, 8(4):235–246, apr 2013.

[17] Michele Lazzeri and Francesco Mauri. Nonadiabatic Kohn Anomaly in a Doped Graphene Monolayer. *Physical Review Letters*, 97(26):266407, dec 2006.

[18] Ji Eun Lee, Gwanghyun Ahn, Jihye Shim, Young Sik Lee, and Sunmin Ryu. Optical separation of mechanical strain from charge doping in graphene. *Nature Communications*, 3(May):1024, 2012.

[19] Xin Zhang, Xiao-Fen Qiao, Wei Shi, Jiang-Bin Wu, De-Sheng Jiang, and Ping-Heng Tan. Phonon and Raman scattering of two-dimensional transition metal dichalcogenides from monolayer, multilayer to bulk material. *Chemical Society Reviews*, 44:2757–2785, 2015.

[20] J. L. Verble and T. J. Wieting. Lattice mode degeneracy in MoS2 and other layer compounds. *Physical Review Letters*, 25(6):362–365, 1970.

[21] Adolfo De Sanctis, Gareth F. Jones, Nicola J. Townsend, Monica F. Craciun, and Saverio Russo. An integrated and multi-purpose microscope for the characterization of atomically thin optoelectronic devices. *Review of Scientific Instruments*, 88(5):055102, may 2017.

4

Hybridised graphene photodetectors

4.1 Introduction

The use of two-dimensional (2D) materials in optoelectronic devices has the potential to supersede current state-of-the-art technology[1] by added functionalities, such as mechanical flexibility and ease of integration onto textile fibres, enabling the development of new wearable electronic applications.[2] Graphene transistors have been shown to operate as high-speed photodetectors[3] with response times comparable to conventional silicon-based devices, but the absence of a band gap and lack of significant gain mechanism limits its use for ultra-sensitive light detection. Hybrid structures of graphene with semiconductor materials such as quantum dots,[4–6] chlorophyll molecules,[7] and MoS$_2$[8–10] have been shown to enhance light absorption and provide an internal gain mechanism. However, these implementations typically have a limited operational bandwidth of less than 10 Hz which hampers their use in real world applications.

Slow response times in these systems are produced by the long-lived trapping of charges, often manifested as hysteresis in gate voltage sweeps. This has been observed in organic, carbon nanotubes, graphene, and more recently in transition metal dichalcogenide (TMD) field-effect transistors, and is typically attributed to unavoidable intrinsic and/or extrinsic charge traps, e.g. SiO$_2$ surface states[11–14] and atmospheric contamination.[12,13,15–17] To reduce the impact of such traps, various solutions have been explored including gate voltage pulses,[11,18,19] vacuum annealing,[20,21] and ionic liquid gating.[22,23] Although ionic liquid gating has been utilised

in WS_2 phototransistors[24] and $MoTe_2$-graphene photodetectors[25], the beneficial effect of polymer gating on the performance of photodetectors consisting of atomically thin heterostructures has not yet been explored.

In this chapter, WS_2-graphene heterostructure photodetectors with an ionic polymer gate are investigated. A gate tunable responsivity up to 10^6 A W^{-1} is demonstrated, which is comparable with other heterostructure devices,[4–7,9,10] and surpasses that of graphene or TMD photodetectors by at least 4 orders of magnitude. These devices reach a -3 dB bandwidth of 1.5 kHz, without the need for any gate pulse, leading to sub-millisecond rise and fall times. The observed 10^3 fold increase of photodetection bandwidth, when compared to other heterostructure photodetectors, is enabled by the enhanced screening properties of mobile ions in the ionic polymer top gate, which act to compensate the charge traps limiting the speed of previous devices. These devices have a detectivity $D^* = 3.8 \times 10^{11}$ Jones, which is approaching that of single photon counters, and are able to operate on a broad spectral range (400 - 700 nm). These properties make ionic polymer gated WS_2-graphene photodetectors highly suitable for video-frame-rate imaging applications unlike previously developed graphene-based heterostructure photodetectors.[4,5,7–10]

4.2 Sample Preparation

Hybrid WS_2-graphene photodetectors have been fabricated on p-Si/SiO_2 (290 nm) substrates, where the doped Si serves as a global back gate. Few-layer WS_2 was mechanically exfoliated from bulk crystals and transferred onto the SiO_2 substrate by means of adhesive tape. WS_2 flakes with thickness between 2 nm and $\sim$50 nm were selected for further fabrication.

The growth of graphene by chemical vapour deposition was carried out in a cold-wall furnace (Moorfield nanoCVD-8G) using a low-pressure CVD process following an optimized growth process.[26] Copper foils (Alpha Aesar, 99% purity, 0.025 mm thick) were used as substrate. The furnace was pumped down to 0.1 mTorr and then heated up to $1000\,°C$ at a rate of $10\,°C\,s^{-1}$, in the presence of Ar and H_2. These conditions were maintained for 10 minutes to increase the copper grain size. Subsequently, the Ar flow was suppressed and CH_4 introduced into the chamber, to initiate the growth of graphene. The pressure was kept at 18 mTorr for 10 minutes during this growth stage. In the last processing step, Ar was introduced into the chamber, after ceasing both the CH_4 and H_2 flows, whilst cooling at a rate of $10\,°C\,s^{-1}$. High quality graphene grown by chemical vapour deposition was then transferred onto the WS_2 using a common PMMA-assisted wet transfer technique.[26]

Electrical contacts were defined by standard electron beam lithography, electron beam deposition of Au (20 nm) and lift-off in acetone. Subsequently, conductive graphene channels of widths ranging from 3 to $10\,\mu m$ and lengths 1 to $12\,\mu m$ were
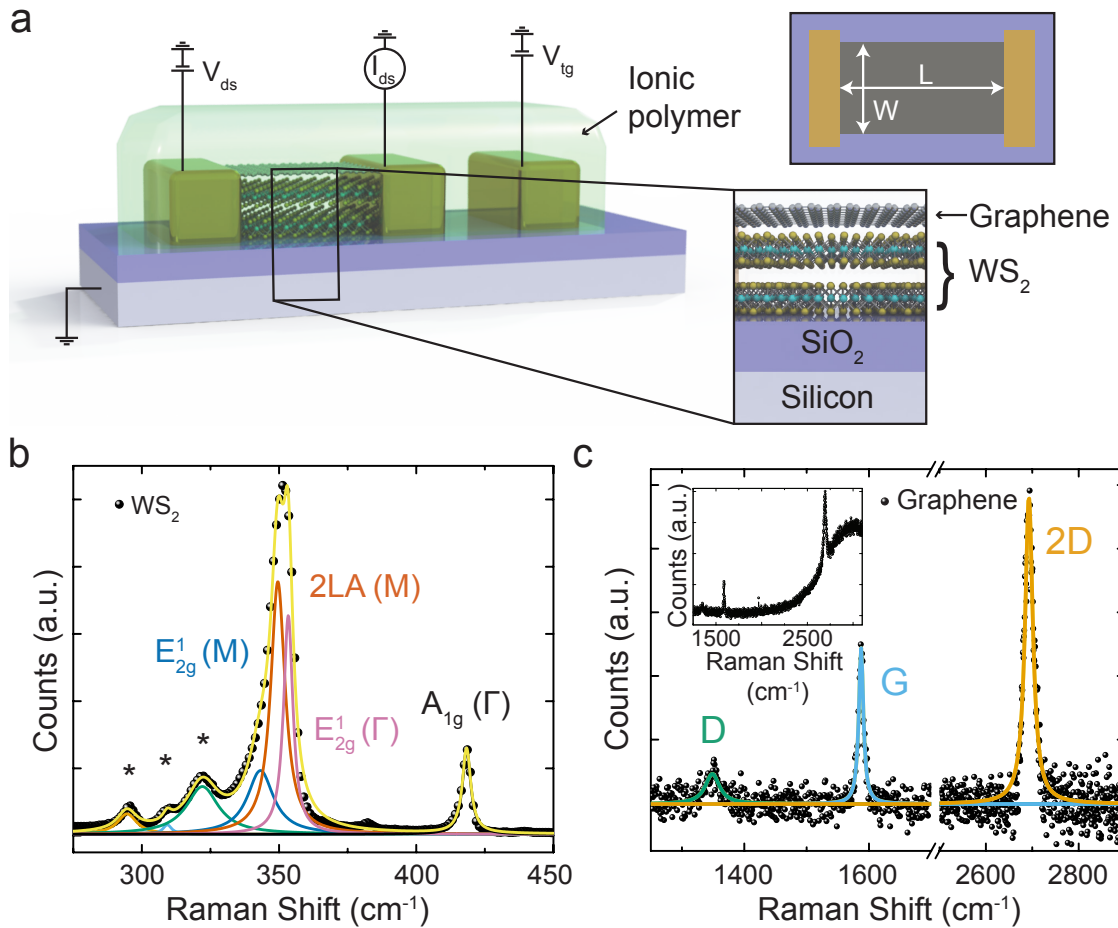
Figure 4.1: **Device schematic and Raman spectrum of the WS_2-graphene field-effect transistor.** (a) Device schematic with electrical connections included. A voltage (V_{tg}) is applied to the transparent ionic polymer (PEO + $LiClO_4$) using a gate electrode in close vicinity to the WS_2-graphene photodetector. The channel (width W, length L) current I_{ds} is collected whilst applying a bias voltage V_{ds} between the source and drain electrodes. Raman spectra of the WS_2-graphene heterostructure are shown for ranges of wavenumber relevant to (b) WS_2 and (c) graphene. Peaks are labelled following Lorentzian fits to the phonon processes. Those labelled ∗ are resonant second order processes. Inset in (c) shows the spectrum before baseline subtraction.

defined by means of O_2 plasma etching. In total 20 devices were fabricated and measured. The length and width of the graphene channel were chosen to overlap with the WS_2 flake and therefore prevent the ionic polymer from contacting the WS_2. The WS_2-graphene devices were covered by a transparent ionic polymer, lithium perchlorate poly-(ethylene oxide) ($LiClO_4$ PEO, 8:1 in methanol), which serves as a top gate, see Figure 4.1a. This transparent top gate was prepared by magnetic stirring poly-ethylene oxide (PEO) and lithium perchlorate ($LiClO_4$), at a ratio of 8:1 in methanol. After centrifugation, the deposition of the supernatant via drop-casting was left to dry at room temperature.

Raman spectra were acquired using a 532 nm laser source with a spot size of $\sim 1\,\mu m$ and an incident laser beam power $\leq 40\,\mu W$ to avoid overheating and damage

to WS$_2$-graphene. Photocurrent maps were recorded at room temperature in ambient conditions in a custom built set-up on an upright BX51 Olympus microscope.[27] The external quantum efficiency, spectral responsivity, and transient response measurements were performed in a custom built vacuum chamber (10^{-3} mbar) using a Xenon Lamp, monochromator and collimating optics (Oriel TLS-300X), to provide a spectrally tunable incident light source. Neutral density filters and a motorized chopper wheel were used to attenuate and modulate the incident signal respectively. Power calibrations were performed with a ThorLabs PM320E power meter equipped with a S130VC sensor.

Raman spectroscopy is used for the characterization of WS$_2$-graphene heterostructures and reveals peaks in two well-separated regions, 200 cm^{-1} $\leq \omega \leq$ 450 cm^{-1} and 1200 cm^{-1} $\leq \omega \leq$ 3000 cm^{-1} respectively. Lorentzian fits of the spectra reveal the presence of several peaks, which originate from the E$_{2g}$, 2LA and A$_{1g}$ modes of WS$_2$ (see Figure 4.1b).[28] The E$_{2g}$ phonon mode is an in-plane displacement of both sulphur and tungsten atoms, whereas, the A$_{1g}$ mode is an out-of-plane displacement of the sulphur atoms. The position of both modes shifts with increasing numbers of layers, and their wavenumber difference changes with layer number.[29–32] For the spectra in Figure 4.1c, a peak separation of 68.7 cm^{-1} is indicative of a trilayer WS$_2$ flake. However this method becomes unreliable for flakes thicker than 3 layers. To avoid uncertainty atomic force microscopy should be used to accurately determine flake thickness. The 2LA peak is a disorder activated overtone of the LA mode, which is the in-plane collective motions of atoms in the lattice.[30] Resonant enhancement of this mode is observed because the photon energy used in acquiring the Raman spectra lies close to the B exciton energy of WS$_2$.[33] This is consistent with the broad photoluminescence peak located at ~3100 cm^{-1}, attributed to the direct electronic transition of WS$_2$. After subtracting this photoluminescence peak from the Raman spectrum the D, G, and 2D peaks of graphene are identified with Lorentzian fits, Figure 4.1c.[34] Previous works observed the half integer quantum Hall effect in similar films - a clear indication of monolayer graphene.[26] Here the FWHM of the 2D peak (20 cm^{-1}) is used to verify monolayer thickness which is essential for high-mobility electrical transport. At the same time, the observed low D/G peak intensity ratio (~ 0.2) indicates a low defect density.[26] Finally, the fact that the measured Raman spectrum on the WS$_2$-graphene heterointerface simply is the sum of the individual spectrum for isolated WS$_2$ and graphene confirms the formation of a van der Waals interface.

4.3 Ionic polymer gating

Figure 4.2a shows the typical ambipolar electrical transport of graphene. Upon applying a bias to the ionic polymer a stable electric double layer (see Figure 4.2b)
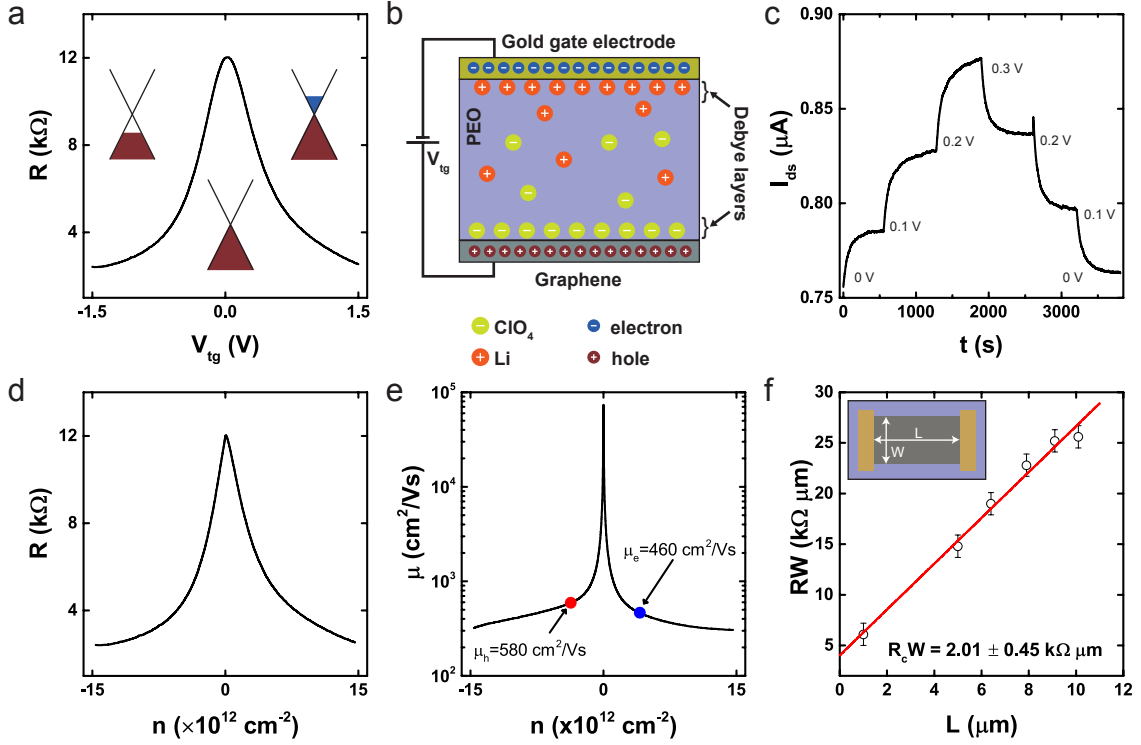
Figure 4.2: **Ionic polymer gated FET** (a) Resistance (R) versus top gate voltage (V_{tg}). Insets show Fermi level position for different V_{tg}. (b) Schematic of ionic polymer gating mechanism. (c) Stabilisation time of ionic gate for $\Delta V_{tg} = \pm 0.1\,\text{V}$. Resistance (d) and mobility (e) versus induced carrier density (n). (f) Resistance (R) scaling with channel length (L) for width (W).

is formed at the interface with graphene without the occurrence of chemical reactions within an electrochemical stability window, $-3\,\text{V} < V_{tg} < 3\,\text{V}$. After each change in V_{tg} a stabilisation period (~ 10 minutes) is required to allow the ions to reach their equilibrium position, Figure 4.2c. An extremely large gate capacitance easily attained in ionic gated transistors ($\geq 2 \times 10^{-6}\,\text{F}\,\text{cm}^{-2}$) which allows the properties of graphene to be probed at extremely high charge carrier densities $\geq 10^{14}\,\text{cm}^{-2}$.[35,36] This is due to the ~ 2 nm Debye layer,[36] which defines the effective thickness of the polymer gate dielectric in comparison to ~ 300 nm typical of SiO_2/Si. Most importantly, the ions in the polymer are highly mobile and provide a significant additional screening mechanism of charge impurities.[37]

For ionic gating the quantum capacitance of graphene becomes significant and can therefore be no longer neglected when calculating the gate-induced carrier density (n):[38]

$$V_{tg} = \frac{E_F}{e} + \phi = \frac{\hbar |v_F| \sqrt{\pi n}}{e} + \frac{ne}{C_{tg}}, \qquad (4.1)$$

where the influence of geometric capacitance (ϕ) and change in Fermi energy (E_F) on top-gate voltage are taken into account. For back-gated FETs $\phi \gg E_F/e$ and the quantum capacitance term (E_F/e) can be neglected. Using values for $C_{tg} =$

$2.2 \times 10^{-6}\,\mathrm{F\,cm^{-2}}$ and $v_F = 1.1 \times 10^6\,\mathrm{m\,s^{-1}}$ yields:

$$V_{tg}(\mathrm{V}) = 1.16 \times 10^{-7}\sqrt{n} + 0.723 \times 10^{-13}n, \qquad (4.2)$$

where n is in units of $\mathrm{cm^{-2}}$. This allows the conversion from top-gate voltage to induced carrier density, Figure 4.2d.

To extract the mobility from the transfer curves, Figure 4.2d, the Drude model has been used ($\sigma = ne\mu$). The zero bias doping of graphene due to electron hole puddles ($n_0 \sim 10^{11}\,\mathrm{cm^{-2}}$) has been accounted for in the calculations of mobility.[39] Figure 4.2e shows a plot of the extracted mobility (μ) as a function of top-gate induced carrier density. In the high-doping regime ($n > 5 \times 10^{12}\,\mathrm{cm^{-2}}$) the mobility is weakly dependent on carrier density as previously observed in samples dominated by impurity scattering due to residual charge impurities.[40] Graphene is predicted to have an intrinsic mobility of $\mu > 10^5\,\mathrm{cm^2\,V^{-1}\,s^{-1}}$ at room temperature.[40] However values reported in literature often fall short due to a combination of different limiting factors including the neighbouring dielectric medium and the presence of scattering centres. For graphene on SiO$_2$ the room temperature mobility is limited to $\mu \sim 10^4\,\mathrm{cm^2\,V^{-1}\,s^{-1}}$ due to the scattering with substrate surface phonons. It is important to consider that the graphene channel here is effectively separated from SiO$_2$ by WS$_2$. As a result the influence of substrate phonons is expected to be minimal. Instead the dominant limitation arises from the polycrystalline nature of the CVD grown films. Charge carriers will be scattered at the grain boundaries leading to a reduction in mobility and an increased $1/f$ noise.[41] These grain boundaries can be inferred from the presence of a small D peak in the Raman spectrum of Figure 4.1c. By evaluating the relative intensity of the D and G peaks a defect density can be estimated, $n_D = 8.3 \times 10^9\,\mathrm{cm^{-2}}$. A previous investigation into the correlation between defect density and mobility revealed that for $n_D \sim 10^{10}\,\mathrm{cm^{-2}}$ a mobility of $\mu \sim 600\,\mathrm{cm^2\,V^{-1}\,s^{-1}}$ was obtained.[42] Indeed when contact resistance is taken into account, Figure 4.2f, this is in excellent agreement with the final value of mobility ($580\,\mathrm{cm^2\,V^{-1}\,s^{-1}}$) highlighting the prominent role of grain boundaries on the electrical properties of these CVD-grown graphene FETs.

4.4   Mechanism of charge transfer between WS$_2$ and graphene

To determine the photo-responsive region of the fabricated WS$_2$-graphene heterostructure scanning photocurrent microscopy (SPCM) has been used. Here a focussed laser beam is rastered across the device and the photocurrent simultaneously recorded for each position.[27] Figure 4.3a shows that in the short circuit configuration ($V_{ds} = 0$ V) photocurrent generation is localised to the lateral interfaces of the
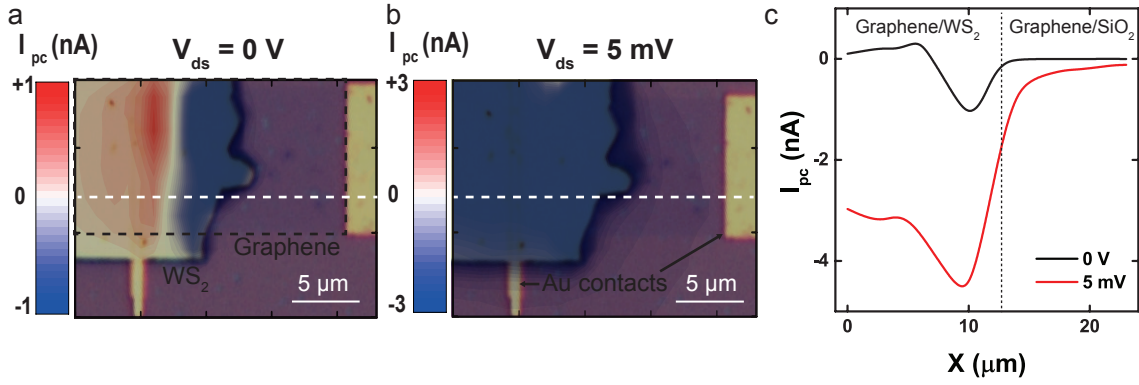
Figure 4.3: **Scanning photocurrent microscopy of heterostructure.** Scanning photocurrent maps of a large area (bulk WS_2) device in short circuit configuration, ($V_{ds} = 0$ mV), (a) and under a source drain bias, ($V_{ds} = 5$ mV), (b). (c) Profile of the photocurrent (I_{pc}) taken along the dashed white line in (a) and (b).

device, such as the edges of Au contacts and the WS_2 flake, and changes in polarity across the photo-responsive region. Upon applying a finite source-drain bias, a uniform photocurrent is generated over the entire vertical WS_2-graphene interface, see Figure 4.3b. This change can be seen more clearly in Figure 4.3c which plots a line scan for the two conditions.

To gain insight in the microscopic origin of the measured photocurrent and understand the role played by the ionic polymer gate on device performance, the photoresponse of these structures is characterized in a vacuum chamber at finite source-drain bias and under illumination with collimated light. Figure 4.4a shows an optical micrograph of the WS_2-graphene heterostructure. Upon increasing top gate voltage (V_{tg}) I_{pc} increases until $V_{tg} = -2$ V, at which point I_{pc} reaches a peak value of -18 nA, Figure 4.4b. For $V_{tg} \leq -2$ V no further increase in I_{pc} is observed. To explain the increased photocurrent under a gate bias the transfer curves ($V_{ds} = 10$ mV) taken in both dark and light (600 nm, $200 \, \mu W \, cm^{-2}$) conditions are examined, as seen in Figure 4.4c. Under illumination a reduction in the current (ΔI_{ds}) is observed and this increases for more negative gate biases. This is expected when the photocurrent generation mechanism is the photogating effect[1] where absorption of photons in WS_2 creates electron-hole pairs, which can be split at the interface between graphene and WS_2, with one charge carrier transferred to graphene and the other remaining in WS_2, as shown schematically in Figure 4.4d. The in-built fields at the interface enable this separation and arise from the work function difference between graphene and WS_2. For $V_{tg} < V_{dirac}$ illumination of the heterostructure results in an increase in resistance due to the recombination between electrons, generated in WS_2 and subsequently transferred to graphene, and electrostatically induced holes present in graphene. This manifests as a shift in the charge neutrality point (ΔV_{tg}) to negative values, indicating n-type doping. Photogenerated holes remain trapped in WS_2 and could be considered as a light induced gating potential.
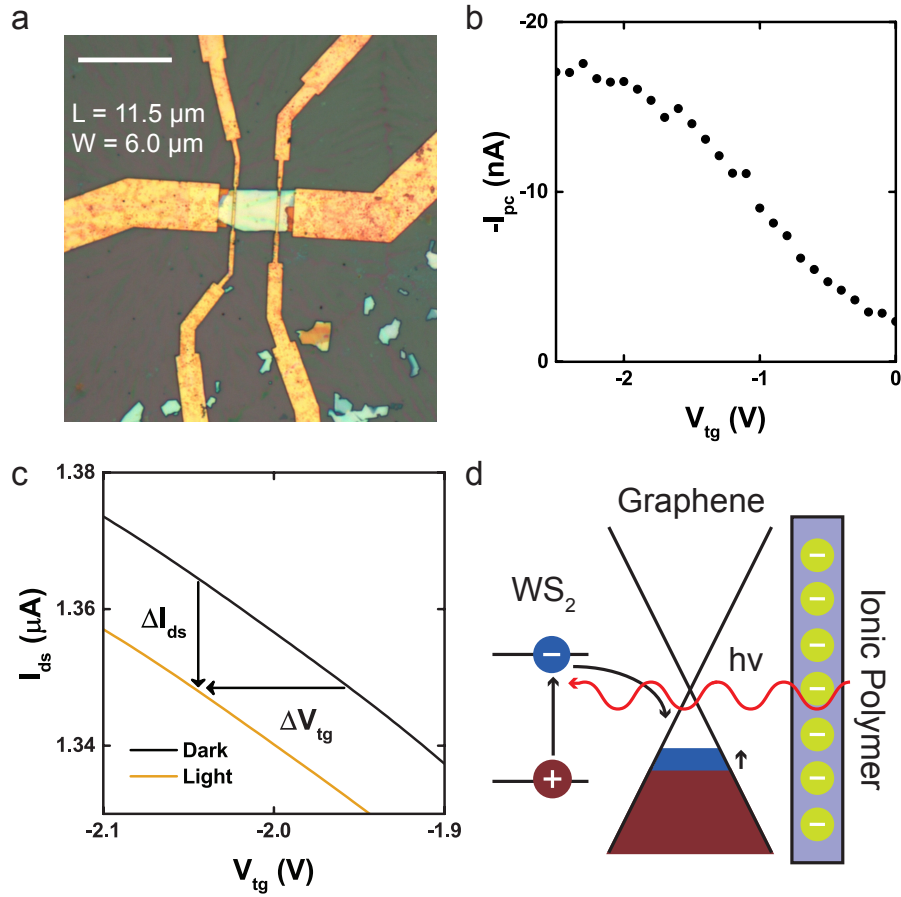
Figure 4.4: **Characterisation of optoelectronic response and charge transfer mechanism.** (a) Optical micrograph of device. Scale bar is 16 µm. (b) Photocurrent (I_{pc}) versus top gate voltage (V_{tg}). (c) Drain current (I_{ds}) versus V_{tg} in dark and under illumination. (d) Schematic of charge transfer at WS_2/graphene interface.

4.5 Spectral response of heterostructure

These devices display an energy dependent responsivity (R) when illuminated by monochromatic light, see Figure 4.5a. More specifically, a photoresponse is only observed for incident photons of energy greater than 1.8 eV, with the spectral profile of responsivity consisting of four Gaussian peaks centred at 1.92 eV, 2.06 eV and 2.36 eV, with a broader peak at 2.97 eV also present. All of these peaks relate to different electronic transitions in WS_2, as illustrated in Figure 4.5b. The sharp increase in photoresponse around 1.9 eV is due to the A exciton.[43] This exciton corresponds to the electronic transition from the upper branch of the spin-split valence band to the conduction band, and subsequent formation of a bound state between an electron and hole. The peak at 2.1 eV is the direct gap (E_g) associated with the A exciton and has been previously observed in photoconductivity measurements of WS_2.[44]

In many semiconductors excitons can be described using a Wannier-Mott 2D hydrogen model.[45] Although the applicability of this model to 2D systems can be questioned because of the increased exciton confinement,[45] in this case it is found that it serves as a reasonable approximation. From the model the binding energy, β,
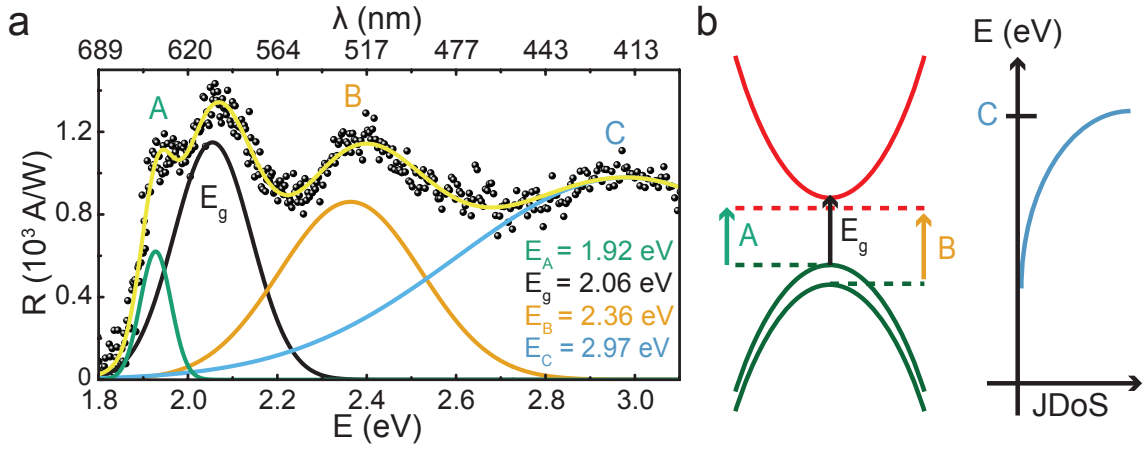
Figure 4.5: **Characterisation of the spectral response of WS$_2$-graphene heterostructures.** (a) Measured responsivity (black dots) versus incident photon energy for V_{ds} = 10 mV and V_{tg} = 0 V. A, B and C exciton peaks, as well as the direct gap transition (E_g), are fit with Gaussian functions with the cumulative fit described by the yellow continuous line. (b) Schematic of electronic transitions responsible for each peak fitted in the spectral responsivity of WS$_2$/graphene interface.

is extracted using $E_A = E_g - \beta$ which gives $\beta = 140$ meV which is a value between that of bulk (~ 50 meV)[43] and monolayer ($\sim 300 - 800$ meV)[45,46] WS$_2$. Such a high binding energy inhibits the contribution of excitons to the measured photocurrent unless they can dissociate into an unbound electron-hole pair and be transferred to the graphene charge transport layer.[47] This dissociation can occur as long as the binding energy can be overcome which typically requires large electric fields. The in-built field at the interface, arising from the work function mismatch ($\Delta\phi$) between graphene and WS$_2$ could encourage this dissociation, although the estimate of $\Delta\phi \sim 100$ meV indicates that this alone would not be sufficient. Applying a non-zero value of V_{tg} creates large electric fields at the surface of graphene which can contribute to the exciton dissociation in WS$_2$ as the fields are not completely screened by graphene.[48] This has been verified by taking spectral scans at different top gate biases.

Finally, the peak at 2.36 eV is due to the exciton formed from the electronic transition originating in the lower branch of the valence band. The difference in energy between this B exciton and the A exciton allows us to extract a spin-orbit splitting energy of 440 meV, which is in good agreement with both theoretical[49] and other experimental[50] works. The broad peak at 2.97 eV, Figure 4.5a, can be attributed to transitions between regions of high density of states in the valence and conduction bands which give these materials their strong light-matter interaction.[51] The joint density of states (JDoS) exhibits this in a clearer fashion and has a prominent peak around this energy, see Figure 4.5b.
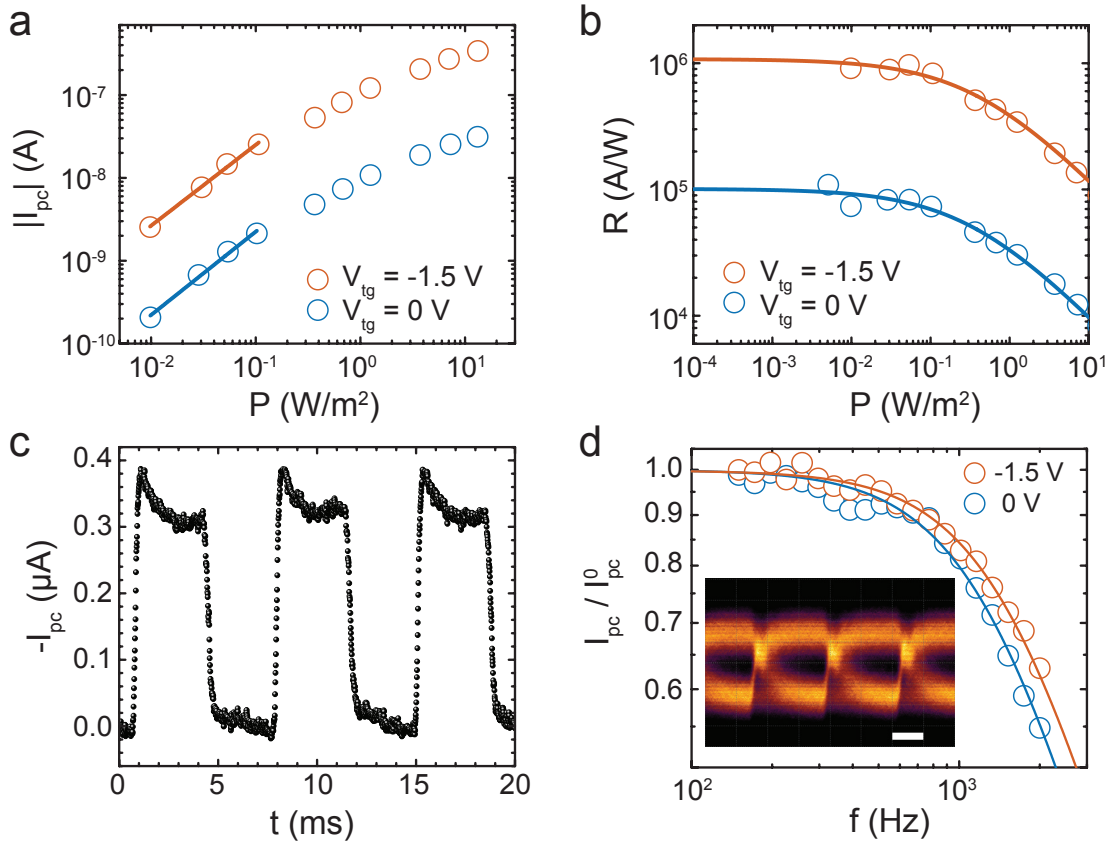
Figure 4.6: **Photodetector performance of WS$_2$-graphene heterostructures.**
(a) Photocurrent ($|I_{pc}|$) and (b) responsivity (R) as a function of incident optical power (P) at $V_{ds} = 100$ mV. (c) Temporal response of the device at $V_{ds} = 100$ mV and $V_{tg} = -1.5$ V. (d) Normalised photoresponse as a function of light modulation frequency. Inset shows eye diagram acquired at 2.9 kbit s^{-1}. Scale bar is 150 μs.

4.6 Performance of photodetectors

From Figures 4.4 and 4.5 it follows that the whole WS$_2$-graphene interface is photoactive and its photosensitivity extends across the spectral range 400 - 700 nm. To fully characterise performance the device has been illuminated with monochromatic light ($\lambda = 625$ nm) of varying intensity and the photocurrent was recorded. Figure 4.6a shows the photocurrent as a function of incident optical power at zero and finite negative bias applied to the polymer gate. For both conditions the photocurrent decreases with reducing optical power, transitioning from a sub-linear power dependence to a linear one below 0.1 W/m^2. In the linear regime, indicated by the straight line fits, photogenerated charge carriers are split, with one charge type being transferred to the graphene channel whilst the other remains trapped in the WS$_2$. Upon increasing the illumination intensity, the large number of photogenerated charge carriers reduces the electric field at the heterointerface, resulting in a sub-linear power dependence.[4,9] Application of a bias to the polymer gate allows for more efficient exciton splitting within WS$_2$ leading to an increase in I_{pc}, as seen previously in Figure 4.4b.

In Figure 4.6b the responsivity as a function of incident optical power is plotted for both $V_{tg} = 0$ V and $V_{tg} = -1.5$ V. The responsivity has been calculated using $R = I_{pc}/P$, where I_{pc} is the photocurrent and P the incident optical power, and follows a non-linear power dependence. This can be well fit using a function of the form $R = a/(b + P^n)$, where a, b and n are fitting parameters. The power exponent $n \sim 2/3$ is indicative of non-radiative Auger recombination,[52] previously observed in other indirect semiconductors such as Ge and Si.[53] The responsivities reach a maximal value of 1×10^6 A W^{-1} at $V_{tg} = -1.5$ V for $V_{ds} = 100$ mV, an order of magnitude higher than that without a bias applied to the top gate. The high responsivities observed in these devices can be explained in terms of a gain mechanism arising from the aforementioned photogating effect; to maintain charge conservation the removal of one electron at a contact requires the injection of one at the opposite contact. This electron circulation exists as long as the holes remain trapped in the WS$_2$ resulting in a net gain.[1] The gain (G) in these devices can be theoretically calculated considering the change in carrier density (Δn) from a known photon flux (ϕ).

Solving equation 4.2 numerically around $V_{tg} = 2$ V and using $\Delta V_{tg} = 114$ mV gives $\Delta n = 1.3 \times 10^{12}$ cm^{-2}. From this the gain is estimated using:

$$G_{th} = \frac{\Delta n \times \mu \times V_{ds}}{L^2 \phi}, \tag{4.3}$$

where L is the channel length and V_{ds} the applied source drain bias. With a value for mobility of $\mu = 560$ cm^{2}V^{-1}s^{-1} extracted from the transfer curves, see Figure 4.2, and a photon flux $(\phi = 6 \times 10^{14}$ cm^{2}s$^{-1})$, we find that $G_{th} = 4.8 \times 10^6$, which is in excellent agreement with the experimental measurement of responsivity, Figure 4.6b.

The temporal response of a polymer gated WS$_2$-graphene device is shown in Figure 4.6c at $V_{ds} = 100$ mV and $V_{tg} = -1.5$ V whilst the incident light is modulated at 140 Hz. The rise and fall times are defined as the time period taken for ΔI_{pc} to change from $10\,\%$ $(90\,\%)$ to $90\,\%$ $(10\,\%)$ of its maximum value respectively. Analysing multiple iterations of this square wave signal reveals that the transient response of the WS$_2$-graphene photodetectors takes place over sub-millisecond timescales with $\tau_{rise} = 130\,\mu$s and $\tau_{fall} = 440\,\mu$s. Prior to encapsulation in the ionic polymer these devices typically had rise and fall times > 1 s, often with the decay of the photocurrent signal persisting well beyond the time frame of the experiment. After deposition of the ionic polymer the response times of these devices improved by at least four orders of magnitude, resulting in sub-millisecond rise and fall times, as seen in Figure 4.6c.

These response times are 10^4 faster than previously reported heterostructure photodetectors which utilise TMDs[9,10] or QDs[4,5] as a light absorbing layer, typically operating over time scales of seconds or greater, owing to long lived charge

trapping present in these devices. Typically, a large gate pulse is applied to reduce the potential barrier between graphene and the semiconductor, thereby accelerating the recombination rate of photogenerated electrons and holes, allowing a swift transition back to dark conditions. Indeed, hysteresis in current-gate sweeps of carbon nanotubes, attributed to atmospheric contamination and oxide charge traps, can be resolved through gate pulsing strategies.[18] However, for graphene-QDs these gate-pulses have been found to be device specific.[4] These devices exhibit rise and fall times that are up to five orders of magnitude faster than previous works, without the need to apply large electrical pulses. This behaviour is attributed to the screening of traps within WS_2, and at the SiO_2 interface, the latter of which is responsible for the localization of charges in monolayer TMDs,[14] by the mobile ions within the ionic polymer. Therefore, the population of long-lived charge traps by photogenerated charges is unlikely, which allows for a swift return to the initial dark state following removal of light.

In Figure 4.6d, these response times are verified by ascertaining the -3 dB bandwidth of polymer gated WS_2-graphene photodetectors. The decline in photocurrent magnitude is measured as an incident light signal is modulated with increasing frequency using an optical chopper wheel. A similar trend is shown for the situation with and without a bias applied to the polymer gate, where photocurrent signals are normalised to the maximum, which occurs at low modulation frequencies. The normalised signal reduces when increasing frequency, as one would expect when the period of modulation begins to impinge upon the rise and fall times of the device. The -3 dB bandwidth, a common figure of merit for photodetectors, is the point at which the signal has dropped to 70% of its initial value, which for these devices are 1.3 kHz ($V_{tg} = 0$ V) and 1.5 kHz ($V_{tg} = -1.5$ V). From this a rise time is extracted using $\tau_{rise} \approx 0.35/f_{-3dB}$ of 220 μs, in good agreement with the data extracted from Figure 4.6c.

This -3 dB bandwidth of 1.5 kHz, coupled with extremely sensitive photodetection across a broad spectral range, means that WS_2-graphene heterostructures are highly suitable for video-frame-rate imaging applications, thanks to the unique screening properties of the ionic polymer top gate. To demonstrate the feasibility of this claim a home-built optical data link was constructed with a pseudo-random bit sequence generator used to modulate the 625 nm light of an LED. This light was focussed onto the WS_2-graphene heterostructure maintained at $V_{ds} = 100$ mV and $V_{tg} = -1.5$ V and the output data stream amplified and delivered into an oscilloscope to obtain an eye diagram. The inset in Figure 4.6d shows such an eye diagram, with the open eye at 2.9 kbit s^{-1} demonstrating that these heterostructures can truly be used in video-frame-rate imaging applications.

Finally in order to directly compare the performance of WS_2-graphene heterostructures to that of other photodetectors the specific detectivity (D^*) is used.
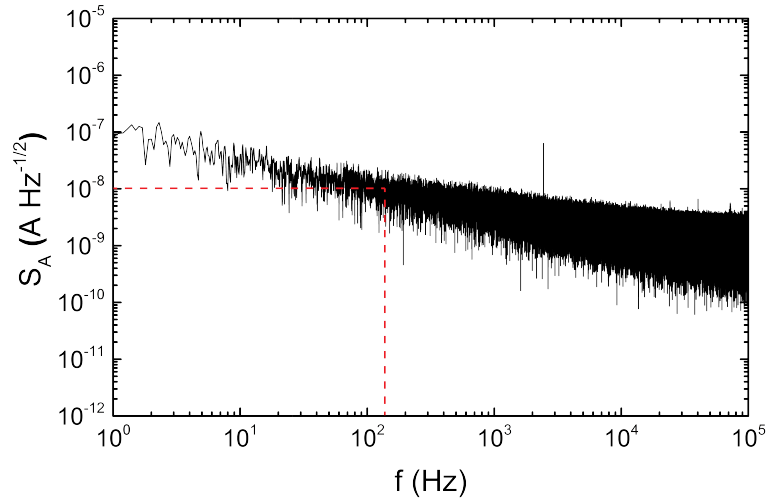
Figure 4.7: **Photodetector noise** Acquired in dark for $V_{ds} = 100\,\mathrm{mV}$ and $V_{tg} = -1.5\,\mathrm{V}$.

This formalism attempts to remove the variation in performance between devices arising from different measurement conditions or geometries. This can be calculated using the responsivity (R) and the noise density (S_A, see Figure 4.7) using $D^* = R\sqrt{A}/S_A$ where A is the device area. Taking the responsivity at $V_{tg} = -1.5$ V and noise value extracted at 150 Hz, a value for detectivity is calculated $D^* = 3.8 \times 10^{11}$ Jones which is comparable to other graphene hybrid photodetectors.[4–7,9,10,54]

4.7 Comparison with literature

The significant novelty which separates this work from previous reports is that these phototransistors display (1) high operational bandwidth and (2) high photo-conductive gain at room temperature. Figure 4.8 shows a comparative plot of gain versus bandwidth for all relevant studies concerning graphene-based phototransistors. The diagonal line in this diagram indicates a gain-bandwidth product of 1 GHz which is comparable to established technology based on III-V phototransistors.[55] These devices greatly outperform any previously demonstrated photosensors of atomically thin materials.

Prior to this study, enhancements in the gain bandwidth product of graphene phototransistors have only been realized using the impractical strategies of cryogenic cooling to reduce electrical noise and the application of large ($\geq$10 V) gate voltage pulses to accelerate resetting times (see hollow data points in Figure 4.8). Crucially, the encapsulation of the phototransistor in ionic polymer results in a two order of magnitude enhancement in operational bandwidth.
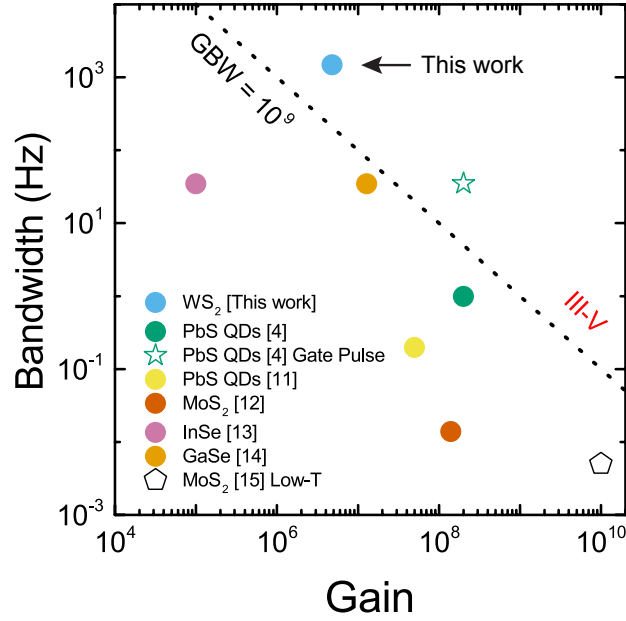
Figure 4.8: **Literature comparison** Reported values for bandwidth and gain for hybrid graphene transistors.

4.8 Summary and outlook

To summarise, the optoelectronic properties of ionic polymer gated WS_2-graphene heterostructure photodetectors has been characterised across a broad spectral range. The photogating effect has been found to be the dominant photocurrent generation mechanism, with a high gain process resulting in responsivities of 1×10^6 A W^{-1}. Furthermore, sub-millisecond response times are demonstrated through both rise and fall time estimates as well as by measuring a -3 dB bandwidth of 1.5 kHz. The high gain and fast response found in these devices arises from the ability to compensate charge traps with the ionic polymer, which is a limiting factor in similar photodetectors. This study demonstrates that both high gain and sub-millisecond response times can be achieved in two-dimensional heterostructure photodetectors. A calculated detectivity of 3.8×10^{11} Jones brings the realisation of high frame-rate video-imaging applications with 2D materials ever closer.

References

[1] F. H. L. Koppens, T Mueller, Ph. Avouris, a C Ferrari, M S Vitiello, and M Polini. Photodetectors based on graphene, other two-dimensional materials and hybrid systems. *Nature Nanotechnology*, 9(10):780–793, oct 2014.

[2] A I S Neves, T H Bointon, L V Melo, S Russo, I de Schrijver, M F Craciun, and H Alves. Transparent conductive graphene textile fibers. *Scientific Reports*, 5(1):9866, sep 2015.

[3] Thomas Mueller, Fengnian Xia, and Phaedon Avouris. Graphene photodetectors for high-speed optical communications. *Nature Photonics*, 4(5):297–301, mar 2010.

[4] Gerasimos Konstantatos, Michela Badioli, Louis Gaudreau, Johann Osmond, Maria Bernechea, F. Pelayo Garcia de Arquer, Fabio Gatti, and Frank H. L. Koppens. Hybrid graphene–quantum dot phototransistors with ultrahigh gain. *Nature Nanotechnology*, 7(6):363–368, may 2012.

[5] Zhenhua Sun, Zhike Liu, Jinhua Li, Guo-an Tai, Shu-Ping Lau, and Feng Yan. Infrared Photodetectors Based on CVD-Grown Graphene and PbS Quantum Dots with Ultrahigh Responsivity. *Advanced Materials*, 24(43):5878–5883, nov 2012.

[6] Ivan Nikitskiy, Stijn Goossens, Dominik Kufer, Tania Lasanta, Gabriele Navickaite, Frank H. L. Koppens, and Gerasimos Konstantatos. Integrating an electrically active colloidal quantum dot photodiode with a graphene phototransistor. *Nature Communications*, 7(May):11954, 2016.

[7] Shao Yu Chen, Yi Ying Lu, Fu Yu Shih, Po Hsun Ho, Yang Fang Chen, Chun Wei Chen, Yit Tsong Chen, and Wei Hua Wang. Biologically inspired graphene-chlorophyll phototransistors with high gain. *Carbon*, 63:23–29, 2013.

[8] Kallol Roy, Medini Padmanabhan, Srijit Goswami, T. Phanindra Sai, Sanjeev Kaushal, and Arindam Ghosh. Optically active heterostructures of graphene and ultrathin MoS2. *Solid State Communications*, 175-176:35–42, dec 2013.

[9] Kallol Roy, Medini Padmanabhan, Srijit Goswami, T Phanindra Sai, Gopalakrishnan Ramalingam, Srinivasan Raghavan, and Arindam Ghosh. Graphene–MoS2 hybrid structures for multifunctional photoresponsive memory devices. *Nature Nanotechnology*, 8(11):826–830, oct 2013.

[10] Wenjing Zhang, Chih-Piao Chuu, Jing-Kai Huang, Chang-Hsiao Chen, Meng-Lin Tsai, Yung-Huang Chang, Chi-Te Liang, Yu-Ze Chen, Yu-Lun Chueh, Jr-Hau He, Mei-Yin Chou, and Lain-Jong Li. Ultrahigh-Gain Photodetectors Based on Atomically Thin Graphene-MoS2 Heterostructures. *Scientific Reports*, 4(1):3826, may 2014.

[11] Martin Egginger, Siegfried Bauer, Reinhard Schwödiauer, Helmut Neugebauer, and Niyazi Serdar Sariciftci. Current versus gate voltage hysteresis in organic field effect transistors. *Monatshefte fur Chemie*, 140(7):735–750, 2009.

[12] P Joshi, H E Romero, a T Neal, V K Toutam, and S a Tadigadapa. Intrinsic doping and gate hysteresis in graphene field effect devices fabricated on SiO2 substrates. *Journal of physics. Condensed matter : an Institute of Physics journal*, 22(33):334214, aug 2010.

[13] Haomin Wang, Yihong Wu, Chunxiao Cong, Jingzhi Shang, and Ting Yu. Hysteresis of electronic transport in graphene transistors. *ACS Nano*, 4(12):7221–7228, 2010.

[14] Subhamoy Ghatak, Atindra Nath Pal, and Arindam Ghosh. Nature of electronic states in atomically thin MoS2 field-effect transistors. *ACS Nano*, 5(10):7707–7712, 2011.

[15] H. Lin and S. Tiwari. Localized charge trapping due to adsorption in nanotube field-effect transistor and its field-mediated transport. *Applied Physics Letters*, 89(7):073507, 2006.

[16] Dattatray J. Late, Bin Liu, H. S S Ramakrishna Matte, Vinayak P. Dravid, and C. N R Rao. Hysteresis in single-layer MoS 2 field effect transistors. *ACS Nano*, 6(6):5635–5641, jun 2012.

[17] Kyungjune Cho, Woanseo Park, Juhun Park, Hyunhak Jeong, Jingon Jang, Tae Young Kim, Woong Ki Hong, Seunghun Hong, and Takhee Lee. Electric stress-induced threshold voltage instability of multilayer MoS2 field effect transistors. *ACS Nano*, 7(9):7751–7758, 2013.

[18] M Mattmann, C Roman, T Helbling, D Bechstein, L Durrer, R Pohle, M Fleischer, and C Hierold. Pulsed gate sweep strategies for hysteresis reduction in carbon nanotube transistors for low concentration NO 2 gas detection. *Nanotechnology*, 21(18):185501, 2010.

[19] Chunrui Ma, Youpin Gong, Rongtao Lu, Emery Brown, Beihai Ma, Jun Li, and Judy Wu. Detangling extrinsic and intrinsic hysteresis for detecting dynamic switch of electric dipoles using graphene field-effect transistors on ferroelectric gates. *Nanoscale*, 7(44):18489–18497, 2015.

[20] Jun Yan and Michael S. Fuhrer. Correlated charged impurity scattering in graphene. *Physical Review Letters*, 107(20):206601, nov 2011.

[21] Dmitry Ovchinnikov, Adrien Allain, Ying Sheng Huang, Dumitru Dumcenco, and Andras Kis. Electrical transport properties of single-layer WS2. *ACS Nano*, 8(8):8174–8181, 2014.

[22] Taner Ozel, Anshu Gaur, John A. Rogers, and Moonsub Shim. Polymer electrolyte gating of carbon nanotube network transistors. *Nano Letters*, 5(5):905–911, may 2005.

[23] Ming-Wei Lin, Lezhang Liu, Qing Lan, Xuebin Tan, Kulwinder S Dhindsa, Peng Zeng, Vaman M Naik, Mark Ming-Cheng Cheng, and Zhixian Zhou. Mobility enhancement and highly efficient gating of monolayer MoS 2 transistors with polymer electrolyte. *Journal of Physics D: Applied Physics*, 45(34):345102, aug 2012.

[24] Nicolas Ubrig, Sanghyun Jo, Helmuth Berger, Alberto F. Morpurgo, and Alexey B. Kuzmenko. Scanning photocurrent microscopy reveals electron-hole asymmetry in ionic liquid-gated WS2 transistors. *Applied Physics Letters*, 104(17):171112, apr 2014.

[25] Manabendra Kuiri, Biswanath Chakraborty, Arup Paul, Subhadip Das, A. K. Sood, and Anindya Das. Enhancing photoresponsivity using MoTe2-graphene vertical heterostructures. *Applied Physics Letters*, 108(6):063506, feb 2016.

[26] Thomas H Bointon, Matthew D Barnes, Saverio Russo, and Monica F Craciun. High Quality Monolayer Graphene Synthesized by Resistive Heating Cold Wall Chemical Vapor Deposition. *Advanced Materials*, 27(28):4200–4206, jul 2015.

[27] Adolfo De Sanctis, Gareth F. Jones, Nicola J. Townsend, Monica F. Craciun, and Saverio Russo. An integrated and multi-purpose microscope for the characterization of atomically thin optoelectronic devices. *Review of Scientific Instruments*, 88(5):055102, may 2017.

[28] T. Sekine, T. Nakashizu, K. Toyoda, K. Uchinokura, and E. Matsuura. Raman scattering in layered compound 2H-WS2. *Solid State Communications*, 35(4):371–373, 1980.

[29] Humberto R. Gutiérrez, Nestor Perea-López, Ana Laura Elías, Ayse Berkdemir, Bei Wang, Ruitao Lv, Florentino López-Urías, Vincent H. Crespi, Humberto Terrones, and Mauricio Terrones. Extraordinary Room-Temperature Photoluminescence in Triangular WS 2 Monolayers. *Nano Letters*, 13(8):3447–3454, aug 2013.

[30] Ayse Berkdemir, Humberto R Gutiérrez, Andrés R Botello-Méndez, Néstor Perea-López, Ana Laura Elías, Chen-Ing Chia, Bei Wang, Vincent H Crespi, Florentino López-Urías, Jean-Christophe Charlier, Humberto Terrones, and Mauricio Terrones. Identification of individual and few layers of WS2 using Raman Spectroscopy. *Scientific Reports*, 3:1755, apr 2013.

[31] Freddie Withers, Thomas Hardisty Bointon, David Christopher Hudson, Monica Felicia Craciun, and Saverio Russo. Electron transport of WS2 transistors in a hexagonal boron nitride dielectric environment. *Scientific Reports*, 4:4967, may 2014.

[32] Amit S. Pawbake, Mahendra S. Pawar, Sandesh R. Jadkar, and Dattatray J. Late. Large area chemical vapor deposition of monolayer transition metal dichalcogenides and their temperature dependent Raman spectroscopy studies. *Nanoscale*, 8(5):3008–3018, 2016.

[33] A. M. Stacy and D. T. Hodul. Raman spectra of IVB and VIB transition metal disulfides using laser energies near the absorption edges. *Journal of Physics and Chemistry of Solids*, 46(4):405–409, 1985.

[34] Andrea C. Ferrari and Denis M. Basko. Raman spectroscopy as a versatile tool for studying the properties of graphene. *Nature Nanotechnology*, 8(4):235–246, apr 2013.

[35] J Ye, M F Craciun, M Koshino, S Russo, S Inoue, H Yuan, H Shimotani, A F Morpurgo, and Y Iwasa. Accessing the transport properties of graphene and its multilayers at high carrier density. *Proceedings of the National Academy of Sciences of the United States of America*, 108(32):13002–13006, 2011.

[36] Chenguang Lu, Qiang Fu, Shaoming Huang, and Jie Liu. Polymer electrolyte-gated carbon nanotube field-effect transistor. *Nano Letters*, 4(4):623–627, 2004.

[37] P. Sharma and Z. L. Mišković. Ionic screening of charged impurities in electrolytically gated graphene: A partially linearized Poisson-Boltzmann model. *The Journal of Chemical Physics*, 143(13):134118, oct 2015.

[38] A Das, S Pisana, B Chakraborty, S Piscanec, S K Saha, U V Waghmare, K S Novoselov, H R Krishnamurthy, A K Geim, A C Ferrari, and A K Sood. Monitoring dopants by Raman scattering in an electrochemically top-gated graphene transistor. *Nature Nanotechnology*, 3(4):210–215, apr 2008.

[39] C. Stampfer, F. Molitor, D. Graf, K. Ensslin, A. Jungen, C. Hierold, and L. Wirtz. Raman imaging of doping domains in graphene on SiO2. *Applied Physics Letters*, 91(24):241907, dec 2007.

[40] Jian-Hao Chen, Chaun Jang, Shudong Xiao, Masa Ishigami, and Michael S. Fuhrer. Intrinsic and extrinsic performance limits of graphene devices on SiO2. *Nature Nanotechnology*, 3(4):206–209, apr 2008.

[41] Vidya Kochat, Chandra Sekhar Tiwary, Tathagata Biswas, Gopalakrishnan Ramalingam, Kimberly Hsieh, Kamanio Chattopadhyay, Srinivasan Raghavan, Manish Jain, and Arindam Ghosh. Magnitude and Origin of Electrical Noise at Individual Grain Boundaries in Graphene. *Nano Letters*, 16(1):562–567, jan 2016.

[42] Jeong-Yuan Hwang, Chun-Chiang Kuo, Li-Chyong Chen, and Kuei-Hsien Chen. Correlating defect density with carrier mobility in large-scaled graphene films: Raman spectral signatures for the estimation of defect density. *Nanotechnology*, 21(46):465705, nov 2010.

[43] J.A. Wilson and A.D. Yoffe. The transition metal dichalcogenides discussion and interpretation of the observed optical, electrical and structural properties. *Advances in Physics*, 18(73):193–335, may 1969.

[44] C. Ballif, M. Regula, P. E. Schmid, M. Remškar, R. Sanjinés, and F. Lévy. Preparation and characterization of highly oriented, photoconducting WS2 thin films. *Applied Physics A Materials Science & Processing*, 62(6):543–546, jun 1996.

[45] Alexey Chernikov, Timothy C. Berkelbach, Heather M. Hill, Albert Rigosi, Yilei Li, Ozgur Burak Aslan, David R. Reichman, Mark S. Hybertsen, and Tony F. Heinz. Exciton binding energy and nonhydrogenic Rydberg series in monolayer WS2. *Physical Review Letters*, 113(7):1–5, 2014.

[46] A. T. Hanbicki, M. Currie, G. Kioseoglou, A. L. Friedman, and B. T. Jonker. Measurement of high exciton binding energy in the monolayer transition-metal dichalcogenides WS2 and WSe2. *Solid State Communications*, 203:16–20, 2015.

[47] A. R. Klots, A. K. M. Newaz, Bin Wang, D. Prasai, H. Krzyzanowska, Junhao Lin, D. Caudel, N. J. Ghimire, J. Yan, B. L. Ivanov, K. A. Velizhanin, A. Burger, D. G. Mandrus, N. H. Tolk, S. T. Pantelides, and K. I. Bolotin. Probing excitonic states in suspended two-dimensional semiconductors by photocurrent spectroscopy. *Scientific Reports*, 4:6608, oct 2014.

[48] Yang Li, Cheng Yan Xu, Jing Kai Qin, Wei Feng, Jia Ying Wang, Siqi Zhang, Lai Peng Ma, Jian Cao, Ping An Hu, Wencai Ren, and Liang Zhen. Tuning the Excitonic States in MoS2/Graphene van der Waals Heterostructures via Electrochemical Gating. *Advanced Functional Materials*, 26(2):293–302, 2016.

[49] Ashwin Ramasubramaniam. Large excitonic effects in monolayers of molybdenum and tungsten dichalcogenides. *Physical Review B - Condensed Matter and Materials Physics*, 86(11):115409, sep 2012.

[50] Weijie Zhao, Zohreh Ghorannevis, Leiqiang Chu, Minglin Toh, Christian Kloc, Ping-Heng Heng Tan, and Goki Eda. Evolution of Electronic Structure in Atomically Thin Sheets of WS 2 and WSe 2. *ACS Nano*, 7(1):791–797, jan 2013.

[51] L Britnell, R M Ribeiro, A Eckmann, R Jalil, B D Belle, A Mishchenko, Y Kim, R V Gorbachev, T Georgiou, S V Morozov, A N Grigorenko, A K Geim, C Casiraghi, A H Castro Neto, and K S Novoselov. Strong Light-Matter Interactions in heterostructures of atomically Thin Films. *Science*, 340(6238):1331–1314, jun 2013.

[52] R.N. Hall. Recombination processes in semiconductors. *Proceedings of the IEE - Part B: Electronic and Communication Engineering*, 106(17S):923–931, may 1959.

[53] Robert E Wagner and Andreas Mandelis. Nonlinear photothermal modulated optical reflectance and photocurrent phenomena in crystalline semiconductors: II. Experimental. *Semiconductor Science and Technology*, 11(3):300–307, mar 1996.

[54] Haijie Tan, Ye Fan, Yingqiu Zhou, Qu Chen, Wenshuo Xu, and Jamie H. Warner. Ultrathin 2D Photodetectors Utilizing Chemical Vapor Deposition Grown WS2 with Graphene Electrodes. *ACS Nano*, 10(8):7866–7873, aug 2016.

[55] L. Y. Leu, J. T. Gardner, and S. R. Forrest. A high-gain, high-bandwidth In 0.53 Ga 0.47 As/InP heterojunction phototransistor for optical communications. *Journal of Applied Physics*, 69(2):1052–1062, jan 1991.

Light-emission and detection in HfOx heterostructures

5.1   Introduction

Silicon has dominated the semiconductor industry for over 50 years due to the ease at which the electronic properties can be modified by doping and the high quality of the native oxide that can be grown on the surface. Indeed silicon transistors are at the foundation of modern electronic devices. However in order to maintain transistor scaling requirements alternative materials and strategies are required. One such example is the use of high-k dielectrics such as HfO_2 as a replacement for SiO_2 in FETs. This increases the capacitive coupling between gate and channel. Therefore the use of a thicker high-k dielectric achieves the same performance as a thinner low-k material but with reduced gate leakage. Recently reports have shown similar high-k native oxides in 2D materials such as $HfSe_2$, $ZrSe_2$, TaS_2, and $TaSe_2$.[1–3]

Vertically stacked heterostructures of two-dimensional materials provide a framework for the creation of large-area, yet atomically thin and flexible optoelectronic devices with photodetectors[4–6] and light-emitting diodes[7–9] already demonstrated. Presently van der Waals nano-electronics use hBN as the dielectric layer. To achieve high performance and low power consumption the dielectric thickness has to be minimized, however thin hBN suffers from increased leakage current preventing further downscaling.

Conventional high-k deposition techniques such as atomic layer deposition or
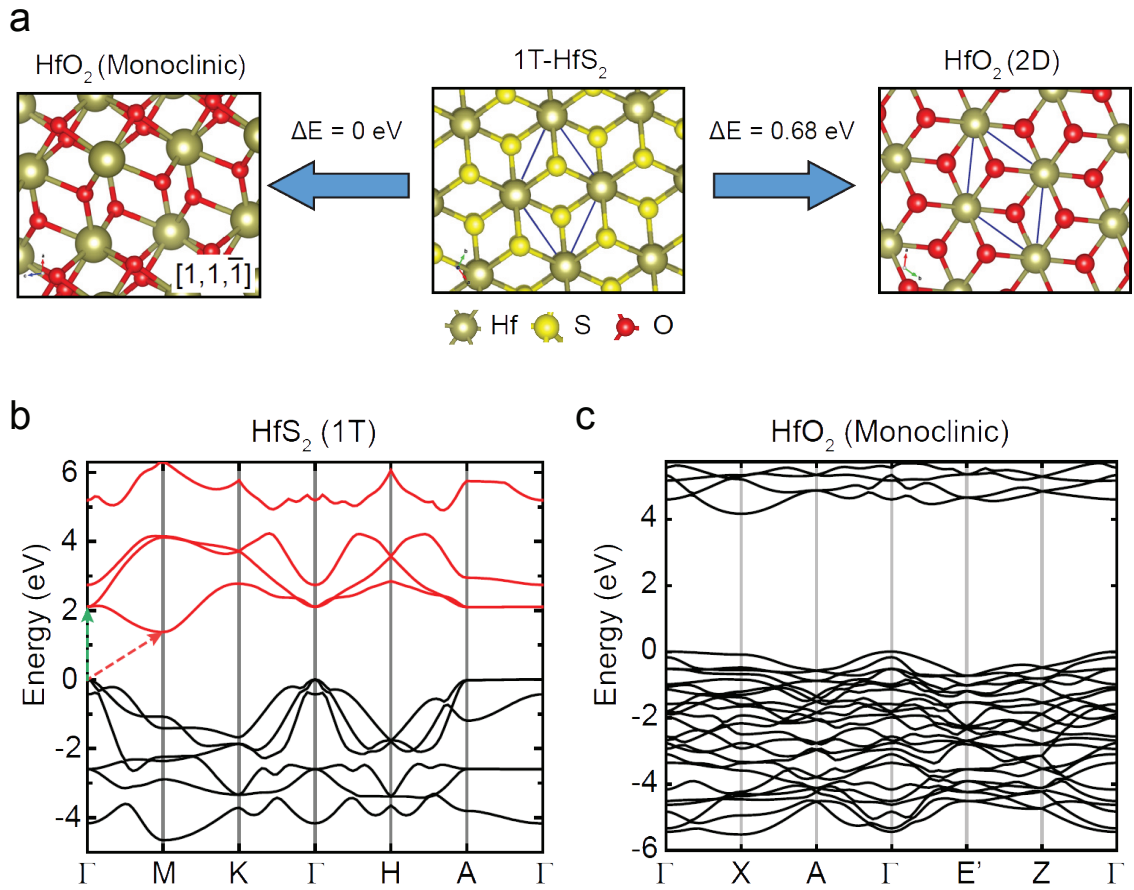
Figure 5.1: **HfO₂/HfS₂ oxidation process and band structure** (a) Simulated crystal structures and associated energy cost relative to formation of monoclinic HfO₂. Band structure of HfS₂ (b) and HfO₂ (c). Direct (indirect) transition shown in green (red). Adapted under CC-BY 4.0[14]

evaporation are incompatible with 2D materials as they tend to damage or permanently modify the electronic properties of the underlying crystal.[10–12] Other options include the integration of atomically thin oxides, such as V_2O_5 into van der Waals heterostructures. However these result in large charge transfer to neighbouring 2D materials, hysteresis in FETs and a significant reduction in mobility - all highly undesirable.[13]

In this chapter the incorporation of a high-k dielectric into van der Waals heterostructures is demonstrated. In-situ photo-oxidisation of HfS₂ allows the formation of clean interfaces between adjacent layers whilst preserving their electronic properties. As a demonstration of this technique multifunctional heterostructure devices are produced and characterised.

5.2 Crystal structure of HfS₂ and HfO₂

Figure 5.1a shows the crystal structure of 1T-HfS₂ where hafnium atoms are between two layers of sulphur atoms. Previous works have shown that 2D semiconductors
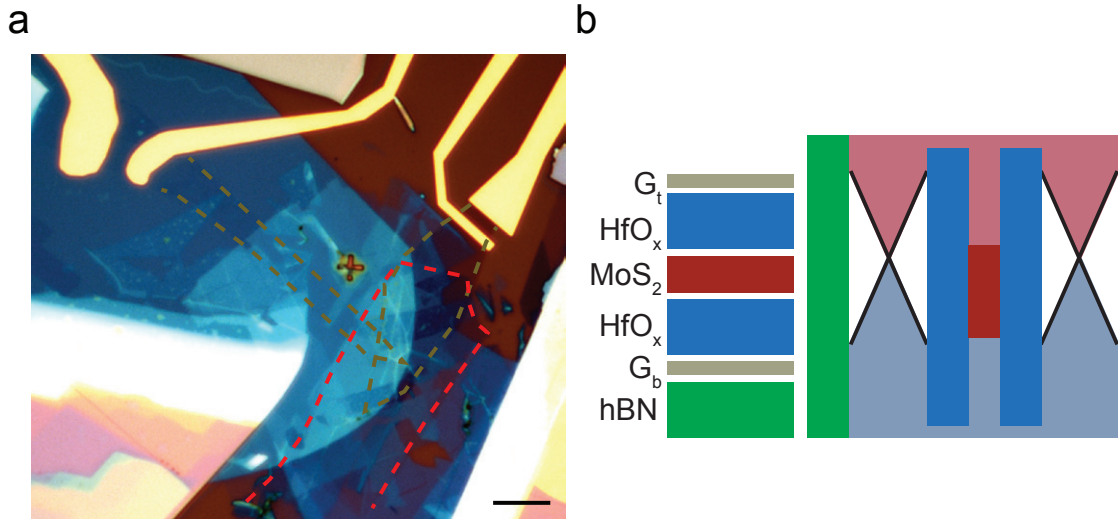
Figure 5.2: **Device Structure** (a) Optical micrograph of device. Edges of graphene (MoS$_2$) outlined in green (red). Scale bar is 6 μm. (b) Schematic of layer sequence and band structure.

are susceptible to photo-oxidation due to charge transfer between the surface and oxygen present in air or surface-bound water.[14,15] Under illumination photons optically excite HfS$_2$. This creates an excess of free carriers which are transferred to oxygen producing a radical ion (O$_2{}^-$). Subsequently this reacts with HfS$_2$, cleaving the Hf-S bond and producing HfO$_2$ and SO$_2$. The full reaction can be expressed as:

$$\text{HfS}_2(s) + 3\text{O}_2(aq) + h\nu \rightarrow \text{HfO}_2(s) + 2\text{SO}_2(g) \tag{5.1}$$
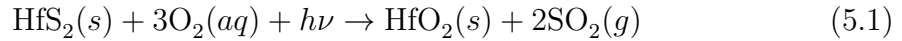
where s, aq, and g indicate the phase of the reactant or product (solid, aqueous, or gaseous respectively). It is important to note that the photo-oxidation process relies on the band alignment of the material with redox potentials. Therefore only certain 2D materials are susceptible.[16]

HfS$_2$ is a layered semiconducting material with an indirect band gap of $E_g \sim$ 1.2 eV. The direct gap is located at the Brillouin zone centre (Γ), see Figure 5.1b. Following oxidation the band gap is increased to $E_g \sim 4$ eV indicating the creation of an insulating material. Interestingly oxidation has been shown to occur even whilst HfS$_2$ is embedded in complex heterostructures and under metal electrodes. This allows the integration of high-k dielectrics into electronic devices based on 2D materials without the need for invasive and destructive sputtering methods. In an accompanying work HfO$_x$-based heterostructure devices are currently being investigated as flexible FETs as well as resistive switching memories. It has been demonstrated that photo-induced HfO$_x$ has a dielectric constant of $k \sim 15$.[17]
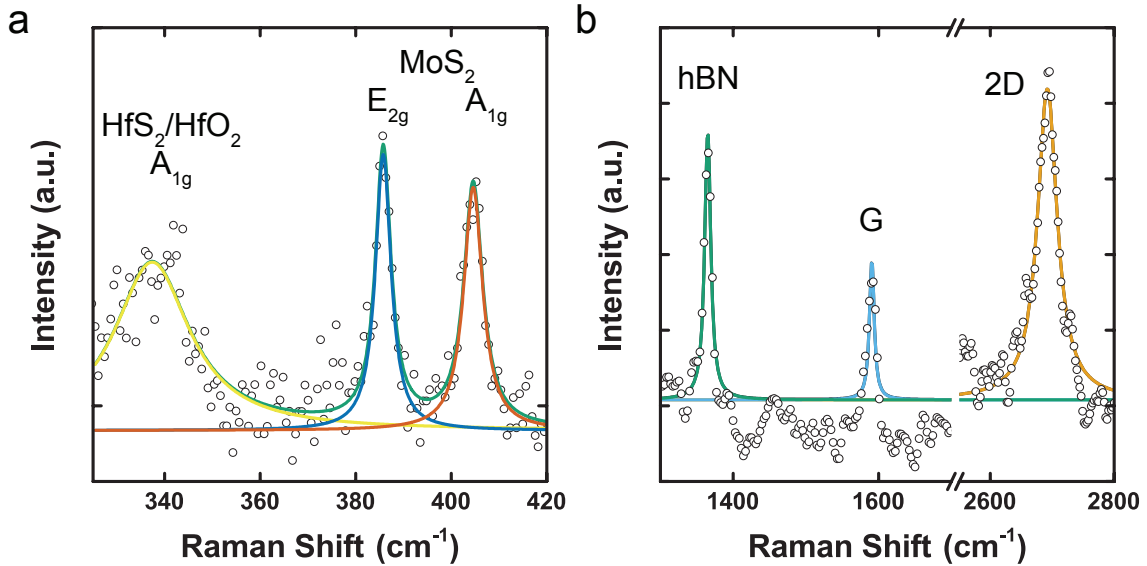
Figure 5.3: **Raman spectra of heterostructure** (a) Low frequency region of spectrum with MoS_2 and HfS_2 modes visible. (b) High frequency region showing hBN and graphene modes. Lorentzian fits have been used to identify peaks and the background MoS_2 PL has been subtracted. The peak around $1450\,cm^{-1}$ is believed to be an artefact from the background subtraction process. Note the absence of the graphene D peak around $1350\,cm^{-1}$ indicates that there is no laser induced disorder from the oxidation process.

5.3 Device Fabrication

Figure 5.2a shows an optical micrograph of the HfO_x vertical tunnelling device. This heterostructure has been assembled by the dry transfer of 2D flakes, as detailed in Chapter 3. Here a few-layer flake of HfS_2 (1-2 nm) has been placed in the stack where a dielectric material is required. Following van der Waals assembly the contacts are defined by electron beam lithography and thermal evaporation of Cr/Au (5/60 nm). Photo-oxidation of the HfS_2 layer was performed in atmospheric conditions by rastering either UV ($\lambda = 375\,nm$) or visible ($\lambda = 473\,nm$) laser light focused to a diffraction-limited spot in a custom-built set-up.[18] A typical power density of $53\,mW\,\mu m^{-2}$ was used for exposures lasting 1-2 seconds per point, depending on the thickness of the HfS_2 layer. Following oxidation all measurements were performed under a vacuum of $10^{-5}\,mBar$ or less. The focused spot-size was $d_s = 264\,nm$ for the UV laser and $d_s = 445\,nm$ for the visible wavelength. For Raman, photoluminesence and other optoelectronic measurements another visible wavelength laser was used ($\lambda = 514\,nm, d_s = 484\,nm$) The heterostructure layer sequence and band structure is shown in Figure 5.2b. hBN is used as an atomically flat substrate on to which the subsequent flakes can be assembled. Monolayer MoS_2 is embedded within two layers of HfO_x with monolayer graphene used as top and bottom electrodes. The separation between electrodes is therefore between 3 and 5 nm.

Raman spectroscopy is used to non-destructively probe the heterostructure de-
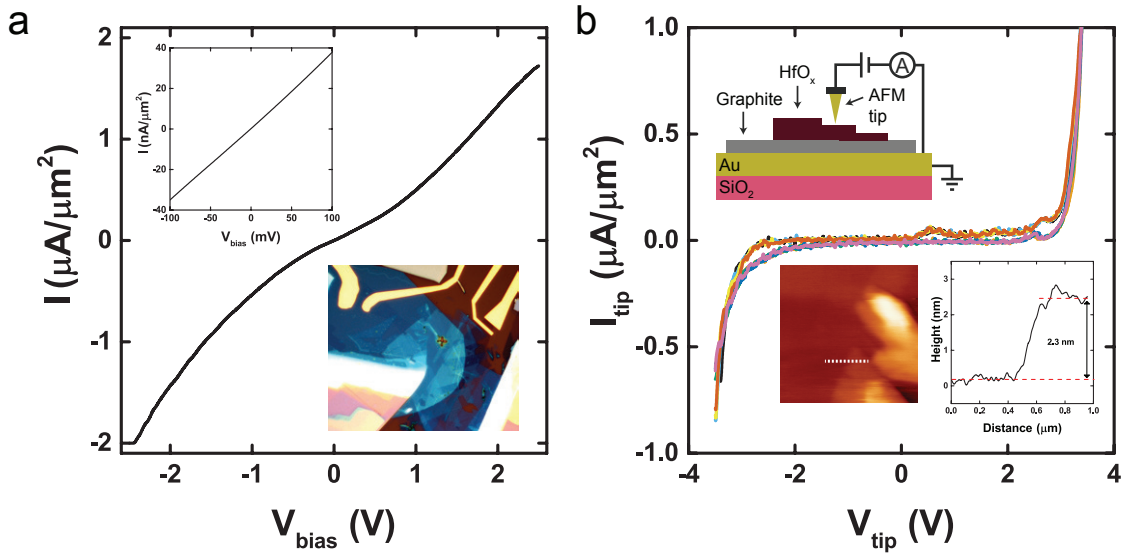
Figure 5.4: **Tunnel current** (a) IV curve for the heterostructure device. Insets show zoom of low bias region (top) and optical image (bottom). (b) IV curve of HfO_x using CAFM. Insets show schematic of CAFM setup (top) and topographical map with line scan (bottom).

vice and verify the material composition. Figure 5.3a shows the low frequency $(320 - 420\,cm^{-1})$ region of the Raman spectra. Multiple peaks can be identified using Lorentzian fits and assigned to different materials by comparison with literature reports. The two peaks at $385\,cm^{-1}$ and $404\,cm^{-1}$ are the E_{2g} and A_{1g} modes of MoS_2 respectively.[19] Whilst the peak around $337\,cm^{-1}$ corresponds to the A_{1g} mode of HfS_2, the contribution from the phonon modes of HfO_2 cannot be ruled out.[20–22] Indeed a previous work has shown that the intensity of this peak decreases upon oxidation.[14] In the higher-frequency region $(1300-2800\,cm^{-1})$ three peaks are identified which originate from phonons present in hBN $(1380\,cm^{-1})$ as well as the G and 2D Raman modes of graphene $(1591\,cm^{-1}$ and $2693\,cm^{-1})$, Figure 5.3.[23,24] The negligible D-peak $(1350\,cm^{-1}$ for $\lambda = 514\,nm)$[25] seen after oxidation indicates that graphene is not significantly damaged by the laser oxidation process.

5.4   Tunnelling behaviour

Figure 5.4a shows a current-voltage curve of a HfO_x encapsulated MoS_2 in 1-2 nm of HfO_x. Upon applying a bias voltage between the top and bottom graphene electrodes (G_t and G_b) a tunnel current through the thin HfO_x layers and into the MoS_2 is observed. As the bias voltage is increased from zero the current increases non-linearly. Outside of a low-bias regime ($|V_{sd}| > 1\,V$) an increase in the current is observed due to tunnelling into the conduction band of MoS_2. In addition, an asymmetry between the current at positive and negative bias voltage is observed which is likely due to both a variation in doping between G_t and G_b and a different thickness of the top and bottom HfO_x. A low-bias resistance of $2.7 \times 10^6\,\Omega\,\mu m^2$
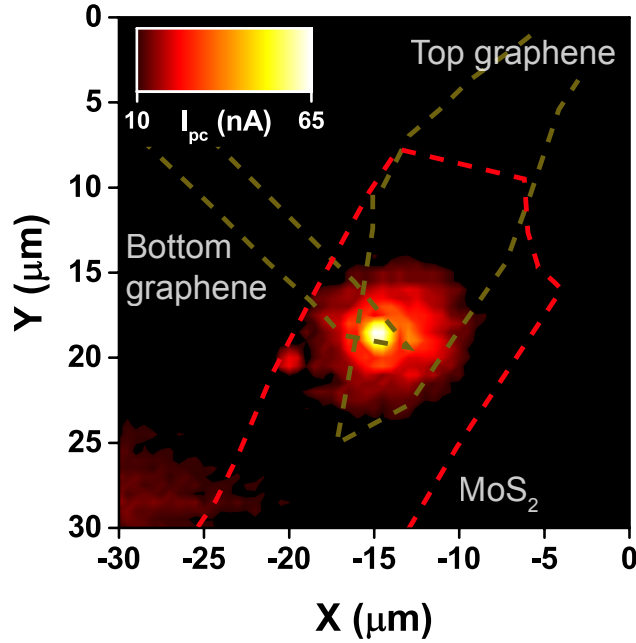
Figure 5.5: **Scanning photocurrent microscopy** Scanning photocurrent map acquired with a bias of V_{bias} = -1 V applied between the top and bottom graphene (outlined in green). Monolayer MoS$_2$ is outlined in red. A power density of $P = 270\,\mu\text{W}\,\mu\text{m}^{-2}$ was used ($\lambda = 514\,\text{nm}$).

is comparable to previous reports of hBN tunnel barriers of similar thickness ($\sim$ 1 nm).[7,26] Conductive AFM (CAFM) was used to locally probe the tunnelling current through ultra-thin HfO$_x$. A voltage was applied to the graphite/Au substrate and the current measured using a conductive tip (diamond like carbon) connected to a Femto DLPCA current amplifier and voltmeter. Figure 5.4b shows multiple I-V curves for a 2.3 nm thick flake of HfO$_x$. The thicker flake used here shows insulating behaviour at low bias and a sharp onset of conductance at higher biases due to the onset of dielectric breakdown ($E_{BD} \sim 0.7\,\text{V}\,\text{nm}^{-1}$). This behaviour is similar to a CAFM study of ultra-thin hBN flakes.[27] Topographical image analysis and height profile extraction were performed with WSxM v4.0 software.[28]

5.5 Photodetection

To determine the active area of the heterostructure scanning photocurrent microscopy (SPCM) was used whereby a laser beam is rastered across the device whilst photocurrent is acquired simultaneously. These measurements were performed using a continuous wave laser ($\lambda = 514\,\text{nm}, P = 50\,\mu\text{W}$). The electrical signal was acquired by a DL Instruments model 1211 current amplifier connected to a Signal Recovery model 7124 digital signal processing lock-in amplifier. The frequency of modulation of the lasers was 73.87 Hz. Figure 5.5 shows that under a moderate bias ($V_{bias} = -1\,\text{V}$) the photocurrent is predominately localized to regions of overlap
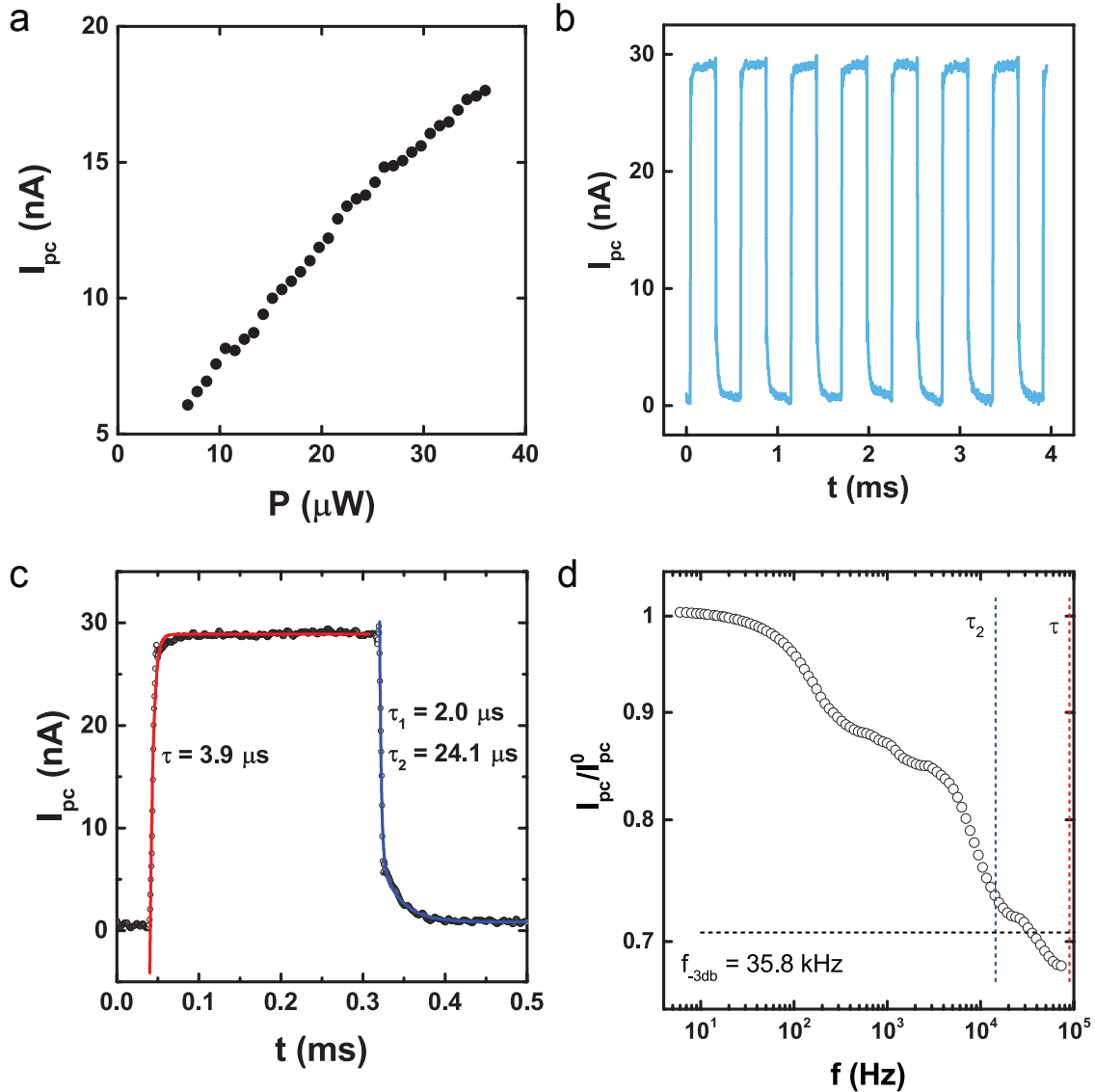
Figure 5.6: **Photodetector performance** (a) Power dependence of the generated photocurrent recorded at V_{bias} = -1 V. (b) Temporal response of the photocurrent at $f = 1.8$ kHz (c) Single oscillation of the photo-current. The rise (fall) times have been extracted by fitting the data, black circles, using exponential decays with one (two) time constants. (d) Normalised photocurrent as a function of modulation frequency. Black dashed line highlights -3 dB frequency ($I_{pc}/I_{pc}^0 \sim 0.707$) whilst red and blue dashed lines are calculated from the time constants in (c).

between the top and bottom graphene flakes, each outlined in light green. Photoexcited carriers in MoS_2 (red outline) are separated by the graphene electrodes due to the applied vertical electric field. Away from this region the photocurrent (I_{pc}) drops from > 65 nA to < 10 nA.

In Figure 5.6a the power dependence of the photocurrent is shown. This localised photocurrent (I_{pc}) has a non-linear power dependence which has been previously attributed to absorption saturation or electric field screening by the photoexcited carriers in MoS_2.[29] An external quantum efficiency (EQE) of ($\eta = (I_{pc}/q)(h\nu/P) \sim 0.002\%$) is observed which is smaller than previous works[29] which is anticipated due to the low absorption of monolayer MoS_2 ($\sim 2.5\%$ at $\lambda = 514$ nm),[30] the increased confinement of charges in the HfO_x QW, and off-resonance excitation. Figure 5.6b shows multiple iterations of the photocurrent obtained at 1.8 kHz. Fitting a single iteration with exponential functions allows the rise and fall times to be extracted which are on µs time-scales, Figure 5.6c. In Figure 5.6d a reduction in the magnitude of the photocurrent is measured whilst the light modulation frequency is increased. By normalizing this to the value of the photocurrent at low frequencies I_{pc}^0 the -3dB bandwidth of the device can be ascertained, which is found to be $f_{-3dB} = 35.8$ kHz. From this we can estimate the rise time using $t_r = 0.35/f_{-3dB} \sim 10$ µs which is in good agreement with our analysis of the temporal response of the photocurrent. The low EQE suggests that there is no significant gain mechanism present in our device which corroborates with the rise and fall time analysis. As the time constants are similar in magnitude it is unlikely that either results from long lived charge trapping – a common mechanism for photoconductive gain. As a result, this conclusion supports the claim of the formation of a clean oxide with few impurity states, crucial for the creation of a tunnelling transistor. The measured response time is $10^3 - 10^6$ times faster than typical planar MoS_2 photodetectors,[31] a result arising from the use of a vertical, as opposed to lateral, contact geometry. The small electrode separation 3-5 nm and large electric fields $\sim 0.2 - 0.3$ V/nm minimize the transit time of the photoexcited carriers. Hence, these vertical heterostructures of MoS_2 encapsulated in HfO_x are a promising high-speed light-detection architecture.

5.6 Light-emission

Monolayer MoS_2 has a direct band gap which favours the radiative recombination of excited charges. Figure 5.7a shows the photoluminescence (PL) spectrum of the heterostructure for $V_{bias} = 0$ V. By fitting the data with Lorentzian fits two peaks are identified corresponding to the A (1.84 eV) and B (2.00 eV) exciton transitions between the conduction and valence bands. The spin-orbit coupling induced splitting (E_{SO}) of the valence band can be estimated from the difference in the energies of
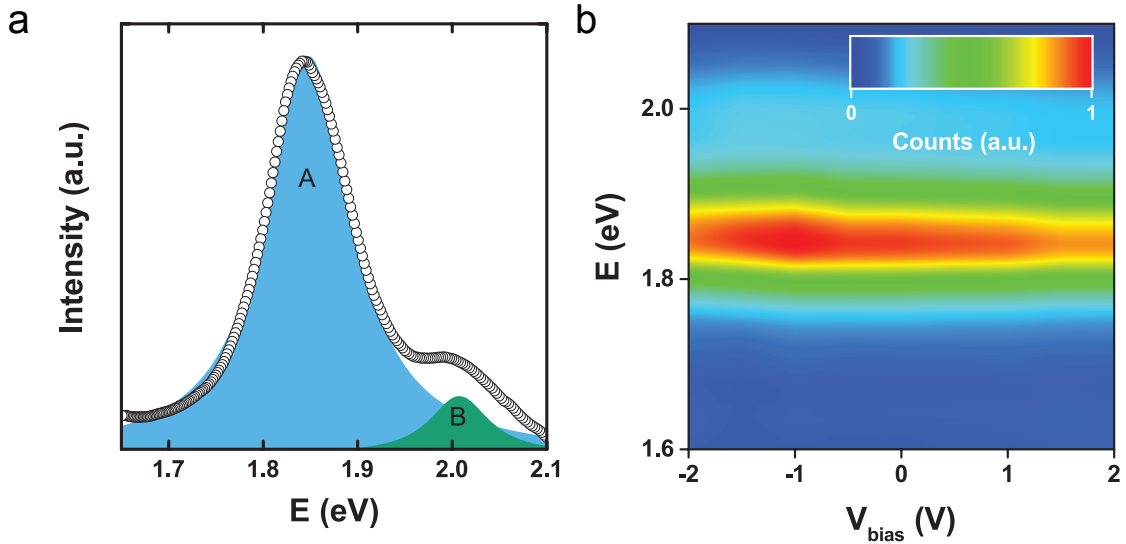
Figure 5.7: **Photoluminescence** (a) PL spectrum of heterostructure for $V_{bias} = 0$ V. (b) Colour map of emission energy against applied bias (V).

the A and B excitons:

$$E_{SO} = E_B - E_A. \tag{5.2}$$

From this E_{SO} is calculated to be 160 meV which is in excellent agreement with other reports.[32]

Figure 5.7b shows the bias dependence of the PL. For positive bias voltages the PL intensity decreases to a minimum at 2 V. As the bias is increased the Fermi level of the bottom graphene electrode aligns with the conduction band of MoS_2 favouring the extraction of photoexcited carriers, preventing their recombination and therefore quenching the PL. Similarly, as the bias is swept to negative values a peak in PL intensity is observed followed by a decrease with the peak located away from zero. This is likely due to asymmetry in the thickness of the two barriers and the doping of top and bottom graphene.

Upon increasing the bias to more negative values ($V < -2$ V) and switching the laser off the onset of electroluminescence (EL) is observed, Figure 5.8a. This is due to the injection of holes into the valence band of MoS_2 as we exceed the single particle band gap. To further understand the emission, normalized EL and photoluminescence (PL) spectra are shown in Figure 5.8b. The main PL emission peak is assigned to the A exciton seen at an energy of 1.84 eV. The energy of the main EL band red-shifts from that of PL by 53 meV. Typically, the exfoliated monolayer MoS_2 is n-doped, which favours the formation of negatively-charged excitons,[33] which have a lower emission energy than that of the neutral exciton by ~ 30 meV. Therefore the main feature in the electroluminescence spectra at 1.78 eV is attributed to the radiative recombination of the charged exciton. Moreover the dissociation energy (i.e. energy shift with respect to that of the neutral exciton) of charged exciton is proportional to the doping concentration.[33] Therefore it is likely the large energy
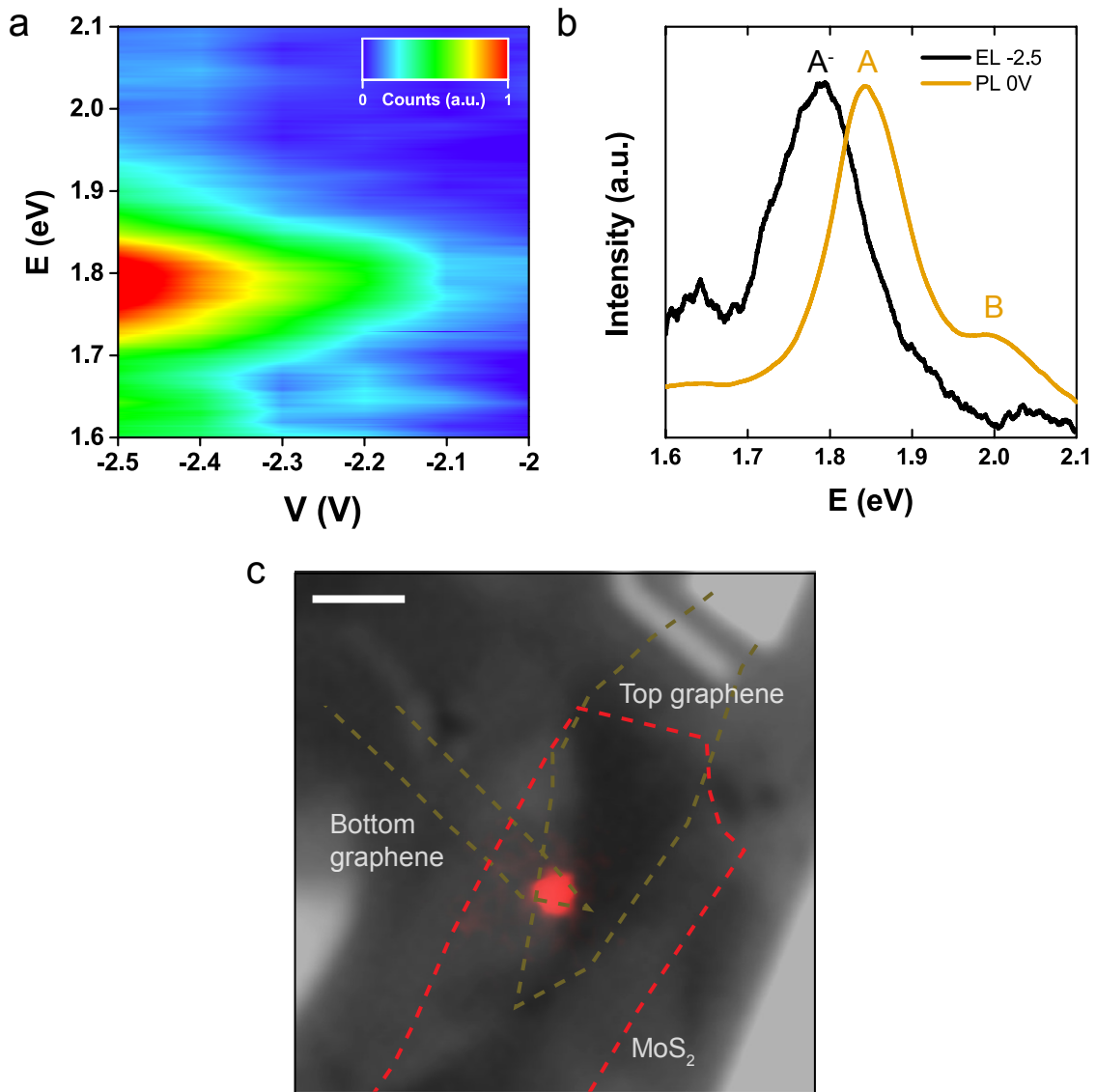
Figure 5.8: **Electroluminesence** (a) Colour map of emission energy against applied bias (V). (b) Comparison between PL and EL spectra of MoS_2. (c) False-colour CCD image of the EL overlaid on an optical image of the device (Scale bar = 5 μm).

difference between electroluminescence and photoluminescence is an indication of high doping in monolayer MoS_2, which is due to doping of the as-exfoliated natural MoS_2 flakes and extra charge transfer from HfO_x. Finally the spatial location of the EL is determined. Figure 5.8c shows a false-colour CCD image of the EL overlaid on a monochrome image of the device at applied bias voltage of -2.5 V. The EL is localized to the active area of the device previously identified in Figure 5.5 through photo-current mapping highlighting the multi-functionality of the device. Therefore both light-detection and light-emission is achieved within the same architecture.

5.7 Summary and outlook

In conclusion this chapter has investigated the use of laser-oxidised HfO_x as a tunnel barrier in multifunctional optoelectronic devices. HfS_2 can be embedded in

complex van der Waals heterostructures and selectively oxidised without damaging the underlying 2D materials. The ultra-thin oxide has a breakdown voltage of $E_{BD} \sim 0.7\,\mathrm{V\,nm^{-1}}$ and a low bias resistance of $2.7 \times 10^6\,\Omega\,\mathrm{\mu m^{-2}}$. These favourable properties allow the creation of a tunnelling transistor when used as a barrier between graphene and MoS_2. Such structures have been shown to be capable of both light emission and detection in the same device with EL intensities and drive voltages comparable to devices based on hBN. Additionally the photodetection response times are 10^6 faster than equivalent planar MoS_2 devices. Furthermore the high-k dielectric constant, compatibility with 2D materials and ease of laser-writing techniques will facilitate the down-scaling of electronic devices and offer greater device functionality. Future research should focus on increasing the quantum efficiency both of photodetection and electroluminescence. This could be achieved by stacking multiple HfO_x encapsulated monolayers or by replacing monolayer MoS_2 with a multilayer direct band gap material.

References

[1] Michal J. Mleczko, Chaofan Zhang, Hye Ryoung Lee, Hsueh-Hui Kuo, Blanka Magyari-Köpe, Robert G. Moore, Zhi-Xun Shen, Ian R. Fisher, Yoshio Nishi, and Eric Pop. HfSe 2 and ZrSe 2 : Two-dimensional semiconductors with native high-κ oxides. *Science Advances*, 3(8):e1700481, aug 2017.

[2] Bhim Chamlagain, Qingsong Cui, Sagar Paudel, Mark Ming-cheng Cheng, Pai-yen Chen, and Zhixian Zhou. Thermally oxidized 2D TaS 2 as a high- κ gate dielectric for MoS 2 field-effect transistors. *2D Materials*, 4(3):031002, jun 2017.

[3] Santiago J. Cartamil-Bueno, Peter G. Steeneken, Frans D. Tichelaar, Efren Navarro-Moratalla, Warner J. Venstra, Ronald van Leeuwen, Eugenio Coronado, Herre S. J. van der Zant, Gary A. Steele, and Andres Castellanos-Gomez. High-quality-factor tantalum oxide nanomechanical resonators by laser oxidation of TaSe2. *Nano Research*, 8(9):2842–2849, sep 2015.

[4] L Britnell, R M Ribeiro, A Eckmann, R Jalil, B D Belle, A Mishchenko, Y Kim, R V Gorbachev, T Georgiou, S V Morozov, A N Grigorenko, A K Geim, C Casiraghi, A H Castro Neto, and K S Novoselov. Strong Light-Matter Interactions in heterostructures of atomically Thin Films. *Science*, 340(6238):1331–1314, jun 2013.

[5] Marco M. Furchi, Andreas Pospischil, Florian Libisch, Joachim Burgdörfer, and Thomas Mueller. Photovoltaic Effect in an Electrically Tunable van der Waals Heterojunction. *Nano Letters*, 14(8):4785–4791, aug 2014.

[6] M Massicotte, P Schmidt, F Vialla, K G Schädler, a Reserbat-Plantey, K Watanabe, T Taniguchi, K J Tielrooij, and F H L Koppens. Picosecond photoresponse in van der Waals heterostructures. *Nature nanotechnology*, 11(October):1–6, 2015.

[7] F. Withers, O. Del Pozo-Zamudio, A. Mishchenko, A. P. Rooney, A. Gholinia, K. Watanabe, T. Taniguchi, S. J. Haigh, A. K. Geim, A. I. Tartakovskii, and K. S. Novoselov. Light-emitting diodes by band-structure engineering in van der Waals heterostructures. *Nature Materials*, 14(3):301–306, feb 2015.

[8] F. Withers, O. Del Pozo-Zamudio, S. Schwarz, S. Dufferwiel, P. M. Walker, T. Godde, A. P. Rooney, A. Gholinia, C. R. Woods, P. Blake, S. J. Haigh, K. Watanabe, T. Taniguchi, I. L. Aleiner, A. K. Geim, V. I. Fal'ko, A. I. Tartakovskii, and K. S. Novoselov. WSe 2 Light-Emitting Tunneling Transistors with Enhanced Brightness at Room Temperature. *Nano Letters*, 15(12):8223–8228, dec 2015.

[9] Johannes Binder, Freddie Withers, Maciej R. Molas, Clement Faugeras, Karol Nogajewski, Kenji Watanabe, Takashi Taniguchi, Aleksey Kozikov, Andre K. Geim, Kostya S. Novoselov, and Marek Potemski. Sub-bandgap Voltage Electroluminescence and Magneto-oscillations in a WSe 2 Light-Emitting van der Waals Heterostructure. *Nano Letters*, 17(3):1425–1430, mar 2017.

[10] Adrianus I. Aria, Kenichi Nakanishi, Long Xiao, Philipp Braeuninger-Weimer, Abhay A. Sagade, Jack A. Alexander-Webber, and Stephan Hofmann. Parameter Space of Atomic Layer Deposition of Ultrathin Oxides on Graphene. *ACS Applied Materials & Interfaces*, 8(44):30564–30575, nov 2016.

[11] Hyun Gu Kim and Han-Bo-Ram Lee. Atomic Layer Deposition on 2D Materials. *Chemistry of Materials*, 29(9):3809–3826, may 2017.

[12] Yuan Liu, Jian Guo, Enbo Zhu, Lei Liao, Sung-joon Lee, Mengning Ding, Imran Shakir, Vincent Gambin, Yu Huang, and Xiangfeng Duan. Waals metal – semiconductor junctions. *Nature*, 2018.

[13] A. V. Kretinin, Y. Cao, J. S. Tu, G. L. Yu, R. Jalil, K. S. Novoselov, S. J. Haigh, A. Gholinia, A. Mishchenko, M. Lozada, T. Georgiou, C. R. Woods, F. Withers, P. Blake, G. Eda, A. Wirsig, C. Hucho, K. Watanabe, T. Taniguchi, A. K. Geim, and R. V. Gorbachev. Electronic properties of graphene encapsulated with different two-dimensional atomic crystals. *Nano Letters*, 14(6):3270–3276, 2014.

[14] Adolfo De Sanctis, Iddo Amit, Steven P. Hepplestone, Monica F. Craciun, and Saverio Russo. Strain-engineered inverse charge-funnelling in layered semiconductors. *Nature Communications*, 9(1):1652, dec 2018.

[15] Alexandre Favron, Etienne Gaufrès, Frédéric Fossard, Anne-Laurence Phaneuf-L'Heureux, Nathalie Y-W. Tang, Pierre L. Lévesque, Annick Loiseau, Richard Leonelli, Sébastien Francoeur, and Richard Martel. Photooxidation and quantum confinement effects in exfoliated black phosphorus. *Nature Materials*, 14(8):826–832, aug 2015.

[16] Filip A. Rasmussen and Kristian S. Thygesen. Computational 2D Materials Database: Electronic Structure of Transition-Metal Dichalcogenides and Oxides. *Journal of Physical Chemistry C*, 119(23):13169–13183, 2015.

[17] Namphung Peimyoo, Jake Mehew, Matt D. Barnes, Adolfo De Sanctis, Iddo Amit, Janire Escolar, Konstantinos Anastasiou, Ali Gholina, Aidan P Rooney, Sarah Haigh, Saverio Russo, Monica F. Craciun, and Freddie Withers. Photo-oxidized HfS2 - An embeddable and writable high-k dielectric for flexible Van der Waals nano-electronics. In *2018 76th Device Research Conference (DRC)*, pages 1–2. IEEE, jun 2018.

[18] Adolfo De Sanctis, Gareth F. Jones, Nicola J. Townsend, Monica F. Craciun, and Saverio Russo. An integrated and multi-purpose microscope for the characterization of atomically thin optoelectronic devices. *Review of Scientific Instruments*, 88(5):055102, may 2017.

[19] J. L. Verble and T. J. Wieting. Lattice mode degeneracy in MoS2 and other layer compounds. *Physical Review Letters*, 25(6):362–365, 1970.

[20] Roubi and Carlone. Resonance Raman spectrum of HfS2 and ZrS2. *Physical review. B, Condensed matter*, 37(12):6808–6812, apr 1988.

[21] A Cingolani, M Lugarà, and F Lévy. Resonance Raman scattering in HfSe 2 and HfS 2. *Physica Scripta*, 37(3):389–391, mar 1988.

[22] Xinyuan Zhao and David Vanderbilt. First-principles study of structural, vibrational, and lattice dielectric properties of hafnium oxide. *Physical Review B*, 65(23):233106, jun 2002.

[23] Roman V. Gorbachev, Ibtsam Riaz, Rahul R. Nair, Rashid Jalil, Liam Britnell, Branson D. Belle, Ernie W. Hill, Kostya S. Novoselov, Kenji Watanabe, Takashi Taniguchi, Andre K. Geim, and Peter Blake. Hunting for Monolayer Boron Nitride: Optical and Raman Signatures. *Small*, 7(4):465–468, feb 2011.

[24] Andrea C. Ferrari and Denis M. Basko. Raman spectroscopy as a versatile tool for studying the properties of graphene. *Nature Nanotechnology*, 8(4):235–246, apr 2013.

[25] Andrea C. Ferrari. Raman spectroscopy of graphene and graphite: Disorder, electron-phonon coupling, doping and nonadiabatic effects. *Solid State Communications*, 143(1-2):47–57, jul 2007.

[26] Liam Britnell, Roman V. Gorbachev, Rashid Jalil, Branson D. Belle, Fred Schedin, Mikhail I. Katsnelson, Laurence Eaves, Sergey V. Morozov, Alexander S. Mayorov, Nuno M. R. Peres, Antonio H. Castro Neto, Jon Leist, Andre K. Geim, Leonid A. Ponomarenko, and Kostya S. Novoselov. Electron Tunneling through Ultrathin Boron Nitride Crystalline Barriers. *Nano Letters*, 12(3):1707–1710, mar 2012.

[27] Gwan Hyoung Lee, Young Jun Yu, Changgu Lee, Cory Dean, Kenneth L. Shepard, Philip Kim, and James Hone. Electron tunneling through atomically flat and ultrathin hexagonal boron nitride. *Applied Physics Letters*, 99(24):1–4, 2011.

[28] I. Horcas, R. Fernández, J. M. Gómez-Rodríguez, J. Colchero, J. Gómez-Herrero, and A. M. Baro. WSXM : A software for scanning probe microscopy and a tool for nanotechnology. *Review of Scientific Instruments*, 78(1):013705, jan 2007.

[29] Woo Jong Yu, Yuan Liu, Hailong Zhou, Anxiang Yin, Zheng Li, Yu Huang, and Xiangfeng Duan. Highly efficient gate-tunable photocurrent generation in vertical heterostructures of layered materials. *Nature Nanotechnology*, 8(12):952–958, dec 2013.

[30] Andres Castellanos-Gomez, Jorge Quereda, Herko P van der Meulen, Nicolás Agraït, and Gabino Rubio-Bollinger. Spatially resolved optical absorption spectroscopy of single- and few-layer MoS2 by hyperspectral imaging. *Nanotechnology*, 27(11):115705, mar 2016.

[31] Dominik Kufer and Gerasimos Konstantatos. Highly Sensitive, Encapsulated MoS2 Photodetector with Gate Controllable Gain and Speed. *Nano Letters*, 15(11):7307–7313, 2015.

[32] Andrea Splendiani, Liang Sun, Yuanbo Zhang, Tianshu Li, Jonghwan Kim, Chi Yung Chim, Giulia Galli, and Feng Wang. Emerging photoluminescence in monolayer MoS2. *Nano Letters*, 10(4):1271–1275, 2010.

[33] Kin Fai Mak, Keliang He, Changgu Lee, Gwan Hyoung Lee, James Hone, Tony F. Heinz, and Jie Shan. Tightly bound trions in monolayer MoS2. *Nature Materials*, 12(3):207–211, mar 2013.

<div style="text-align: right; font-size: 3em;">*6*</div>

Modifying the twist-angle in graphene/hBN superlattice devices using contact-induced strain

NOTE: The ideas and data presented in this Chapter have been the subject of the following publication: *Strain-Engineering of Twist-Angle in Graphene/hBN Superlattice Devices.* Nano Letters 18, 7919 (2018). Adolfo De Sanctis, **Jake D. Mehew**, Saad Alkhalifa, Freddie Withers, Monica F. Craciun, and Saverio Russo.

J. D. Mehew fabricated all the devices, participated in data analysis & interpretation and wrote the manuscript associated with this chapter which is currently in preparation for submission.

6.1   Introduction

The fabrication of high-mobility graphene devices has benefited from two major breakthroughs. Hexagonal boron nitride (hBN) was introduced as a substrate for graphene replacing the commonly used SiO_2. This 2D dielectric ($E_g \sim 6\,\text{eV}$) is free from dangling bonds and is lattice matched to graphene within $\delta \sim 1.8\%$ allowing for an atomically clean interface to be formed. The van der Waals attraction between these 2D materials is strong enough to push contamination outside of the overlap region - an atomic-scale self cleaning mechanism.[1] Furthermore hBN surface optical phonons are at energies two times larger than similar modes in SiO_2.[2] These favourable conditions increase the mobility of graphene devices on hBN by an order of magnitude compared with SiO_2.[2] The second major development in graphene devices was the realization of high-quality electrical contacts to graphene fully encapsulated in hBN.[3] Reactive ion etching of the hBN/graphene/hBN heterostructure allows the metallization of only the 1D edge of a graphene layer. In these edge-contact geometries low temperature ballistic transport was reported over $15\,\mu\text{m}$ and room temperature mobilities became comparable with the phonon scattering limit.[3]

Moiré interference patterns are observed for graphene on hBN owing to similarities between their lattices. The rotation of graphene with respect to the underlying hBN produces patterns each with a different Moiré wavelength,[4,5] suggesting that effective periodic potentials are formed. Figure 6.1a shows the Moiré pattern for

<div style="text-align: center;">79</div>
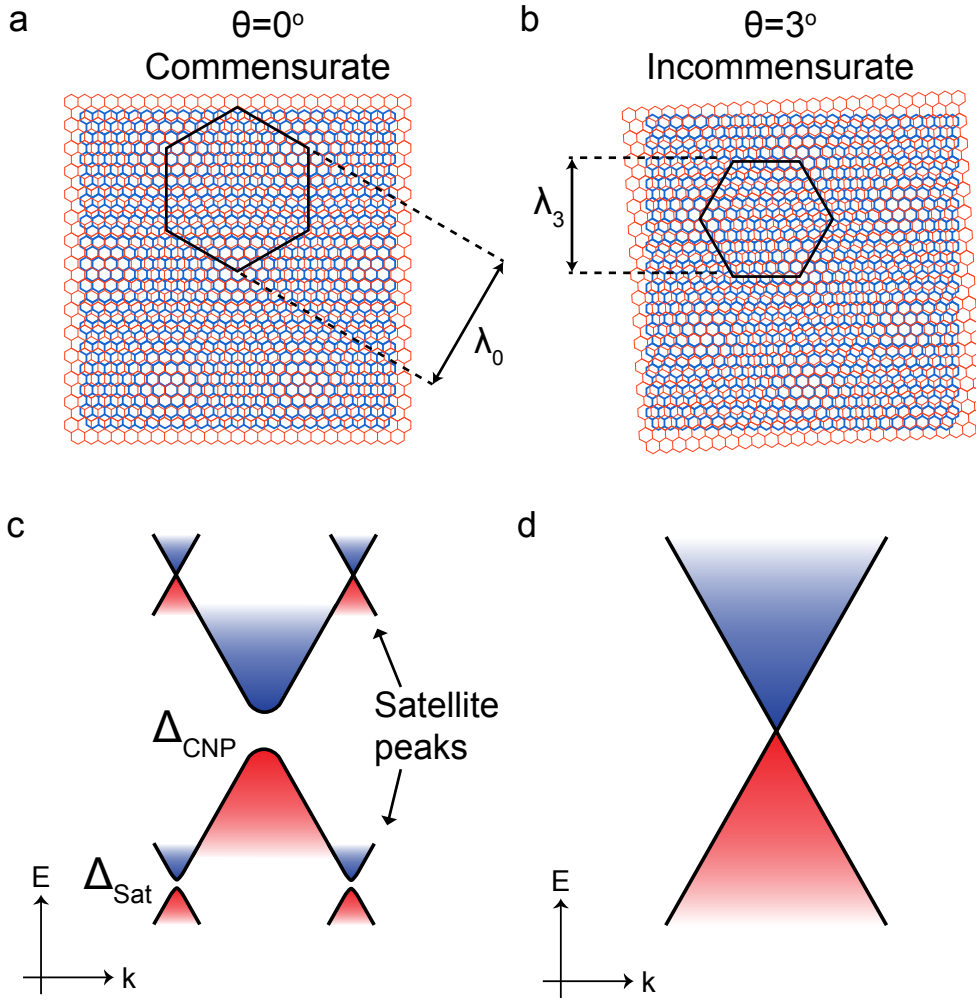
Figure 6.1: **Schematic of the moiré pattern of graphene (red) on hBN (blue) and heterostructure band structure.** Twist angle between the crystals for the commensurate (a) and incommensurate (b) states. Black hexagons outline the Moiré plaquette of wavelength λ. The lattice mismatch has been exaggerated to illustrate the Moiré pattern (10 %). Schematic band structure of graphene-hBN heterostructure (c) and pristine graphene (d). In the graphene-hBN heterostructure both the charge neutrality point (Δ_{CNP}) and satellite peaks (Δ_{Sat}) can have an energy gap.

the case in which graphene and hBN are perfectly aligned (twist angle $\theta = 0°$). The relationship between twist angle (θ) and Moiré wavelength (λ) is:[6,7]

$$\lambda = \frac{(1 + \delta) \, a}{\sqrt{2 \, (1 + \delta) \, [1 - \cos \theta] + \delta^2}}, \qquad (6.1)$$

where $\delta \sim 0.017$ is the lattice mismatch between graphene/hBN and $a = 0.246\,\mathrm{nm}$ the lattice constant of graphene. With increasing twist angle the Moiré wavelength reduces, Figure 6.1b. For massless Dirac fermions this results in the formation of new Dirac points in the electronic band structure whose energy and wavevector is determined by the Moiré wavelength, Figure 6.1c.[6] Furthermore energy gaps open at the charge neutrality point (Δ_{CNP}) and at the satellite peaks (Δ_{Sat}) located in the

valence band. The asymmetry between satellite peaks in the conduction and valence bands comes from the asymmetry in the on-site energies in hBN and next-nearest neighbour interlayer hopping.[6] For large twist angles the band structure approaches that of pristine graphene, Figure 6.1d.

Super-lattice structures have led to observation of several physical phenomena including Hofstadter's butterfly,[8–10] topological supercurrents,[11] and even unconventional superconductivity.[12] Critical to these observations is the formation of a commensurate state in which graphene is locally stretched in domains separated by sharp domain walls. Previous works have reported that a commensurate-incommensurate transition occurs at twist angles $\theta \sim 1°$.[13] For small angles (large $\lambda > 10\,\text{nm}$) graphene forms these domains of strong van der Waals interaction with hBN. For the case with large angles local strain is not observed and the system is in an incommensurate state, Figure 6.1b. Thermal annealing has been shown to induce an incommensurate-commensurate transition providing the initial twist angle is small ($\theta \leq 2°$).[14] For flakes which do not align, a 1D network of wrinkles emerge.[14] This is proposed to arise from the difference in thermal expansion coefficients between hBN and graphene.

It is known that the deposition of metal contacts onto graphene induces structural defects, doping and strain.[15] However the effect that this has on graphene/hBN super-lattice structures is at present unknown. This chapter will attempt to address this shortcoming. Aligned graphene/hBN heterostructures with both 2D (top) and 1D (edge) contacts have been fabricated and characterised using Raman spectroscopy and electrical transport measurements.

6.2   Fabrication

hBN was mechanically exfoliated onto SiO_2/Si^+ substrates that had been previously treated with a high power oxygen plasma (30 W). This processing step increases both the yield and lateral size of exfoliated flakes.[16] Graphene was exfoliated onto a polymer bilayer (PMMA/PVA) and placed on the hBN by the dry transfer technique, detailed in depth in Chapter 2. Care was taken to minimise the twist angle by aligning the crystallographic edges of graphene and hBN. Figure 6.2a shows the lithography steps that follow. Graphene on hBN (i) is etched into Hall bar geometry using an Ar/O_2 plasma (ii). Deposition of metal electrodes followed one of two routes: A or B. In route A the top contacts are formed first by electron beam lithography and thermal evaporation of Cr/Au (15/60 nm) electrodes (iii). For edge contacts the graphene/hBN heterostructure is etched in an CHF_3/O_2 plasma (iv) before metal deposition (v). Optical images of each stage of fabrication are shown in Figure 6.2b. Route B differs in that the edge contacts are processed before the top contacts. In the following sections the results obtained are independent of the
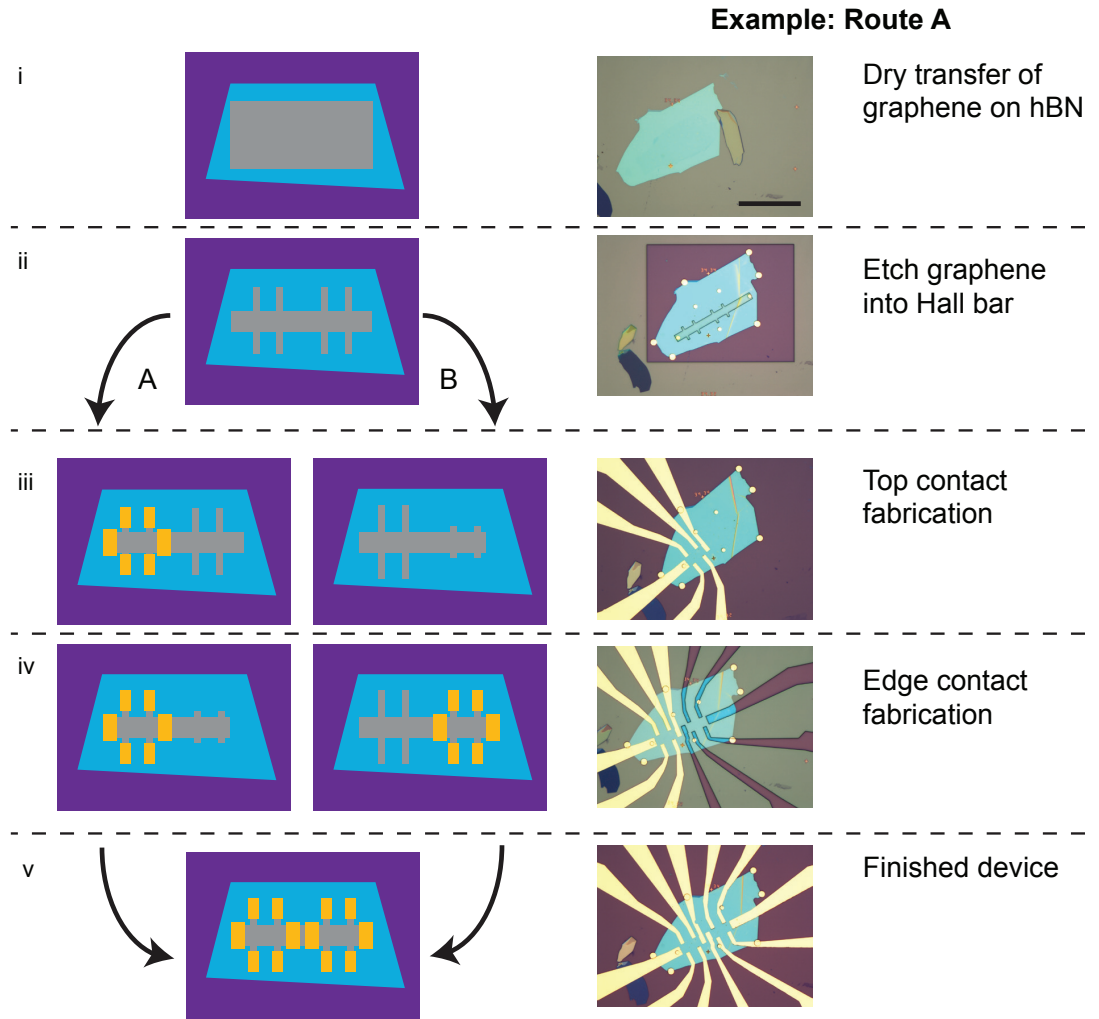
Figure 6.2: **Top and edge contact fabrication** Sequence (i-v) of fabrication steps (see main text) with schematic (left) and optical image (right). In route A (B) the top (edge) contact fabrication step comes first. Both routes yield the same outcome.

processing route taken.

In Figure 6.3a a 3D illustration of the device is shown. In particular the difference between edge and top contacts becomes clear. Edge electrodes make contact along a 1D chain of carbon atoms due to the etching step immediately before metal evaporation. On the other hand top electrodes overlap with the graphene flake.

6.3   Raman analysis

Given the dissimilarity between the top and edge contacts it is not surprising that the Raman specta acquired in their proximity is different, Figure 6.3b. Here multiple peaks are observed corresponding to the E_{2g} phonon mode of hBN and the G ($\sim$ 1580 cm^{-1}) and $2D$ ($\sim$ 2670 cm^{-1}) modes of graphene. Both the G and $2D$ modes are up-shifted for edge compared with top contacts whilst the hBN mode remains at $\sim$ 1365 cm^{-1} with such shifts previously attributed to both doping and strain.[17–19]
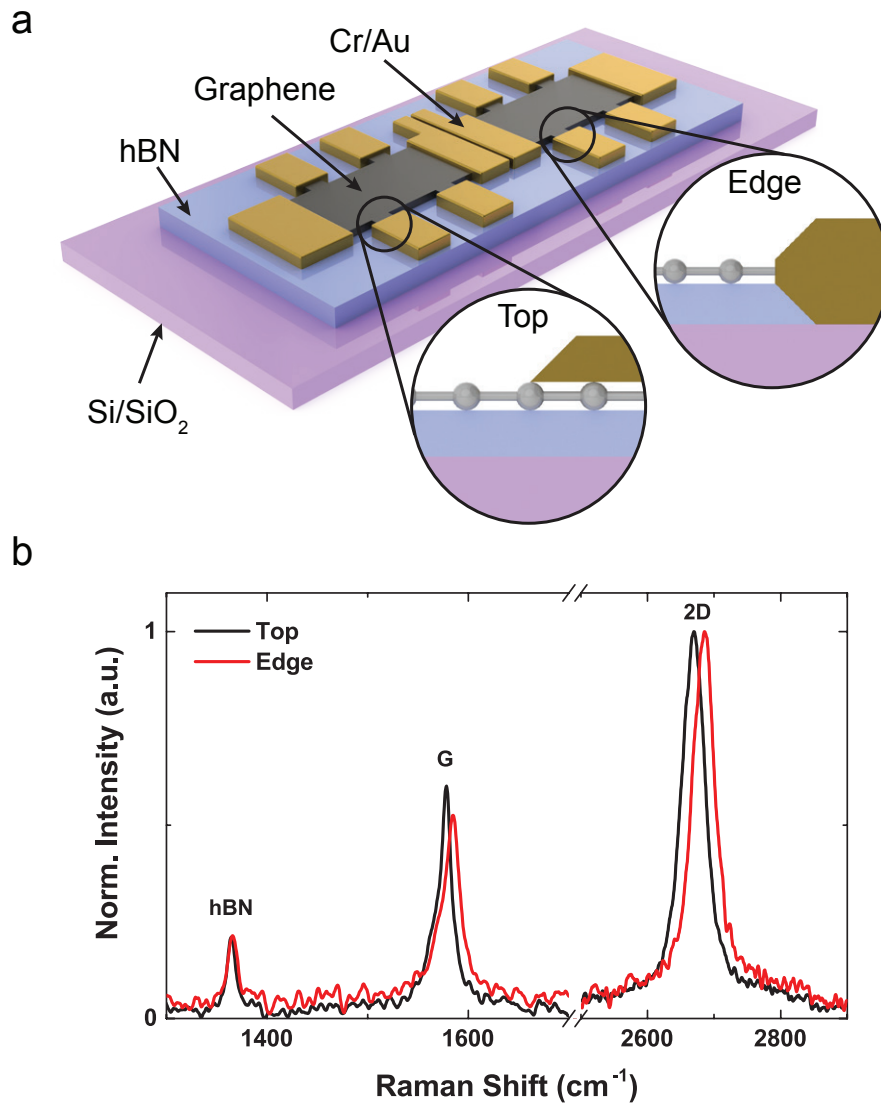
Figure 6.3: **Device schematic and Raman spectra** (a) Schematic of device. Cut-outs highlight the difference between top and edge contacts. (b) Typical Raman spectra of graphene acquired near the top (black) or edge (red) contacts.

The hBN mode and the Si peak at 520cm^{-1} are used as calibration peaks in the following analysis.

A Raman map was produced by rastering a laser beam ($\lambda = 514 \text{ nm}$) across the device and acquiring the spectra at each position. Lorentzian fits were used to identify the frequency of the G and $2D$ modes which are then plotted against each other, Figure 6.4. A clear correlation between ω_G and ω_{2D} can be seen where the data points tend to be distributed along a line. For means of comparison the expected correlation for pristine (suspended) graphene has been included,[19] which represents the ideal case with only intrinsic doping and residual strain. Previous works have verified that suspended graphene is free from strain through polarized Raman spectroscopy. Anisotropic strain leads to the splitting of the G mode with the relative intensity of each peak correlated to the angle of polarization.[20] Therefore by suspending graphene over a trench the occurrence of isotropic strain can be excluded and then the
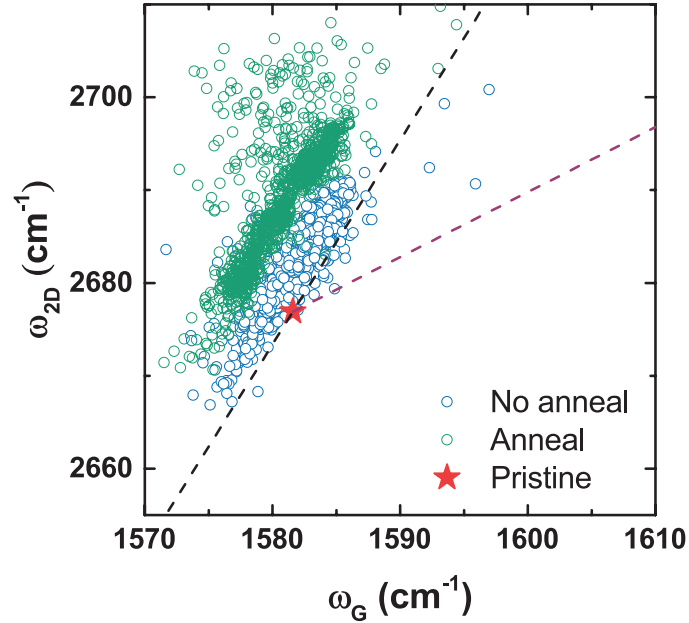
Figure 6.4: $\omega_{\mathbf{G}} - \omega_{\mathbf{2D}}$ **space** G and 2D peak frequencies from a Raman map of the device before (blue circles) and after (green circles) annealing. The red star indicates the expected values for suspended pristine graphene taken from literature.[19] Black (pink) line shows the expected dependence of ω_G/ω_{2D} on strain (hole doping).

presence of anisotropic strain can be investigated. Within the experimental error it was found that this is less than $0.1\,\%$.[20] Taking literature values for strain we plot the effect on ω_G and ω_{2D} (black dashed line) using $(\Delta\omega_{2D}/\Delta\omega_G)^{uniaxial}_{\varepsilon} = 2.2$,[19] where this represents an average value between the case with strain aligned along the zigzag and arm-chair directions. The influence of doping is more complicated as it depends on the type of charge carriers (electron or hole) and is more pronounced for ω_G than ω_{2D} because of the non-adiabatic electron-phonon coupling.[21] Hole doping results in a quasi-linear dependence of $(\Delta\omega_{2D}/\Delta\omega_G)^{hole}_n = 0.70$. For low electron doping levels ($n_e \leq 7.5 \times 10^{12}\,\mathrm{cm^{-2}}$) the dependence remains linear but for greater doping this becomes highly non-linear. However it is commonly found that both pristine and annealed graphene is hole doped. Given that the data points are distributed along the strain line one can conclude that graphene is uniformly doped with a distribution in strain. The vertical shift away from the pristine case is thought to be due to Fermi velocity reduction, previously reported for graphene on hBN and arises from van der Waals interlayer interaction.[22,23] Upon thermal annealing for 2 hours in forming gas ($\mathrm{H_2/Ar}$, $10\%/90\%$) at $200\,^{\circ}\mathrm{C}$ the data set shifts vertically upwards, suggesting a greater Fermi velocity reduction from increasing interlayer interaction.

Figure 6.5a shows a computation flow diagram for extracting the strain and doping contributions to the ω_G and ω_{2D} peak positions following the work of Ji Eun Lee and co-authors.[19] The raw data is fit with Lorenztian peaks following a
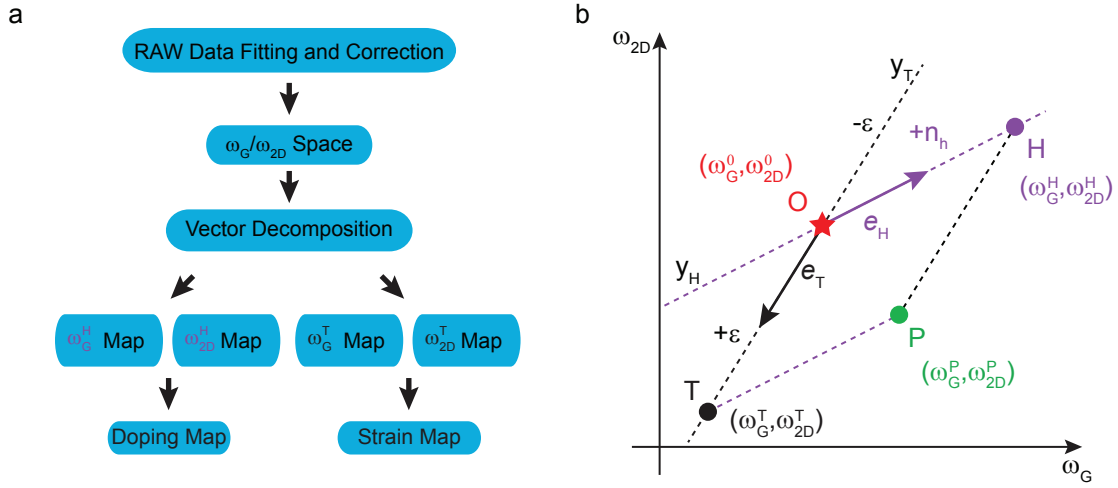
Figure 6.5: **Vector model for G and 2D mode frequencies** (a) Computational flow diagram for extracting strain and doping contributions to the ω_G and ω_{2D} peak positions. (b) Vector map of ω_G/ω_{2D}. Any vector **OP** can be decomposed into the strain-free **OH** and charge-neutral **OT** directions. Unit vectors: $\mathbf{e_H}$ hole doping, $\mathbf{e_T}$ tensile strain, and $-\mathbf{e_T}$ compressive strain.

calibration step using the hBN Raman mode. This produces the ω_G/ω_{2D} space seen in Figure 6.4. Each point represents a vector from the pristine case which can be decomposed into ω_G and ω_{2D} maps for doping and strain. Doping and strain maps can be produced by combining these contributions. Figure 6.5b shows the vector map where any vector from the origin **O** to a point **P** (**OP**) can be decomposed into the strain-free **OH** and charge neutral **OT** direction with unit vectors $\mathbf{e_H}$ for hole doping, $\mathbf{e_T}$ for tensile strain and $-\mathbf{e_T}$ for compressive strain. The dashed lines can be expressed as:

$$
\begin{aligned}
y_H &= \omega_{2D}^0 + \Delta_H \left(\omega_G^H - \omega_G^0\right) \\
y_T &= \omega_{2D}^0 + \Delta_T \left(\omega_G^T - \omega_G^0\right) \\
y_H^P &= \omega_{2D}^P + \Delta_H \left(\omega_G^T - \omega_G^P\right) \\
y_T^P &= \omega_{2D}^P + \Delta_T \left(\omega_G^H - \omega_G^P\right),
\end{aligned}
\tag{6.2}
$$

where $\Delta_H = (\Delta\omega_{2D}/\Delta\omega_G)_n^{hole}$ and $\Delta_T = (\Delta\omega_{2D}/\Delta\omega_G)_\varepsilon^{uniaxial}$. Solving these by finding their intercept yields:

$$
\begin{aligned}
w_G^H &= \frac{\omega_{2D}^P - \omega_{2D}^0 + \Delta_H\omega_G^0 - \Delta_T\omega_G^P}{\Delta_H - \Delta_T} \\
w_{2D}^H &= \omega_{2D}^P + \Delta_T(\omega_G^H - \omega_G^P) \\
w_G^T &= \frac{\omega_{2D}^P - \omega_{2D}^0 + \Delta_T\omega_G^0 - \Delta_H\omega_G^P}{\Delta_T - \Delta_H} \\
w_{2D}^T &= \omega_{2D}^P + \Delta_H(\omega_G^T - \omega_G^P).
\end{aligned}
\tag{6.3}
$$

Finally the doping and strain values can be calculated using $\Delta n = \frac{\Delta\omega_G^H}{-13.1}$ $[10^{13}\,\mathrm{cm}^{-2}]$ and $\Delta\varepsilon = \frac{\Delta\omega_G^T}{-23.5}$ $[\%]$ respectively with the values taken from literature.[17,18]
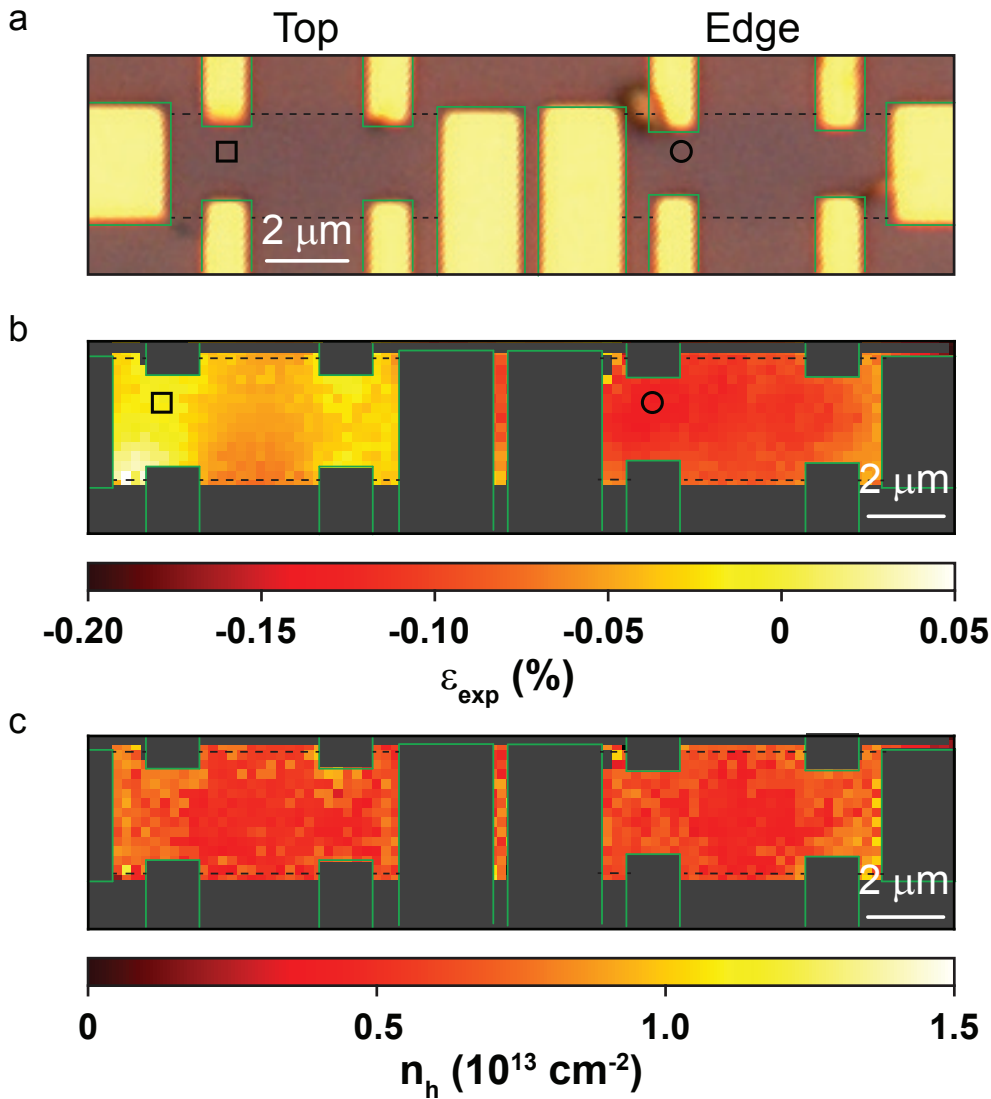
Figure 6.6: **Strain and doping maps** (a) Optical image of the device. Contacts outlined in green. Graphene channel bounded by the dashed lines. Device regions for top and edge contacts are labelled. Strain (b) and doping (c) maps extracted using the vector analysis. The symbols refer to the positions the indiviual spectra in Figure 6.3b were acquired.

6.4 Raman mapping

Figure 6.6 visualises the strain and doping distributions within the device by applying the vector decomposition analysis to the ω_G and ω_{2D} Raman maps. In the optical image the metal contacts and graphene flake have been outlined with solid green and dashed black lines respectively with the top and edge electrode regions identified, Figure 6.6a. It is known that graphene on hBN becomes compressively strained owing to the difference in lattice constants ($\delta \sim 1\%$) with $\varepsilon \sim -0.1\%$. However a clear distinction in the level of strain between the two regions is observed in Figure 6.6b. For the edge contacts strain is uniformly distributed across the graphene channel. Conversely for the top contacts regions of large strain are seen
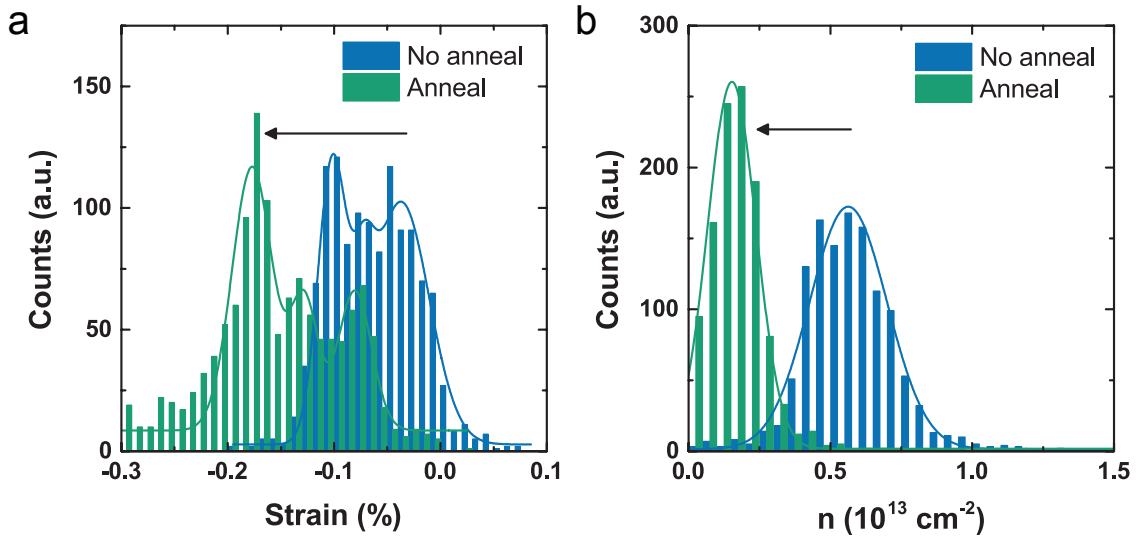
Figure 6.7: **Strain and doping statistics** (a) Histogram of strain values before (blue) and after thermal annealing (green). A multipeak Gaussian is required to fit the data corresponding to 3 distinct regions of strain. (b) Histogram of hole doping values. A single Gaussian fit suggests uniform doping across the whole device.

between opposing electrodes with lower strain levels in the central area between electrodes. Figure 6.6c shows the doping distribution of the device. In contrast to strain the doping is uniform across both top and edge contact geometries.

The visual representation of strain and doping in Figure 6.6 provides an insight into the impact of the different contacts. By examining the statistics behind these maps both parameters can be quantified. Figure 6.7a shows a histogram plot of the strain distribution in the device. The data is fit with three Gaussian peaks indicating three distinct regions of strain with two coming from the top and one from the edge contact regions. Our analysis reveals a Gaussian peak located at $\varepsilon = -0.10\%$ and confirms earlier reports that graphene on hBN is compressively strained. By comparison with the strain map this is assigned to the edge contact region, see Figure 6.6b. The other two peaks correspond to strain emerging from opposing top contacts and the channel between adjacent pairs. The non-uniformity between these two regions can be understood by considering the relaxation of compressive strain in graphene by the metal electrodes. Metal deposition elevates the device temperature which subsequently cools once evaporation is complete. Given the difference between thermal expansion coefficients (TEC) of gold (positive) and graphene (negative) upon cooling graphene expands whilst gold contracts. This contraction dominates as the TEC of gold ($\approx 14 \times 10^{-6}\,\mathrm{K}^{-1}$) is greater than that of graphene ($\approx -7 \times 10^{-6}\,\mathrm{K}^{-1}$).[24,25] Therefore the contraction of the gold contacts relaxes the strained graphene as indicated by the Gaussian located around -0.04% strain with this relaxation extending into the channel area ($\varepsilon \sim -0.07\%$). While this is the case for top contacts no strain relaxation is observed for edge contacts. This result may be related to the fact that the effective contact area is order of

Table 6.1: Comparison of strain values for different device regions before and after annealing

	Strain (%)		Doping ($10^{12}\,\mathrm{cm}^{-2}$)	
Region	No anneal	Anneal	No anneal	Anneal
Edge	-0.102 ± 0.002	-0.177 ± 0.002	5.63 ± 0.05	1.53 ± 0.01
Top (contact)	-0.037 ± 0.001	-0.090 ± 0.003	”	”
Top (channel)	-0.072 ± 0.005	-0.128 ± 0.003	”	”

magnitudes greater for the former than the latter given their respective 2D and 1D nature.

Thermal annealing is commonly used to enhance the electrical properties of graphene FETs by improving the metal-graphene interface and reducing contamination (e.g. from polymer residues). Figure 6.7b shows a histogram of the doping levels used as an indication of contamination. In contrast to the strain statistics a single Gaussian is used to fit the data indicating uniform doping across both contact regions with $n \sim 5.6 \times 10^{12}\,\mathrm{cm}^{-2}$. Following annealing this reduces to $1.5 \times 10^{12}\,\mathrm{cm}^{-2}$ somewhat validating this common processing step. However this thermal treatment has a pronounced effect on the strain distribution, Figure 6.7a. Strain increases in all areas as evidenced by an up-shift in ε of between $0.4\,\%$ and $0.7\,\%$. Previous reports have shown that graphene on hBN can undergo a rotation upon thermal annealing,[14] increasing the crystallographic alignment, which occurs as the system tries to minimise the interlayer van der Waals energy. Table 6.1 compares values for strain before and after annealing. Strain in the edge-contacted region increases from $-0.10\,\%$ to $-0.17\,\%$ indicating that graphene has become more compressed. Similar compression is observed for top-contacts where close to (away from) the electrode an increase of $\Delta\varepsilon = -0.04\,\%$ ($\Delta\varepsilon = -0.06\,\%$) is extracted. This suggests that there is a competition between flake rotation and mechanical clamping from the metal electrodes. With increased clamping from top contacts a smaller change in strain occurs in these regions. It is clear that care should be taken when annealing graphene/hBN devices as the increased strain could lead to contact failure.

6.5 Finite Element Modelling

To validate the idea that top-contacts induce strain in graphene/hBN devices the system is described as a deformable, 2D membrane with a force applied normal to each contact and use finite element modelling to calculate the resulting strain. Due to complications in imposing initial compressive strain conditions in our model, this is added later as a constant term to the trace of the strain tensor, $\Delta tr(\varepsilon) = (\varepsilon_{xx} + \varepsilon_{yy}) + \varepsilon_0$. Previous works have shown uniform compressive strain in graphene/hBN structures therefore validating this approach.[23,26] Figure 6.8a shows the
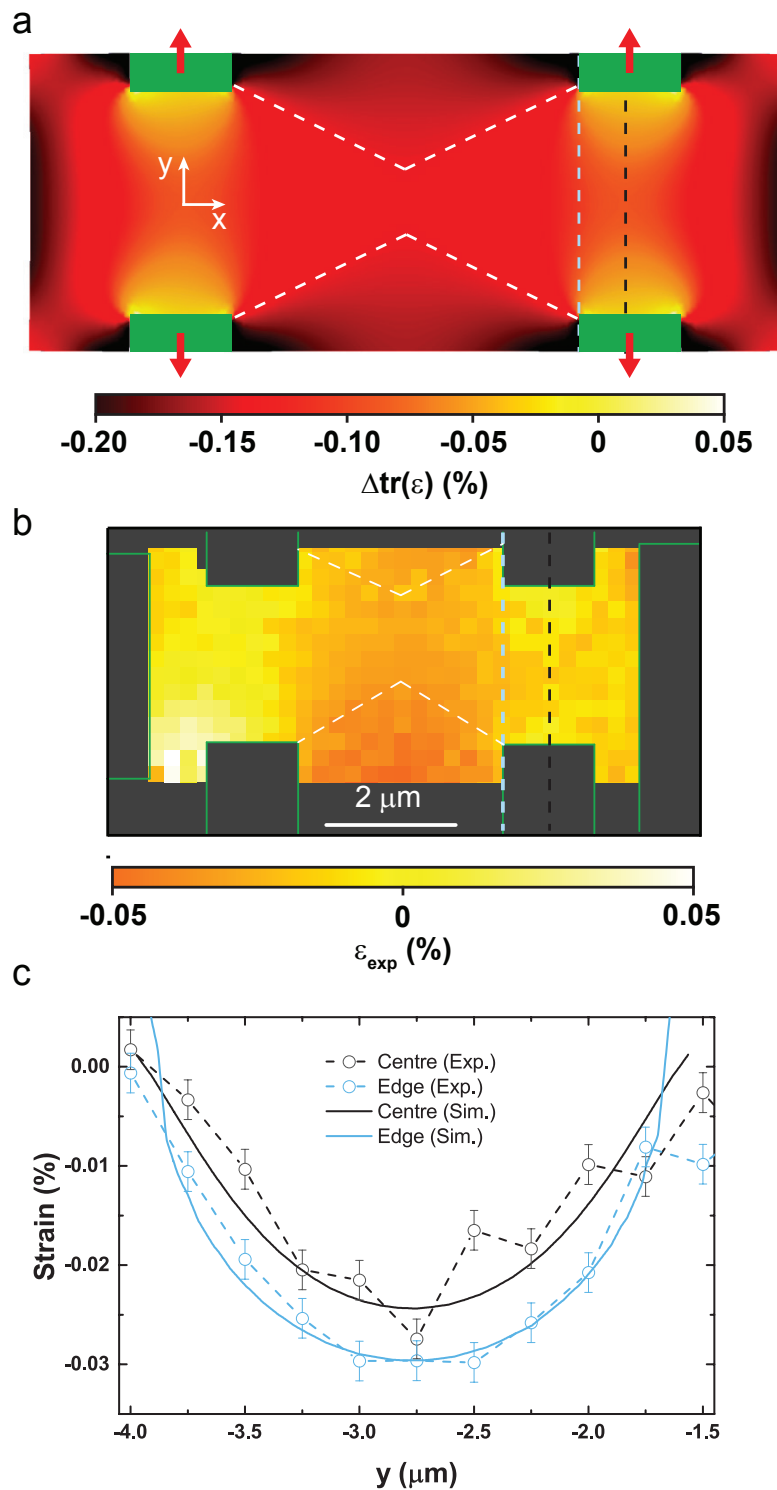
Figure 6.8: **Finite element modelling** (a) Simulated strain map of membrane in which a force equal in magnitude is applied to each voltage probe. A bow-tie strain pattern is observed in the centre (white dashed line). (b) Experimental strain map of top contact region. (c) Comparison between experimental (open circles, dashed line) and simulated (solid line) strain values extracted along the blue and black dashed lines in (a) and (b).

result of this analysis. As expected strain is observed at the contacts due to a relaxation of the initial compressive strain and more interestingly a bow-tie feature is observed between opposing contacts. Re-examination of the experimental strain map reveals the presence of both these features, Figure 6.8b. Strain induces a gauge potential in the effective Hamiltonian and the ability to engineer strain patterns could provide a system in which new physical phenomena could be investigated including the realization of a purely strain-based valley filter.[27–29] Figure 6.8c compares the experiment and simulated strain values for line-cuts in panels a and b with reasonable agreement between the two providing further justification for the validity of the model and prior explanation.

6.6   Electrical properties

Figure 6.9a shows the circuit used for characterising the electrical properties of graphene/hBN Hall bar devices. AC lock-in measurement techniques are employed to accurately probe changes in resistivity with small excitation voltages ($V_{ac} \sim 1\,\mathrm{mV}$) minimising Joule heating in the device. Two- (V_{2T}) and four-terminal (V_{4T}) voltages allow the simultaneous measurement of channel resistivity, ρ_{xx}, field-effect mobility, μ, and contact resistance, $(R_{2T} - R_{4T})/2$, Figure 6.9 b, c, and d respectively. The graphene channel is capacitively coupled to the Si^{++} backgate allowing the modulation of carrier density n by applying a DC voltage between the two V_{gs}. Figure 6.9b shows two peaks in resistivity as V_{gs} is swept between $\pm 80\,\mathrm{V}$. The first around $-20\,\mathrm{V}$ ($\rho_{xx} = 4.5\,\mathrm{k\Omega/sq}$) is identified as the charge neutrality point. However the second, a satellite peak at $V_{gs} \sim -60\,\mathrm{V}$, arises due to the emergence of additional Dirac points in the band structure of graphene on hBN, see Figure 6.1c. As the Fermi level is swept into the valence band the sign of the majority charge carrier flips at these additional Dirac points which reduces the density of states. This manifests as a peak in the resistivity of graphene. This behaviour has been previously observed in low-temperature transport experiments[8–10] and very recently at room temperature.[7] The absence of a peak on the electron-doped side ($V_{gs} > V_{CNP}$) can be explained by the asymmetry between satellite peaks in the conduction and valence bands. For the latter an energy gap emerges at the satellite peak whereas none such gap occurs in the former. This is due next-nearest-neighbour interlayer hopping which breaks electron-hole symmetry.[6]

Applying the Drude model ($\sigma = ne\mu$) allows the field-effect mobility to be extracted, Figure 6.9c, though this analysis for hole doping is complicated by the presence of the satellite peak. On the electron doping side mobilities approach $\mu = 7.4 \times 10^3\,\mathrm{cm^2\,V^{-1}\,s}$ and $\mu = 2.2 \times 10^3\,\mathrm{cm^2\,V^{-1}\,s}$ for the top and edge contacts respectively. Edge, or 1D, contacts are expected to give the highest room-temperature mobility in fully encapsulated devices.[3] However the absence of top
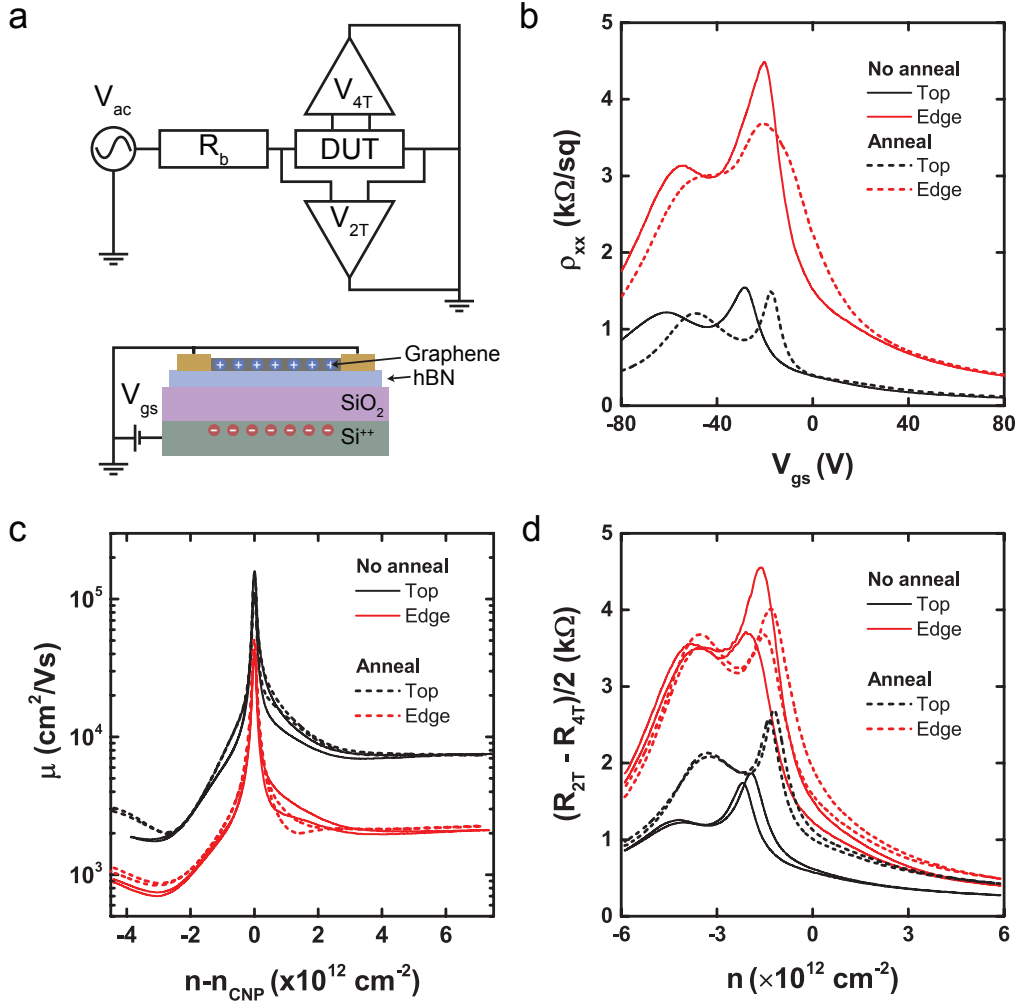
Figure 6.9: **Field effect measurements** (a) Circuit diagram (upper) and schmatic (lower) of field effect measurements. (b) Longitudinal resistivity (ρ_{xx}) as a function of gate voltage (V_{gs}). (c) Mobility (μ) versus carrier density ($n - n_{CNP}$). (d) Contact resistance ($(R_{2T} - R_{4T})/2$) versus induced carrier density (n). Electrical measurements were acquired for top (black) and edge (red) contacted regions before and after thermal annealing, solid and dashed lines respectively.

hBN means that the Cr-C bond is exposed to the environment so it is not surprising that the higher mobility is reported from the top-contacted region. Further evidence of this can be seen in Figure 6.9d where $(R_{2T} - R_{4T})/2$ for edge contacts is roughly twice as large for top contacts indicating a higher contact resistance. Interestingly thermal annealing has a more pronounced effect on the electrical performance of the latter whilst having a negligible effect on overall device mobility. For both contact types the resistivity peaks shift to smaller values of V_{gs} supporting the earlier conclusion that thermal annealing reduces doping by removing contamination. However $(R_{2T} - R_{4T})/2$ increased by a factor of two following annealing for top contacts whereas a slight reduction is observed for edge contacts.

Figure 6.10 a and b show the longitudinal resistivity (ρ_{xx}) as a function of gate voltage of the top and edge contacted regions before (a) and after (b) annealing. By taking the second derivative ($(d^2\rho_{xx}/dV_{gs}^2$) of the longitudinal resistivity (ρ_{xx})
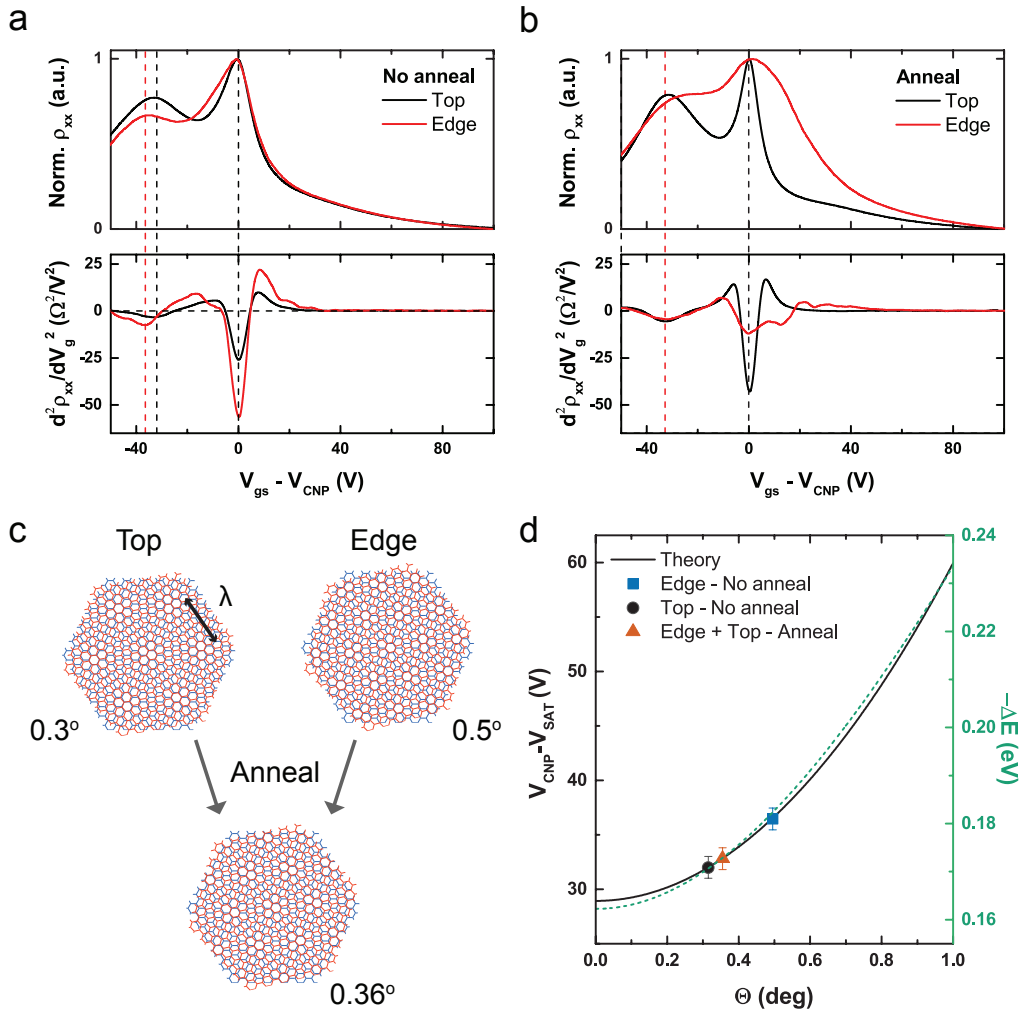
Figure 6.10: **Satellite peak analysis** Longitudinal resistivity (ρ_{xx}, upper) and second-derivative ($d^2\rho_{xx}/dV_{gs}^2$, lower) versus $V_{gs} - V_{CNP}$ before (a) and after (b) thermal annealing. (c) Schematic showing emergence of Moire pattern with different twist angles between graphene and hBN (note angles exaggerated). (d) Extracted twist angle from $V_{gs} - V_{CNP}$ data using Equation 6.1 in main text and corresponding mini-band energy level (green).

with respect to gate voltage (V_{gs}) several minima can be identified. Interestingly the separation between these minima in gate voltage, and therefore Fermi energy, is different for the top ($-32.0\,\text{V}$) and edge ($-36.5\,\text{V}$) contacted regions, Figure 6.10a.

The band structure of graphene is modified by interlayer interactions with hBN where the angle between crystallographic axes defines the interaction strength. Increasing this twist angle from $\theta = 0°$ reduces the Moiré wavelength (λ) and manifests as a shift of the satellite Dirac points away from the main Dirac point, see Equation 6.1 above. Due to the spin and valley degeneracies in graphene full filling occurs at a density of four electrons per superlattice cell ($n = 4n_0$) with the unit cell area $1/n_0 = \sqrt{3}\lambda^2/2$.[8] Carrier density and gate voltage are related though

$n = C_g(V_{gs} - V_{CNP})/e$ where C_g is the geometric capacitance. Combining these:

$$(V_{gs} - V_{CNP}) = \frac{8e}{\sqrt{3}\lambda^2 C_g}, \tag{6.4}$$

Therefore the separation between peaks in transport measurements can be correlated to the Moiré wavelength and twist angle.[7]

Rearranging Equation 6.4 allows the Moiré wavelength (λ) to be extracted from the transport data in Figure 6.10a. A value for C_g has been estimated by considering two dielectrics (SiO$_2$ and hBN) stacked in series ($C_g = 1.18 \times 10^{-4}\,\mathrm{F\,m^{-2}}$). Equation 6.1 can then be used to convert Moiré wavelength to twist angle (θ). For the top contacted regions $\lambda = 14.0\,\mathrm{nm}$ and $\theta = 0.31°$ whilst in the edge contacted regions $\lambda = 13.1\,\mathrm{nm}$ and $\theta = 0.50°$. The difference in Moiré patterns between the edge and contact regions disappears following thermal annealing, Figure 6.10b. Here the second derivative reveals that the separation between peaks is identical for the different contact regions implying that these now have the same twist angle. Indeed the analysis shows that $\lambda = 13.8\,\mathrm{nm}$ and $\theta = 0.36°$.

Figure 6.10c shows a schematic illustration of the Moiré superlattice structure formed by rotating the graphene (red) with respect to the hBN (blue). Our analysis shows that two twist angles are present before annealing with $\theta_{top} = 0.3°$ and $\theta_{edge} = 0.5°$ calculated using Equations 6.1 and 6.4. After thermal annealing one angle is now measured for both regions ($\theta = 0.36°$). The heterostructure can undergo a self-reorientation following thermal annealing due to the small twist angles present in the as-fabricated device. This movement is due to a gradient in the van der Waals forces.[14] In Table 6.1 we summarised the strain induced by the different contact regions and found that the top contacts relax the compressive strain found in graphene on hBN. On the other hand the edge contacts did not induce this relaxation and the value approaches that found in uncontacted graphene/hBN structures ($\epsilon = -0.1\,\%$).[23] Interestingly this implies that the strain induced by the top contacts has driven an initial, that is pre-thermal annealing, reorientation of twist-angle. The lower induced strain of the edge contacts does not permit such a reorientation but will allow this following thermal annealing. To summarise, Figure 6.10d plots the experimental data with the functional dependence of $V_{CNP} - V_{sat}$ versus twist angle. For reference the Moiré energy has been plotted using $\Delta E = (hv_f)/\sqrt{3}\lambda$ using a Fermi velocity of $v_f = 1 \times 10^6\,\mathrm{m\,s^{-1}}$.

The Moiré wavelength influences the phonon modes of graphene which manifests as changes in peak position and width in Raman spectroscopy. Empirically λ can be related to the full-width half-maximum of the 2D peak (Γ_{2D}) using $\Gamma_{2D} = 2.7\lambda + 0.77$, where the numerical constant (0.77) is dependent on the device structure and electrical properties (e.g. mobility).[7] Given that this constant is unknown in our devices we cannot directly compare the absolute value of λ extrapolated from Raman and trans-

port measurements. However the difference in Γ_{2D} between the top and edge contacted regions can be quantifed ($\Delta\Gamma_{2D}$). Before thermal annealing $\Delta\Gamma_{2D} = 1.0 \pm 0.5$ cm^{-1}. Afterwards this reduces to $\Delta\Gamma_{2D} \simeq 0\,$cm^{-1}, confirming the convergence of the twist-angle observed in electronic transport measurements.

6.7 Summary and outlook

In conclusion this chapter has described the influence metal contact geometry has upon strain distributions in aligned graphene/hBN heterostructures. Complementary Raman spectroscopy and electrical transport measurements allow the extraction of strain and doping across the top and edge contacted regions. In particular vector decomposition of spatial maps of the ω_G and ω_{2D} peak frequencies confirms graphene on hBN to be compressively strained. Interestingly top contacts allow a partial relaxation of this strain unlike edge contacted regions which was verified through FEM simulations. Thermal annealing was shown to be effective in reducing doping levels through the removal of contaminants. However greater strain was observed in all regions following this annealing step highlighting the risk of contact failure.

Electrical measurements reveal the emergence of satellite Dirac points by the presence of additional resistivity peaks away from the main charge neutrality point. This is to be expected for graphene aligned on hBN due to the formation of superlattice structures. Indeed analysis of the Moiré wavelengths extracted from transport measurements agree well with those from Raman spectroscopy. Interestingly distinct twist angles are observed for different contact regions which converge to a single value following annealing. These results suggest that contact design and geometry can be used to engineer the twist-angle in graphene/hBN heterostructure devices.

References

[1] A. V. Kretinin, Y. Cao, J. S. Tu, G. L. Yu, R. Jalil, K. S. Novoselov, S. J. Haigh, A. Gholinia, A. Mishchenko, M. Lozada, T. Georgiou, C. R. Woods, F. Withers, P. Blake, G. Eda, A. Wirsig, C. Hucho, K. Watanabe, T. Taniguchi, A. K. Geim, and R. V. Gorbachev. Electronic properties of graphene encapsulated with different two-dimensional atomic crystals. *Nano Letters*, 14(6):3270–3276, 2014.

[2] C R Dean, a F Young, I Meric, C Lee, L Wang, S Sorgenfrei, K Watanabe, T Taniguchi, P Kim, K L Shepard, and J Hone. Boron nitride substrates for high-quality graphene electronics. *Nature nanotechnology*, 5(10):722–726, oct 2010.

[3] L Wang, I. Meric, P. Y. Huang, Q. Gao, Y. Gao, H. Tran, T. Taniguchi, K. Watanabe, L. M. Campos, D. A. Muller, J. Guo, P. Kim, J. Hone, K. L. Shepard, and C. R. Dean. One-Dimensional Electrical Contact to a Two-Dimensional Material. *Science*, 342(6158):614–617, nov 2013.

[4] Jiamin Xue, Javier Sanchez-Yamagishi, Danny Bulmash, Philippe Jacquod, Aparna Deshpande, K. Watanabe, T. Taniguchi, Pablo Jarillo-Herrero, and Brian J. LeRoy. Scanning tunnelling microscopy and spectroscopy of ultra-flat graphene on hexagonal boron nitride. *Nature Materials*, 10(4):282–285, apr 2011.

[5] Regis Decker, Yang Wang, Victor W. Brar, William Regan, Hsin-Zon Tsai, Qiong Wu, William Gannett, Alex Zettl, and Michael F. Crommie. Local Electronic Properties of Graphene on a BN Substrate via Scanning Tunneling Microscopy. *Nano Letters*, 11(6):2291–2295, jun 2011.

[6] Matthew Yankowitz, Jiamin Xue, Daniel Cormode, Javier D. Sanchez-Yamagishi, K. Watanabe, T. Taniguchi, Pablo Jarillo-Herrero, Philippe Jacquod, and Brian J. LeRoy. Emergence of superlattice Dirac points in graphene on hexagonal boron nitride. *Nature Physics*, 8(5):382–386, may 2012.

[7] Rebeca Ribeiro-Palau, Changjian Zhang, Kenji Watanabe, Takashi Taniguchi, James Hone, and Cory R. Dean. Twistable electronics with dynamically rotatable heterostructures. *Science*, 361(6403):690–693, aug 2018.

[8] B. Hunt, J. D. Sanchez-Yamagishi, A. F. Young, M. Yankowitz, B. J. LeRoy, K. Watanabe, T. Taniguchi, P. Moon, M. Koshino, P. Jarillo-Herrero, and R. C. Ashoori. Massive Dirac Fermions and Hofstadter Butterfly in a van der Waals Heterostructure. *Science*, 340(6139):1427–1430, jun 2013.

[9] C. R. Dean, L. Wang, P. Maher, C. Forsythe, F. Ghahari, Y. Gao, J. Katoch, M. Ishigami, P. Moon, M. Koshino, T. Taniguchi, K. Watanabe, K. L. Shepard, J. Hone, and P. Kim. Hofstadter's butterfly and the fractal quantum Hall effect in moiré superlattices. *Nature*, 497(7451):598–602, may 2013.

[10] L. A. Ponomarenko, R. V. Gorbachev, G. L. Yu, D. C. Elias, R. Jalil, A. A. Patel, A. Mishchenko, A. S. Mayorov, C. R. Woods, J. R. Wallbank, M. Mucha-Kruczynski, B. A. Piot, M. Potemski, I. V. Grigorieva, K. S. Novoselov, F. Guinea, V. I. Fal'ko, and A. K. Geim. Cloning of Dirac fermions in graphene superlattices. *Nature*, 497(7451):594–597, may 2013.

[11] R. V. Gorbachev, J. C. W. Song, G. L. Yu, A. V. Kretinin, F. Withers, Y. Cao, A. Mishchenko, I. V. Grigorieva, K. S. Novoselov, L. S. Levitov, and A. K. Geim. Detecting topological currents in graphene superlattices. *Science*, 346(6208):448–451, oct 2014.

[12] Yuan Cao, Valla Fatemi, Shiang Fang, Kenji Watanabe, Takashi Taniguchi, Efthimios Kaxiras, and Pablo Jarillo-Herrero. Unconventional superconductivity in magic-angle graphene superlattices. *Nature*, 556(7699):43–50, mar 2018.

[13] C. R. Woods, L. Britnell, A. Eckmann, R. S. Ma, J. C. Lu, H. M. Guo, X. Lin, G. L. Yu, Y. Cao, R. V. Gorbachev, A. V. Kretinin, J. Park, L. A. Ponomarenko, M. I. Katsnelson, Yu. N. Gornostyrev, K. Watanabe, T. Taniguchi, C. Casiraghi, H-J. Gao, A. K. Geim, and K. S. Novoselov. Commensurate–incommensurate transition in graphene on hexagonal boron nitride. *Nature Physics*, 10(6):451–456, jun 2014.

[14] C. R. Woods, F. Withers, M. J. Zhu, Y. Cao, G. Yu, A. Kozikov, M. Ben Shalom, S. V. Morozov, M. M. van Wijk, A. Fasolino, M. I. Katsnelson, K. Watanabe, T. Taniguchi, A. K. Geim, A. Mishchenko, and K. S. Novoselov. Macroscopic self-reorientation of interacting two-dimensional crystals. *Nature Communications*, 7:10800, mar 2016.

[15] W. X. Wang, S. H. Liang, T. Yu, D. H. Li, Y. B. Li, and X. F. Han. The study of interaction between graphene and metals by Raman spectroscopy. *Journal of Applied Physics*, 109(7):07C501, apr 2011.

[16] Filippo Pizzocchero, Lene Gammelgaard, Bjarke S. Jessen, José M. Caridad, Lei Wang, James Hone, Peter Bøggild, and Timothy J. Booth. The hot pick-up technique for batch assembly of van der Waals heterostructures. *Nature Communications*, 7(May):11894, jun 2016.

[17] A Das, S Pisana, B Chakraborty, S Piscanec, S K Saha, U V Waghmare, K S Novoselov, H R Krishnamurthy, A K Geim, A C Ferrari, and A K Sood. Monitoring dopants by Raman scattering in an electrochemically top-gated graphene transistor. *Nature Nanotechnology*, 3(4):210–215, apr 2008.

[18] Duhee Yoon, Young-Woo Son, and Hyeonsik Cheong. Strain-Dependent Splitting of the Double-Resonance Raman Scattering Band in Graphene. *Physical Review Letters*, 106(15):155502, apr 2011.

[19] Ji Eun Lee, Gwanghyun Ahn, Jihye Shim, Young Sik Lee, and Sunmin Ryu. Optical separation of mechanical strain from charge doping in graphene. *Nature Communications*, 3(May):1024, 2012.

[20] Stephane Berciaud, Sunmin Ryu, Louis E. Brus, and Tony F. Heinz. Probing the Intrinsic Properties of Exfoliated Graphene: Raman Spectroscopy of Free-Standing Monolayers. *Nano Letters*, 9(1):346–352, jan 2009.

[21] Michele Lazzeri and Francesco Mauri. Nonadiabatic Kohn Anomaly in a Doped Graphene Monolayer. *Physical Review Letters*, 97(26):266407, dec 2006.

[22] Choongyu Hwang, David A. Siegel, Sung-Kwan Mo, William Regan, Ariel Ismach, Yuegang Zhang, Alex Zettl, and Alessandra Lanzara. Fermi velocity engineering in graphene by substrate modification. *Scientific Reports*, 2(1):590, dec 2012.

[23] Gwanghyun Ahn, Hye Ri Kim, Taeg Yeoung Ko, Kyoungjun Choi, Kenji Watanabe, Takashi Taniguchi, Byung Hee Hong, and Sunmin Ryu. Optical Probing of the Electronic Interaction between Graphene and Hexagonal Boron Nitride. *ACS Nano*, 7(2):1533–1541, feb 2013.

[24] Wenzhong Bao, Feng Miao, Zhen Chen, Hang Zhang, Wanyoung Jang, Chris Dames, and Chun Ning Lau. Controlled ripple texturing of suspended graphene and ultrathin graphite membranes. *Nature Nanotechnology*, 4(9):562–566, sep 2009.

[25] Duhee Yoon, Young-Woo Son, and Hyeonsik Cheong. Negative Thermal Expansion Coefficient
of Graphene Measured by Raman Spectroscopy. *Nano Letters*, 11(8):3227–3231, aug 2011.

[26] C. Neumann, S. Reichardt, P. Venezuela, M. Drögeler, L. Banszerus, M. Schmitz, K. Watanabe, T. Taniguchi, F. Mauri, B. Beschoten, S. V. Rotkin, and C. Stampfer. Raman
spectroscopy as probe of nanometre-scale strain variations in graphene. *Nature Communications*, 6(1):8429, dec 2015.

[27] A. Rycerz, J. Tworzydło, and C. W. J. Beenakker. Valley filter and valley valve in graphene.
Nature Physics, 3(3):172–175, mar 2007.

[28] T. Fujita, M. B. A. Jalil, and S. G. Tan. Valley filter in strain engineered graphene. *Applied
Physics Letters*, 97(4):043508, jul 2010.

[29] Marko M. Grujić, Milan Ž. Tadić, and François M. Peeters. Spin-Valley Filtering in Strained
Graphene Structures with Artificially Induced Carrier Mass and Spin-Orbit Coupling. *Physical
Review Letters*, 113(4):046601, jul 2014.

7

Summary

In this thesis the use of van der Waals heterostructures in novel optoelectronic devices was investigated. Each of the preceding chapters demonstrate that an improvement in the optical and electronic performance of several devices can be made by combining two or more atomically thin materials in layered structures.

The first heterostructure device we reported in Chapter 4 was a photodetector formed by combining graphene with tungsten disulphide. These photodetectors were found to be highly sensitive to light owing to a gain mechanism that produced over a million electrons per photon thanks to the excellent electrical properties of graphene. An analysis of the performance metrics show that these devices are capable of detecting light under moonlight conditions at video-frame-rate speeds with applications in night vision imaging envisaged. Future studies on the role played by charge trapping and the origin of noise are necessary to increase the performance. However our current results indicate that there is great potential for commercialisation.

Graphene was utilised again in Chapter 5 this time as a transparent electrode in a vertical tunnelling transistor. In this study we report a novel method for the direct laser writing of a high-k dielectric (HfO_x) embedded inside a van der Waals heterostructure. These dielectric layers formed tunnel barriers between the graphene electrodes and MoS_2. The confinement of injected charges in MoS_2 favours radiative recombination and subsequently leads to electroluminesence. Within the same architecture we were also able to extract photoexcited charges. The combination of a photodetector and light-emitting transistor could have applications in screens capable of simultaneously displaying and recording information. Whilst the efficiencies of these prototypes are low, improvements could be made by combining multiple cells into a single device.

In Chapter 6 we address a more fundamental problem in the properties of aligned graphene/hBN heterostructures. Strain distributions are shown to modify the electronic properties of graphene due to a change in the interlayer interaction. We were able to engineer these strain patterns by design of contact geometries and ther-

mal annealing strategies. Changes in the interlayer interaction were verified through complementary electrical transport measurements and Raman spectroscopy. This provides a valuable insight into the role played by contacts in devices governed by alignment angle. Future works should investigate the impact this has on the efficiency of light-emitting devices. In particular strain engineering could be a route to modify the band structure of atomically thin materials - providing a tunable light source.

A

Sample preparation

Device fabrication

The samples presented in this thesis have been fabricated on highly doped Silicon with a thermally grown oxide, SiO_2 (typically 290 nm) . Flakes of 2D materials were deposited via mechanical exfoliation of the bulk crystal with heterostructures formed by repeated wet or dry transfer of additional flakes, see Chapter 3 for further details of the stacking process.

After material deposition contact electrodes were defined using electron beam lithography (EBL). The positive resist PMMA (Poly(methyl methacrylate)) was spun onto the substrate (thickness ~ 300 nm), *soft-baked* at 150 °C for 1 - 2 minutes and patterned using the 80 kV electron beam of a **Nanobeam NB4** system. *Soft-baking* below the manufacturers recommended temperature assists in the formation of a clean interface between metal and flake. Low beam currents (1-5 nA) are used when directly writing on top of 2D materials. This potentially reduces the interaction of PMMA with the crystal. High beam currents (≈ 80 nA) are used for the leads and bonding pads.

Exposed PMMA was then removed through immersion in a developer solution of IPA (Isopropanol), MIBK (Methyl isobutyl ketone) and MEK (methyl ethyl ketone), at a ratio of 15:5:1 respectively typically for 30 s, then rinsed in IPA for a further 60 s and dried under a flow of N_2. Metallization was performed using a either thermal or electron beam evaporator. Generally a thin layer of Cr or Ti (5 nm) is deposited first to promote adhesion between the SiO_2 and contact metal (Au, 50 nm). The adhesion between Cr and 2D crystals, in particular hBN, appears to be stronger than that of Ti. Therefore for heterostructure devices Cr/Au is used.

To remove the PMMA mask and unwanted metal the sample is immersed in hot (70 °C) acetone for 2 hours. The final pieces of metal are gently removed with small jets of acetone from a glass pipette. If the channel has been exposed to PMMA in order to thoroughly remove PMMA residues the sample is then transferred to fresh acetone and left overnight.

If necessary device geometries were defined by EBL using PMMA *hard-baked* at 175 °C for 1 - 2 minutes as a mask. Unwanted material was then removed through reactive ion etching. For example graphene was etched in an Ar/O_2 (2:1) plasma, whilst TMDs and hBN require CHF_3 or SF_6 due to the different chemical reactions occurring at the surface of the 2D materials.

B

Summary of key photodetector performance metrics

Table B.1 shows a compilation of the data presented in Figure 2.10 of Chapter 2

Table B.1: Summary of key performance parameters for graphene, functionalised graphene and hybrid PDs. LDR and D^* values are reported only if available from the experimental data. Range of R, Δf, D^* and LDR are given corresponding to the range in $\Delta\lambda$.

Ref.	Type/Functional.	Response	R (A/W)	Δf (Hz)	$D^\star$ (Jones)	$\Delta\lambda$ (nm)[a]	LDR (dB)
			Pristine graphene				
[1]	Interdigitated	PTE	$6.1 \cdot 10^{-3}$	$1.6 \cdot 10^7$	$6 \cdot 10^{5\ b}$	1500	7.5
[2]	Suspended	PTE/PV	$6.25 \cdot 10^{-4}$	10	$1.3 \cdot 10^{4\ b}$	540	24
[3]	Dual-gated	PTE	$1.55 \cdot 10^{-3}$	—	—	532	—
[4]	Log-antenna	PTE	$5 \cdot 10^{-9}$	$7 \cdot 10^9$	—	$30\,\mu m$ to $220\,\mu m$	—
			Functionalised graphene				
[5]	FeCl$_3$	PV	$(0.015 - 0.1) \cdot 10^{-3}$	700	$10^{3\ b}$	375 to $10\,\mu m$	44
[6]	FeCl$_3$	PV	$0.1 \cdot 10^{-3}$	—	—	375	—
[7]	GO/rGO	PV	0.12	$1.6 \cdot 10^{-4}$	—	360	—
[8]	GO/rGO	PV	$4 \cdot 10^{-3}$	$3 \cdot 10^{-2}$	—	1550	—
[9]	GO/rGO	PV	$2.4 \cdot 10^{-4} - 1.4 \cdot 10^{-3}$	$2 - 2.5$	—	375 to $118.6\,\mu m$	$7 - 11$
[10]	3D np-rGO	PV	$1.33 \cdot 10^3 - 1.13 \cdot 10^4$	$6 \cdot 10^{-4}$	—	$370 - 895$	4
[11]	GO/Na$_2$So$_4$	PV	$(17.5 - 95.8) \cdot 10^{-3}$	$2 - 50 \cdot 10^{-3}$	—	$455 - 980$	—
[12]	GO	PV	$1 \cdot 10^{-3} - 1 \cdot 10^{-6}$	2.2	$3 \cdot 10^7$	$375 - 1610$	25
[13]	GO	PV	$1.6 \cdot 10^{-7} - 1.8 \cdot 10^{-6}$	$7 \cdot 10^{-3}$	—	1064	—
[14]	rGO/ZnO	PV	$1 \cdot 10^{-7} - 3 \cdot 10^{-7}$	3.3	—	$532 - 1064$	11
[15]	rGO/TiO$_2$	PV	—	0.1	—	> 400	—
[16]	FG	PG	$1000 - 10$	3	$4 \cdot 10^{11} - 1 \cdot 10^9$	$255 - 4290$	4
[17]	BTS/ATS SAMs	PTE	0.02	100	—	532	15

Hybrid and heterostructures

18	PbS QDs	PG	$5 \cdot 10^7$	10	$7 \cdot 10^{13}$	$600 - 1750$	30^c
19	PbS QDs	PG	$1 \cdot 10^6$	1.2	$-$	895	$-$
20	ZnO QDs	PG	$1 \cdot 10^4$	$-$	$-$	325	$-$
21	ZnO QDs	PG	$1 \cdot 10^4$	0.07	$5.1 \cdot 10^{13}$	335	36^c
22	ZnO QDs	PG	$2.5 \cdot 10^6$	$-$	$-$	326	$-$
23	CdS NPs	PG	$4 \cdot 10^4$	1000	$1 \cdot 10^9$	349	$-$
24	CdSe/CdS NPs	PG	10	10	10^6	$532 - 800$	$-$
25	PbS QDs/ITO	PG/PD	$2 \cdot 10^6$	$4 \cdot 10^3$	$1 \cdot 10^{13}$	$635 - 1600$	110
26	Si QDs	PG	$0.1 - 2 \cdot 10^9$	$-$	$10^3 - 10^{13}$	$375 - 3900$	$-$
27	PbS QDs/MAPbI3	PG	$2 \cdot 10^5$	100	$5 \cdot 10^{12}$	$400 - 1500$	24
28	MAPbI$_3$	PG	$18 - 180$	4	$1 \cdot 10^9$	$400 - 1000$	$-$
29	MAPbBr$_2$I	PG	$6 \cdot 10^4$	2.9	$-$	$405 - 633$	$-$
30	MAPbI$_3$ + Au NPs	PG	$2.1 \cdot 10^3$	0.2	$-$	532	
31	MAPbI$_3$	PG	$1.7 \cdot 10^7$	0.4	$2 \cdot 10^{15}$ ^{c}	$450 - 700$	$-$
32	Chlorophyll	PG	$1.1 \cdot 10^6$	0.78	$-$	$400 - 700$	$-$
33	Ruthenium	PG	$1 \cdot 10^5$	0.125	$-$	450	$-$
34	P3HT	PG	$1.7 \cdot 10^5$	5.8	$-$	500	$-$
35	C$_8$-BTBT	PG	$1.6 \cdot 10^4$	14	$-$	355	$-$
36	Rubrene	PG	$1 \cdot 10^7$	0.014	$9 \cdot 10^{11}$	$400 - 600$	$-$
37	MoS$_2$	PG	$5 \cdot 10^8$	$-$	$-$	635	$-$
38	MoS$_2$	PG	$1 \cdot 10^9$	$-$	$1 \cdot 10^{12}$	609	$-$
39	MoS$_2$	PG	$1 \cdot 10^7$	$-$	$-$	650	$-$

40	MoS$_2$	PG	46	–	–	642	–
41	GaSe	PG	$4 \cdot 10^5$	35	$1 \cdot 10^{10}$	532	–
42	MoTe$_2$	PG	970	4.5	$1.6 \cdot 10^{11}$	1064	–
43	WS$_2$	PG	$1 \cdot 10^6$	1500	$3.8 \cdot 10^{11}$	$400 - 700$	12
44	Tunnel barrier	PG	$1.1 - 10^3$	35	–	$532 - 3200$	–

^{a} Unless other units specified; ^{b} Value calculated from data provided in the reference; ^{c} Theoretical extrapolation;

References

[1] Thomas Mueller, Fengnian Xia, and Phaedon Avouris. Graphene photodetectors for high-speed optical communications. *Nature Photonics*, 4(5):297–301, mar 2010.

[2] Vikram Patil, Aaron Capone, Stefan Strauf, and Eui-Hyeok Yang. Improved photoresponse with enhanced photoelectric contribution in fully suspended graphene photodetectors. *Scientific reports*, 3:2791, 2013.

[3] Max C. Lemme, Frank H L Koppens, Abram L. Falk, Mark S. Rudner, Hongkun Park, Leonid S. Levitov, and Charles M. Marcus. Gate-activated photoresponse in a graphene p-n junction. *Nano Letters*, 11(10):4134–4137, 2011.

[4] Martin Mittendorff, Stephan Winnerl, Josef Kamann, Jonathan Eroms, Dieter Weiss, Harald Schneider, and Manfred Helm. Ultrafast graphene-based broadband THz detector. *Applied Physics Letters*, 103(2):021113, jul 2013.

[5] Adolfo De Sanctis, Gareth F Jones, Dominique J Wehenkel, Francisco Bezares, Frank H L Koppens, Monica F Craciun, and Saverio Russo. Extraordinary linear dynamic range in laser-defined functionalized graphene photodetectors. *Science Advances*, 3(5):e1602617, may 2017.

[6] Adolfo De Sanctis, Matthew D Barnes, Iddo Amit, Monica F Craciun, and Saverio Russo. Functionalised hexagonal-domain graphene for position-sensitive photodetectors. *Nanotechnology*, 28(12):124004, mar 2017.

[7] Basant Chitara, L. S. Panchakarla, S. B. Krupanidhi, and C. N. R. Rao. Infrared Photodetectors Based on Reduced Graphene Oxide and Graphene Nanoribbons. *Advanced Materials*, 23(45):5419–5424, dec 2011.

[8] Basant Chitara, S. B. Krupanidhi, and C. N. R. Rao. Solution processed reduced graphene oxide ultraviolet detector. *Applied Physics Letters*, 99(11):113114, sep 2011.

[9] Hua Yang, Yang Cao, Junhui He, Yue Zhang, Binbin Jin, Jia-Lin Sun, Yingxin Wang, and Ziran Zhao. Highly conductive free-standing reduced graphene oxide thin films for fast photoelectric devices. *Carbon*, 115:561–570, may 2017.

[10] Yoshikazu Ito, Wenfeng Zhang, Jinhua Li, Haixin Chang, Pan Liu, Takeshi Fujita, Yongwen Tan, Feng Yan, and Mingwei Chen. 3D Bicontinuous Nanoporous Reduced Graphene Oxide for Highly Sensitive Photodetectors. *Advanced Functional Materials*, 26(8):1271–1277, feb 2016.

[11] Xiang Qi, Xianghua Zou, Zongyu Huang, Long Ren, Guolin Hao, Yundan Liu, Xiaolin Wei, and Jianxin Zhong. Ultraviolet, visible, and near infrared photoresponse properties of solution processed graphene oxide. *Applied Surface Science*, 266:332–336, feb 2013.

[12] Sin Ki Lai, Libin Tang, Yeung Yu Hui, Chi Man Luk, and Shu Ping Lau. A deep ultraviolet to near-infrared photoresponse from glucose-derived graphene oxide. *J. Mater. Chem. C*, 2(34):6971–6977, aug 2014.

[13] Shiang-Kuo Chang-Jian, Jeng-Rong Ho, J.-W. John Cheng, and Ya-Ping Hsieh. Characterizations of photoconductivity of graphene oxide thin films. *AIP Advances*, 2(2):022104, jun 2012.

[14] Hao Liu, Qi Sun, Jie Xing, Zhiyuan Zheng, Zhili Zhang, Zhiqing Lü, and Kun Zhao. Fast and Enhanced Broadband Photoresponse of a ZnO Nanowire Array/Reduced Graphene Oxide Film Hybrid Photodetector from the Visible to the Near-Infrared Range. *ACS Applied Materials & Interfaces*, 7(12):6645–6651, apr 2015.

[15] Chao Chen, Weimin Cai, Mingce Long, Baoxue Zhou, Yahui Wu, Deyong Wu, and Yujie Feng. Synthesis of Visible-Light Responsive Graphene Oxide/TiO 2 Composites with p/n Heterojunction. *ACS Nano*, 4(11):6425–6432, nov 2010.

[16] Sichao Du, Wei Lu, Ayaz Ali, Pei Zhao, Khurram Shehzad, Hongwei Guo, Lingling Ma, Xuemei Liu, Xiaodong Pi, Peng Wang, Hehai Fang, Zhen Xu, Chao Gao, Yaping Dan, Pingheng Tan, Hongtao Wang, Cheng-Te Lin, Jianyi Yang, Shurong Dong, Zhiyuan Cheng, Erping Li, Wenyan Yin, Jikui Luo, Bin Yu, Tawfique Hasan, Yang Xu, Weida Hu, and Xiangfeng Duan. A Broadband Fluorographene Photodetector. *Advanced Materials*, 29(22):1700463, jun 2017.

[17] Zongguo Wang, Shaojing Qin, Chuilin Wang, and Qun Hui. Fluorine adsorption on the graphene films: From metal to insulator. *Computational Materials Science*, 97:14–19, feb 2015.

[18] Gerasimos Konstantatos, Michela Badioli, Louis Gaudreau, Johann Osmond, Maria Bernechea, F. Pelayo Garcia de Arquer, Fabio Gatti, and Frank H. L. Koppens. Hybrid graphene–quantum dot phototransistors with ultrahigh gain. *Nature Nanotechnology*, 7(6):363–368, may 2012.

[19] Zhenhua Sun, Zhike Liu, Jinhua Li, Guo-an Tai, Shu-Ping Lau, and Feng Yan. Infrared Photodetectors Based on CVD-Grown Graphene and PbS Quantum Dots with Ultrahigh Responsivity. *Advanced Materials*, 24(43):5878–5883, nov 2012.

[20] Wenhao Guo, Shuigang Xu, Zefei Wu, Ning Wang, M. M. T. Loy, and Shengwang Du. Oxygen-Assisted Charge Transfer Between ZnO Quantum Dots and Graphene. *Small*, 9(18):3031–3036, sep 2013.

[21] Dali Shao, Jian Gao, Philippe Chow, Hongtao Sun, Guoqing Xin, Prachi Sharma, Jie Lian, Nikhil A. Koratkar, and Shayla Sawyer. Organic–Inorganic Heterointerfaces for Ultrasensitive Detection of Ultraviolet Light. *Nano Letters*, 15(6):3787–3792, jun 2015.

[22] Vinh Quang Dang, Tran Quang Trung, Le Thai Duy, Bo-Yeong Kim, Saqib Siddiqui, Wonil Lee, and Nae-Eung Lee. High-Performance Flexible Ultraviolet (UV) Phototransistor Using Hybrid Channel of Vertical ZnO Nanorods and Graphene. *ACS Applied Materials & Interfaces*, 7(20):11032–11040, may 2015.

[23] Davide Spirito, Stefan Kudera, Vaidotas Miseikis, Carlo Giansante, Camilla Coletti, and Roman Krahne. UV Light Detection from CdS Nanocrystal Sensitized Graphene Photodetectors at kHz Frequencies. *Journal of Physical Chemistry C*, 119(42):23859–23864, 2015.

[24] A. Robin, E. Lhuillier, X. Z. Xu, S. Ithurria, H. Aubin, A. Ouerghi, and B. Dubertret. Engineering the Charge Transfer in all 2D Graphene-Nanoplatelets Heterostructure Photodetectors. *Scientific Reports*, 6:24909, 2016.

[25] Ivan Nikitskiy, Stijn Goossens, Dominik Kufer, Tania Lasanta, Gabriele Navickaite, Frank H. L. Koppens, and Gerasimos Konstantatos. Integrating an electrically active colloidal quantum dot photodiode with a graphene phototransistor. *Nature Communications*, 7(May):11954, 2016.

[26] Zhenyi Ni, Lingling Ma, Sichao Du, Yang Xu, Meng Yuan, Hehai Fang, Zhen Wang, Mingsheng Xu, Dongsheng Li, Jianyi Yang, Weida Hu, Xiaodong Pi, and Deren Yang. Plasmonic Silicon Quantum Dots Enabled High-Sensitivity Ultrabroadband Photodetection of Graphene-Based Hybrid Phototransistors. *ACS Nano*, 11(10):9854–9862, oct 2017.

[27] Alexander A. Bessonov, Mark Allen, Yinglin Liu, Surama Malik, Joseph Bottomley, Ashley Rushton, Ivonne Medina-Salazar, Martti Voutilainen, Sami Kallioinen, Alan Colli, Chris Bower, Piers Andrew, and Tapani Ryhänen. Compound Quantum Dot–Perovskite Optical Absorbers on Graphene Enhancing Short-Wave Infrared Photodetection. *ACS Nano*, 11(6):5547–5557, jun 2017.

[28] Youngbin Lee, Jeong Kwon, Euyheon Hwang, Chang-Ho Ra, Won Jong Yoo, Jong-Hyun Ahn, Jong Hyeok Park, and Jeong Ho Cho. High-Performance Perovskite-Graphene Hybrid Photodetector. *Advanced Materials*, 27(1):41–46, jan 2015.

[29] Yusheng Wang, Yupeng Zhang, Yao Lu, Weidong Xu, Haoran Mu, Caiyun Chen, Hong Qiao, Jingchao Song, Shaojuan Li, Baoquan Sun, Yi-Bing Cheng, and Qiaoliang Bao. Hybrid Graphene-Perovskite Phototransistors with Ultrahigh Responsivity and Gain. *Advanced Optical Materials*, 3(10):1389–1396, oct 2015.

[30] Zhenhua Sun, Lionel Aigouy, and Zhuoying Chen. Plasmonic-enhanced perovskite–graphene hybrid photodetectors. *Nanoscale*, 8(14):7377–7383, mar 2016.

[31] Po-Han Chang, Shang-Yi Liu, Yu-Bing Lan, Yi-Chen Tsai, Xue-Qian You, Chia-Shuo Li, Kuo-You Huang, Ang-Sheng Chou, Tsung-Chin Cheng, Juen-Kai Wang, and Chih-I Wu. Ultrahigh Responsivity and Detectivity Graphene–Perovskite Hybrid Phototransistors by Sequential Vapor Deposition. *Scientific Reports*, 7(1):46281, dec 2017.

[32] Shao Yu Chen, Yi Ying Lu, Fu Yu Shih, Po Hsun Ho, Yang Fang Chen, Chun Wei Chen, Yit Tsong Chen, and Wei Hua Wang. Biologically inspired graphene-chlorophyll phototransistors with high gain. *Carbon*, 63:23–29, 2013.

[33] Xien Liu, Eun Kwang Lee, and Joon Hak Oh. Graphene-ruthenium complex hybrid photodetectors with ultrahigh photoresponsivity. *Small*, 10(18):3700–3706, 2014.

[34] Everardus H. Huisman, Artem G. Shulga, Paul J. Zomer, Nikolaos Tombros, Davide Bartesaghi, Satria Zulkarnaen Bisri, Maria A. Loi, L. Jan Anton Koster, and Bart J. Van Wees. High gain hybrid graphene-organic semiconductor phototransistors. *ACS Applied Materials and Interfaces*, 7(21):11083–11088, 2015.

[35] Xiaolong Liu, Xiaoguang Luo, Haiyan Nan, Hui Guo, Peng Wang, Linglong Zhang, Minmin Zhou, Ziyi Yang, Yi Shi, Weida Hu, Zhenhua Ni, Teng Qiu, Zongfu Yu, Jian Bin Xu, and Xinran Wang. Epitaxial Ultrathin Organic Crystals on Graphene for High-Efficiency Phototransistors. *Advanced Materials*, 28(26):5200–5205, 2016.

[36] Gareth F. Jones, Rui M. Pinto, Adolfo De Sanctis, V. Karthik Nagareddy, C. David Wright, Helena Alves, Monica F. Craciun, and Saverio Russo. Highly Efficient Rubrene-Graphene Charge-Transfer Interfaces as Phototransistors in the Visible Regime. *Advanced Materials*, page 1702993, sep 2017.

[37] Kallol Roy, Medini Padmanabhan, Srijit Goswami, T Phanindra Sai, Gopalakrishnan Ramalingam, Srinivasan Raghavan, and Arindam Ghosh. Graphene–MoS2 hybrid structures for multifunctional photoresponsive memory devices. *Nature Nanotechnology*, 8(11):826–830, oct 2013.

[38] Kallol Roy, Tanweer Ahmed, Harshit Dubey, T. Phanindra Sai, Ranjit Kashid, Shruti Malia-kal, Kimberly Hsieh, Saquib Shamim, and Arindam Ghosh. Number-Resolved Single-Photon Detection with Ultralow Noise van der Waals Hybrid. *Advanced Materials*, 1704412:1704412, nov 2017.

[39] Wenjing Zhang, Chih-Piao Chuu, Jing-Kai Huang, Chang-Hsiao Chen, Meng-Lin Tsai, Yung-Huang Chang, Chi-Te Liang, Yu-Ze Chen, Yu-Lun Chueh, Jr-Hau He, Mei-Yin Chou, and Lain-Jong Li. Ultrahigh-Gain Photodetectors Based on Atomically Thin Graphene-MoS2 Heterostructures. *Scientific Reports*, 4(1):3826, may 2014.

[40] Domenico De Fazio, Ilya Goykhman, Duhee Yoon, Matteo Bruna, Anna Eiden, Silvia Milana, Ugo Sassi, Matteo Barbone, Dumitru Dumcenco, Kolyo Marinov, Andras Kis, and Andrea C. Ferrari. High Responsivity, Large-Area Graphene/MoS 2 Flexible Photodetectors. *ACS Nano*, 10(9):8252–8262, sep 2016.

[41] Rongtao Lu, Jianwei Liu, Hongfu Luo, Viktor Chikan, and Judy Z Wu. Graphene/GaSe-Nanosheet Hybrid: Towards High Gain and Fast Photoresponse. *Scientific Reports*, 6:19161, jan 2016.

[42] Wenzhi Yu, Shaojuan Li, Yupeng Zhang, Weiliang Ma, Tian Sun, Jian Yuan, Kai Fu, and Qiaoliang Bao. Near-Infrared Photodetectors Based on MoTe2/Graphene Heterostructure with High Responsivity and Flexibility. *Small*, 13(24):1–8, 2017.

[43] Jake D. Mehew, Selim Unal, Elias Torres Alonso, Gareth F. Jones, Saad Fadhil Ramadhan, Monica F. Craciun, and Saverio Russo. Fast and Highly Sensitive Ionic-Polymer-Gated WS 2 -Graphene Photodetectors. *Advanced Materials*, 29(23):1700222, jun 2017.

[44] Chang-Hua Liu, You-Chia Chang, Theodore B Norris, and Zhaohui Zhong. Graphene photodetectors with ultra-broadband and high responsivity at room temperature. *Nature nano-technology*, 9(4):273–8, mar 2014.